Dissertation

submitted to the

Combined Faculties of the Natural Sciences and Mathematics

of the Ruperto-Carola-University of Heidelberg, Germany

for the degree of

Doctor of Natural Sciences

Put forward by

M.Sc. Matthieu Kecke

born in: Magdeburg, Germany

Oral examination: 15.04.2019

Time-dependent measurement of CP violation and determination of the CKM angle γ using $B_s^0 \to D_s^{\pm} K^{\mp} \pi^+ \pi^-$ decays with the LHCb experiment

Referees:

Prof. Dr. Ulrich Uwer

Prof. Dr. Hans-Christian Schultz-Coulon

Abstract

The measurement of time-dependent CP violation in $B_s^0 \to D_s^{\pm} K^{\mp} \pi^+ \pi^-$ decays and the determination of the CKM angle γ is performed using a dataset collected by the LHCb experiment in proton-proton collisions during Run I (2011-2012) and Run II (2015-2017) of the LHC operation, corresponding to an integrated luminosity of 6.7 fb^{-1}. The results are presented in terms of the CP-violating parameters C, D_f, and S_f, which are found to be

$$\begin{aligned} C &= 0.68 \pm 0.12 \pm 0.02, \\ D_f &= 0.01 \pm 0.32 \pm 0.08, \\ D_{\bar{f}} &= 0.38 \pm 0.30 \pm 0.08, \\ S_f &= -0.14 \pm 0.17 \pm 0.04, \\ S_{\bar{f}} &= -0.54 \pm 0.17 \pm 0.04, \end{aligned}$$

where the uncertainties are statistical and systematic, respectively. The measured parameters correspond to a 3.4σ evidence of CP violation in the interference between decay and decay after mixing. These parameters are used together with the value of the B_s^0 mixing phase β_s to determine the CKM angle γ using $B_s^0 \to D_s^{\pm} K^{\mp} \pi^+ \pi^-$ decays, yielding

$$\gamma = (65^{+27}_{-20})^{\circ},$$

where statistical and systematic uncertainties are combined. The obtained value of γ agrees with the world average within its uncertainties. This analysis represents the first determination of CP violation in this decay channel and the second result on the CKM phase γ from a time-dependent measurement. In addition, an amplitude analysis of $B_s^0 \to D_s^{\pm} K^{\mp} \pi^+ \pi^-$ decays is presented and the sensitivity of a time-dependent amplitude model to γ in this decay channel is discussed.

Kurzfassung

In dieser Arbeit werden die Messung von CP Verletzung in $B_s^0 \to D_s^{\pm} K^{\mp} \pi^+ \pi^-$ Zerfällen und die Bestimmung des CKM Winkels γ vorgestellt. Hierzu werden Daten des LHCb Experiments verwendet, welche aus Proton-Proton Kollisionen während Run I (2010-2012) und Run II (2015-2017) des LHC aufgenommen wurden und einer integrierten Luminosität von 7 fb^{-1} entsprechen. Die Resultate werden bezüglich der CP-verletzenden Parameter C, D_f und S_f präsentiert:

$$\begin{aligned} C &= 0.68 \pm 0.12 \pm 0.02, \\ D_f &= 0.01 \pm 0.32 \pm 0.08, \\ D_{\bar{f}} &= 0.38 \pm 0.30 \pm 0.08, \\ S_f &= -0.14 \pm 0.17 \pm 0.04, \\ S_{\bar{f}} &= -0.54 \pm 0.17 \pm 0.04, \end{aligned}$$

wobei sich die erste Unsicherheit aus dem statistischen Fehler und die zweite Usicherheit aus dem systematischen Fehler ergibt. Die gemessenen Parameter entsprechen einem Hinweis auf CP-Verletzung mit 3.4σ Signifikanz. Diese Parameter werden, zusammen mit dem Wert der B_s^0 Mischungsphase β_s, benutzt um den CKM Winkel γ aus $B_s^0 \to D_s^{\pm} K^{\mp} \pi^+ \pi^-$ Zerfällen zu bestimmen. Die Messung ergibt

$$\gamma = (65^{+27}_{-20})^{\circ},$$

wobei die Unsicherheit sowohl statistische als auch systematische Fehler enthält. Diese Analyse repräsentiert die erste Bestimmung von CP-Verletzung in diesem Zerfallskanal und die zweite zeitabhängige Messung des CKM Winkels γ. Der gemessene Wert für γ stimmt innerhalb seiner Unsicherheit mit dem Weltdurchschnitt überein. Zusätzlich werden in dieser Arbeit eine Amplitudenanalyse des Zerfalls $B_s^0 \to D_s^{\pm} K^{\mp} \pi^+ \pi^-$ vorgestellt und die Sensitivität eines zeitabhängigen Amplituden-Modells für die Messung von γ in diesem Kanal diskutiert.

Contents

Chapter 1

Preface

The analysis presented in this thesis has been performed using data from the LHCb experiment, a collaboration of around 800 scientists and 400 technicians from 72 institutes, representing 16 countries (numbers as of June 2017 [1]). This thesis would not have been possible without numerous contributions of many current and former members of the collaboration.

The measurement of CP violation and the CKM angle γ in $B_s^0 \to D_s^\pm K^\mp \pi^- \pi^+$ decays is the work of an analysis group of which two Ph.D. students, including the author, are the main contributors. Every step of the presented analysis has been performed by the author, while his main contributions were the selection of B_s^0 signal candidates and the separation from the background, as well as the determination of the decay-time resolution, the calibration of the flavor tagging algorithms and the evaluation of the B_s^0-$\bar{B}_s^0$ production and $K^\pm$ detection asymmetry. The decay-time acceptance, the implementation of the fitting procedure for the time-dependent, phase space averaged fit, as well as the evaluation of systematic uncertainties was studied in a combined effort together with the second student. A time-dependent description of the intermediate hadronic amplitudes contributing to the $B_s^0 \to D_s^\pm K^\mp \pi^- \pi^+$ decay was mainly developed by the second Ph.D. student.

For the fit implementation, a formalism and software first developed in [2] and further improved in [3] to describe the different hadronic amplitudes is used and combined with parts of a package used to describe time-dependent decay rates of beauty meson to charm meson transitions [4]. The measurement of CP violation and the determination of the CKM angle γ using $B_s^0 \to D_s^\pm K^\mp \pi^- \pi^+$ decays is documented in detail in the internal note [5] and will be published in a dedicated paper [6] with the author as one of the two main contributors.

The presented thesis focuses on the model-independent, phase space integrated time-dependent determination of the CP parameters and γ, while a sensitivity study using

an amplitude-dependent fit is briefly summarized and estimates on the sensitivity to the CKM angle γ are quoted.

Chapter 2

Introduction

For over 40 years, the current formulation of the Standard Model of particle physics (SM) has been enormously successful in describing fundamental physics at the quantum scale and predicting particle states and properties that are observed in various experiments. However, it is evident that the Standard Model is not a complete theory that describes all phenomena observed in nature. Although successfully describing and unifying the electromagnetic and weak force, as well as the strong nuclear force, the Standard Model does not include the theory of general relativity that describes gravitational interactions. Moreover, it fails to explain the existence of dark matter and dark energy and the magnitude of the excess of matter with respect to anti-matter in our observable universe. Besides these practical shortcomings, it also exhibits theoretical issues such as extensive fine-tuning of parameters and the hierarchy problem [7].

New theories, expanding the Standard Model to accommodate the mentioned phenomena and mitigate mathematical inconsistencies can be tested with data from the Large Hadron Collider (LHC) near Geneva. It is the world's largest proton accelerator, reaching the highest energy scale to date. During the first two operation phases of the LHC, at center of mass energies of 7 and 8 TeV for Run I (2010-2012) and 13 TeV for Run II (2015-2018), various notable measurements were published. Among them the discovery of a Standard Model-like Higgs particle [8, 9] and the first observation of a matter state that consists of five quarks [10], both of which sparked especially large public interest.

One approach to explore physics at the highest energy scales at the LHC is to study amplitudes of rare decays and CP-violating observables, which are very sensitive to new heavy degrees of freedom contributing to quantum loops, making them excellent probes for new physics effects. The Large Hadron Collider beauty experiment, LHCb, one of the four experiments at the LHC, is designed to study those effects in decays of b- and c-hadrons. Due to the large amount of produced $b\bar{b}$ quark pairs, even beauty hadron decay modes that happen rarely with absolute branching fractions of less than one part

per million can be studied with high precision.
A particular interesting channel is the $B_s^0 \to D_s^\pm K^\mp \pi^- \pi^+$ decay, where CP violation occurs in the interference of the B_s^0 mixing and decay amplitudes, as well as in the decay amplitudes themselves [11, 12, 13]. A time-dependent analysis is sensitive to the magnitude of CP-violation present in this process, as well as the Cabibbo-Kobayashi-Maskawa [14, 15] (CKM) angle γ. This angle is an important input parameter to the Standard Model and a comparison between the value of γ determined in direct measurements like the presented analysis, as well as the value obtained from indirect measurements using other Standard Model observables, presents an excellent consistency check of the SM.

This thesis is structured as follows: In Chapter 3 the Standard Model of particle physics is introduced, with focus on the electroweak sector. The LHCb experiment is presented in Chapter 4. Chapter 5 discusses the strategy implemented to extract the CP violation parameter and the angle γ in the presented analysis. The selection process which isolates the $B_s^0 \to D_s^\pm K^\mp \pi^- \pi^+$ signal decays from the large LHCb data sample is discussed in Chapter 6 and 7. The relevant input for the analysis of the decay time spectrum of signal B_s^0 candidates is summarized in Chapter 8 and 9. The fits to this spectrum for $B_s^0 \to D_s^\pm \pi^\mp \pi^- \pi^+$ and $B_s^0 \to D_s^\pm K^\mp \pi^- \pi^+$ decays, as well as the estimation of possible sources of systematic uncertainty to this measurement and the determination of the CKM angle γ from the measured CP parameters is shown in Chapter 10. A time-dependent amplitude model that describes the intermediate hadronic resonances, contributing to the $B_s^0 \to D_s^\pm K^\mp \pi^- \pi^+$ decay, is developed in Chapter 11, before a summary of the analysis is given and conclusions are drawn in Chapter 12.
For the sake of convenience, natural units are used throughout this thesis where the Planck constant and the speed of light are set to unity, $\hbar = c = 1$, making the units of masses, momenta and energies equal to electron volts. In addition, for all processes which involve electric charges, e.g. the $B_s^0 \to D_s^- K^+ \pi^- \pi^+$ decay, the charge-conjugate process is implicitly included unless stated otherwise.

Chapter 3

Theoretical framework

In this chapter, an introduction to the theoretical background that is important for this analysis is given. First, an overview of the Standard Model of particle physics is presented, focusing on the CKM formalism which describes the flavor transitions between quarks. This overview is followed by a summary of the theoretical framework of CP violation in the b-meson system. After that, time-dependent CP violation in the interference between the decay and mixing of B_s^0 mesons is discussed, before the specific phenomenology of the $B_s^0 \to D_s^- K^+ \pi^- \pi^+$ decay is reviewed.

3.1. The Standard Model of Particle Physics

The Standard Model of particle physics is a relativistic, renormalizable quantum field theory that describes matter and interactions at the level of fundamental particles. It is the basis for modern particle physics, comprising all known elementary particles and three of the four fundamental interactions in between them. It combines the strong interaction, which is described by the theory of quantum chromodynamics (QCD) [16], with the weak and the electromagnetic forces that are in turn unified to the Glashow-Salam-Weinberg electroweak theory [17, 18, 19].

In the Standard Model, all known matter is built up from the twelve fundamental particles with spin $\frac{1}{2}$, called fermions. Depending on their interactions, the fermions are grouped into six quarks and six leptons, where each particles has an antiparticle with identical properties but opposite charge. The quarks and leptons are further grouped into three generations, each generation containing a charged and neutral lepton, as well as two quarks of which one is down-type and one is up-type with electric charges of $-\frac{1}{3}e$ and $\frac{2}{3}e$, respectively. Leptons interact exclusively via the electromagnetic and weak force, whereas quarks carry an additional color charge, enabling them to also participate

in the strong interaction. The three charged leptons are the electron, the muon and the tau, while the neutral leptons are the corresponding neutrinos. The three quark pairs are the up and down, charm and strange and the top and bottom quarks. An overview of the fermionic particle content of the Standard Model is shown in Table 3.1.

Table 3.1.: The fermionic content of the Standard Model, with properties taken from [20].

	Quarks			**Leptons**		
generation	type	charge	mass	type	charge	mass
I	u	$+2/3e$	$2.2^{+0.5}_{-0.4}\ MeV$	e	$-1e$	$511\ keV$
	d	$-1/3e$	$4.7^{+0.5}_{-0.3}\ MeV$	ν_e	0	$< 2\ eV$
II	c	$+2/3e$	$1.28 \pm 0.03\ GeV$	μ	$-1e$	$105.7\ MeV$
	s	$-1/3e$	$95^{+9}_{-3}\ MeV$	ν_μ	0	$< 2\ eV$
III	t	$+2/3e$	$173.0 \pm 0.4\ GeV$	τ	$-1e$	$1.77\ GeV$
	b	$-1/3e$	$4.18^{+0.04}_{-0.03}\ GeV$	ν_τ	0	$< 2\ eV$

For this Table, the quoted quark masses are taken as 'free' masses in contrast to the constituent masses of quarks in bound states and the uncertainties on the lepton masses are omitted due to their smallness. The fundamental forces between the fermions are mediated by the spin 1 gauge bosons. The massless photon γ couples to the electromagnetic charge and therefore mediates the electromagnetic interactions. Weak interactions are mediated by the massive, charged $W^\pm$ bosons, which couple to the third component I_3 of the weak isospin I and the massive neutral Z boson, which couples to a combination of I_3 and the hypercharge $Y = Q - I_3$, where Q represents the electrical charge. Gluons are the massless gauge bosons of the strong interaction, coupling to the red, green and blue color charge. All known free particles are found in a colorless state, giving rise to the gluon color-octet in which each gluon is carrying a color and an anti-color charge. The particle content of the Standard Model is completed by the scalar Higgs boson H^0, which generates particle masses through its couplings discussed in the next section. Table 3.2 summarizes the bosons of the Standard Model and their properties.

The next two sections describe the unified electroweak theory. First, the electroweak symmetry breaking (EWSB) is discussed before a general introduction to flavor physics is given.

3.1.1. Electroweak Theory

The electroweak sector of the Standard Model is described by the $SU(2)_L \otimes U(1)_Y$ local gauge symmetry group. The gauge fields of this group are the three W_i fields

Table 3.2.: The bosonic content of the Standard Model, with properties taken from [20]. The uncertainties on the $W^{\pm}$ and Z masses are omitted due to their negligibility.

boson	mass	force mediation
γ	0	electromagnetic
$W^{\pm}$	80.38 GeV	weak
Z	91.19 GeV	
g	0	strong
H^0	125.09 ± 0.24 GeV	-

and the B field. The fields couple to the weak isospin I with its third component I_3 and the hypercharge Y. All fermions take part in the electroweak interaction. They are grouped into left-handed doublets with $I_3 = \pm\frac{1}{2}$. Right-handed particles form isospin singlets with $I_3 = 0$. It should be noted that there are no right-handed neutrinos in the original formulation of the Standard Model. The W_i fields couple to I_3 and therefore only to left-handed particles or right-handed antiparticles, whereas the B field couples to a combination of I_3 and Y and therefore to left-and right-handed particles alike. The W_i and B fields are not equal to the particles observed in experiments. The observed particles are the $W^{\pm}$, the Z boson and the photon γ which are linear combinations of the W_i and the B.

Experimental evidence beyond any doubt has shown that the $W^{\pm}$ and the Z bosons are massive, although direct mass terms in the electroweak Lagrangian would violate local gauge invariance. Thus, there needs to be another mechanism that gives rise to boson masses without violating the gauge symmetry. In the Standard Model, this is the Higgs-Mechanism [21] which introduces a complex scalar doublet

$$\varphi = \frac{1}{\sqrt{2}} \begin{pmatrix} \varphi_1 + i\varphi_2 \\ \varphi_3 + i\varphi_4 \end{pmatrix}, \tag{3.1}$$

leading to a potential called the Higgs potential in the electroweak Lagrangian. This potential is of the form:

$$V(\varphi) = \lambda(\varphi^{\dagger}\varphi)^2 - \mu\varphi^{\dagger}\varphi. \tag{3.2}$$

Introducing this kind of potential to the electroweak Lagrangian leads to a non-vanishing vacuum expectation value (vev) which spontaneously breaks the $SU(2)_L \otimes U(1)_Y$ symmetry. The $U(1)_Q$ electric charge symmetry remains as residual unbroken and therefore the photon remains massless. The weak bosons however acquire mass via

the covariant derivatives in the kinetic terms of the isospin doublet φ in the Lagrangian. This terms are of the form

$$\mathcal{L}_{ew} \propto (D^{\mu}\varphi)^{\dagger} D_{\mu}\varphi \text{ , with } D_{\mu} = \partial_{\mu} + \frac{1}{2}(ig_2 W_{\mu}^{i}\vec{\tau} + ig_1 \Upsilon_{\varphi} B_{\mu}), \tag{3.3}$$

where $g_{1,2}$ are the coupling constants of the weak interaction and $\vec{\tau}$ the vector of Pauli matrices σ_i with $i = \{1, 2, 3\}$. Resolving Equation 3.3 leads to mass terms for the W and Z bosons:

$$\mathcal{L}_{ew} \propto \frac{1}{2}v^2 g_2^2 W_{\mu}^{-} W_{\mu}^{+} + \frac{1}{2}v\sqrt{g_1^2 + g_2^2}^{2} Z_{\mu} Z^{\mu}. \tag{3.4}$$

The factor v is the vev of the Higgs potential and for the W and Z masses one obtains $m_W = \frac{v^2 g_2^2}{4}$, $m_Z = \frac{v^2(g_1^2+g_2^2)}{4}$.
After EWSB, the fermions acquire mass trough Yukawa terms that couple the Higgs boson to the fermionic fields. The fermionic mass terms thus appear in the Lagrangian as [22]

$$\mathcal{L}_{fermion} = -\frac{v}{\sqrt{2}}\overline{d'}_{L,i} Y_{d,i\gamma} d'_{R,i} - \frac{v}{\sqrt{2}}\overline{u'}_{L,i} Y_{u,i\gamma} u'_{R,i}, \tag{3.5}$$

where the index L denotes a left-handed and R a right-handed fermion field in its weak eigenstate $q'_{R/L,i}$, represented as column vector. The fermion masses depend on the coupling strength given by the three-by-three, complex Yukawa matrices $Y_{u/d,i\gamma}$. After EWSB the Lagrangian also features a mass term of the form

$$\mathcal{L}_{ew} \propto -\frac{1}{2}m_H^2 H^2, \tag{3.6}$$

where H is the scalar Higgs field and m_H the corresponding Higgs mass. This means that the Higgs-Mechanism predicts a massive boson called Higgs boson, which remained the last undiscovered particle of the Standard Model until its observation by the ATLAS [8] and CMS [9] collaborations in 2012.

3.1.2. Introduction to flavor physics

As discussed in the previous section, quarks acquire mass through their interaction with the Higgs field. This is expressed by the Yukawa terms in the fermionic part of the Standard Model Lagrangian, $\mathcal{L}_{fermion}$, described in Equation 3.5. Since the Yukawa matrices in $\mathcal{L}_{fermion}$ have non-zero off-diagonal elements, the weak eigenstates of the quark fields $u'_{R/L,i}$ and $d'_{R/L,i}$, as well as the corresponding anti-quark fields $\overline{q'}_{R/L,i}$, are

not equal to the mass eigenstates $q_{L/R,i}$ ($\bar{q}_{L/R,i}$). The mass eigenstates are obtained by unitary transformations,

$$u_{L/R,j} = V_{(L/R,u),ij} u'_{L/R,i}, \tag{3.7}$$

$$d_{L/R,j} = V_{(L/R,d),ij} d'_{L/R,i}, \tag{3.8}$$

with the unitary transition matrices $V_{(L/R,u/d),ij}$. The same matrices appear in weak charge current interactions, allowing for transitions between up-type and down-type quarks:

$$\mathcal{L}_{cc} = -\frac{g}{\sqrt{2}} \left(\bar{u}_{L,i} \gamma^\mu W^+_\mu (V_{(L,u),ij} V^\dagger_{(L,d),ij}) d_{L,i} + \bar{d}_{L,i} \gamma^\mu W^-_\mu (V_{(L,u),ij} V^\dagger_{(L,d),ij})^\dagger u_{L,i} \right), \tag{3.9}$$

where γ^μ are the Dirac matrices [23]. The complex product of the unitary matrices in Equation 3.9 is defined as the Cabbibo-Kobayashi-Maskawa matrix [15],

$$V_{CKM} = V_{L,u} V^\dagger_{L,d} = \begin{pmatrix} V_{ud} & V_{us} & V_{ub} \\ V_{cd} & V_{cs} & V_{cb} \\ V_{td} & V_{ts} & V_{tb} \end{pmatrix}, \tag{3.10}$$

with non-zero off-diagonal elements that allow for transitions between quarks from different generations. The structure of V_{CKM} is hierarchical, meaning that the diagonal elements are close to unity while the off-diagonal elements are small, strongly preferring transitions within the same generation. As product of two unitary matrices, the CKM matrix is unitary itself, fulfilling $V_{CKM} \cdot V^\dagger_{CKM} = \mathbb{1}$ and reducing the number of free parameters from 18 to 9. Off those nine parameters, five can be absorbed into unobservable relative phases between the quarks. In the commonly chosen parametrization of the CKM matrix, the four remaining parameters are the three Euler angles θ_{12}, θ_{13} and θ_{23} and the complex phase δ:

$$V_{CKM} = \begin{pmatrix} c_{12}c_{13} & s_{12}c_{13} & s_{13}e^{-i\delta} \\ -s_{12}c_{23} - c_{12}s_{23}s_{13}e^{i\delta} & c_{12}c_{23} - s_{12}s_{23}s_{13}e^{i\delta} & s_{23}c_{13} \\ s_{12}c_{23} - c_{12}s_{23}s_{13}e^{i\delta} & -c_{12}s_{23} - s_{12}c_{23}s_{13}e^{i\delta} & c_{23}c_{13} \end{pmatrix}, \tag{3.11}$$

where the coefficients s_{ij} and c_{ij} are abbreviations for $s_{ij} = \sin\theta_{ij}$ and $c_{ij} = \cos\theta_{ij}$, with $i, j \in \{1, 2, 3\}$. As further discussed in the upcoming Section 3.2, CP violation

in the quark sector of the Standard Model is introduced by a non-vanishing value for the phase δ. The hierarchical structure of the CKM matrix is best represented by the Wolfenstein parametrization [24] that expresses the free parameters in terms of a small expansion parameter λ:

$$\sin\theta_{12} = \lambda, \tag{3.12}$$

$$\sin\theta_{23} = A\lambda^2, \tag{3.13}$$

$$\sin\theta_{13}e^{-i\delta} = A\lambda^3(\rho - i\eta), \tag{3.14}$$

where A, ρ, η and λ are the four free parameters of the CKM matrix in the Wolfenstein parametrization. The CKM matrix can be expressed in terms of the new parameters:

$$V_{CKM} = \begin{pmatrix} 1-\frac{\lambda^2}{2}-\frac{\lambda^4}{8} & \lambda & A\lambda^3(\rho - i\eta) \\ -\lambda & 1-\frac{\lambda^2}{2}-\frac{\lambda^4}{8}(1+4A^2) & A\lambda^2 \\ A\lambda^3(1-\rho-i\eta) & -A\lambda^2+\frac{1}{2}A\lambda^4(1-2(\rho+i\eta)) & 1-\frac{1}{2}A^4\lambda^4 \end{pmatrix} + \mathcal{O}(\lambda^5), \tag{3.15}$$

where the values for A and λ are measured to be 0.82 and 0.23 [20], respectively. It can be observed that the diagonal elements are of $\mathcal{O}(1)$, with corrections of the order λ^2 and λ^4, while the off-diagonal elements are small and scale with λ^2 and λ^3.

The unitarity condition for V_{CKM} on the diagonal terms can be written as $\Sigma_k|V_{ik}|^2 = \Sigma_i|V_{ik}|^2 = 1$, while for the off-diagonal terms the relation $\Sigma_k V_{ki}V_{kj}^* = 0$ holds. In total, six equations can be build from the second unitarity constrain, where each equation represents a triangle equation in the complex plane, e.g.

$$V_{ud}V_{ub}^* + V_{cd}V_{cb}^* + V_{td}V_{tb}^* = 0. \tag{3.16}$$

Since the elements of this triangle can generally be determined from the analysis of B_d^0 decays, it is referred to as the "B_d^0" triangle. Figure 3.1 shows this triangle, where the sides are normalized to $V_{cd}V_{cb}^*$.

The three angles of this triangle are defined by relations of the elements of V_{CKM}:

$$\alpha \equiv arg\left(\frac{V_{td}V_{tb}^*}{V_{ud}V_{ub}^*}\right),\ \beta \equiv arg\left(\frac{V_{cd}V_{cb}^*}{V_{td}V_{tb}^*}\right),\ \gamma \equiv arg\left(\frac{V_{ud}V_{ub}^*}{V_{cd}V_{cb}^*}\right). \tag{3.17}$$

Using a different, so-called "B_s^0" triangle the corresponding angle β_s is defined as

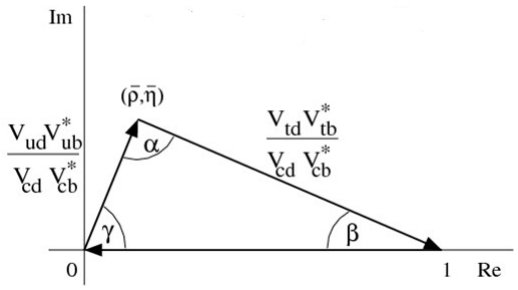

Figure 3.1.: The "B_d^0" triangle in the complex plain defined by Equation 3.16, taken from [25]. The sides are normalized to $V_{cd}V_{cb}^*$.

$$\beta_s \equiv arg\left(\frac{V_{ts}V_{tb}^*}{V_{cs}V_{cb}^*}\right). \tag{3.18}$$

With these angles, the CKM matrix can be expressed as

$$V_{CKM} = \begin{pmatrix} |V_{ud}| & |V_{us}| & |V_{ub}|e^{-i\gamma} \\ -|V_{cd}| & |V_{cs}| & |V_{cb}| \\ |V_{td}|e^{-i\beta} & -|V_{ts}|e^{i\beta_s} & |V_{tb}| \end{pmatrix} + \mathcal{O}(\lambda^5). \tag{3.19}$$

For this order, only the elements V_{ub}, V_{td} and V_{ts} have non-zero imaginary parts expressed by β, γ and β_s, respectively.
When a CP transformation, which is defined as the consecutive application of a charge (C) transformation, converting a particle into the anti-particle, and a parity (P) transformation, inverting the spatial coordinates, is performed in the charged interaction Lagrangian defined in Equation 3.9

$$CP(\mathcal{L}_{cc}) = -\frac{g}{\sqrt{2}}\left(\bar{d}_L\gamma^\mu W_\mu^- V_{CKM}^T u_L + \bar{u}_L\gamma^\mu W_\mu^+ V_{CKM}^* d_L\right), \tag{3.20}$$

it is observed that $CP(\mathcal{L}_{cc}) \neq \mathcal{L}_{cc}$ when $V_{CKM} \neq V_{CKM}^*$. Therefore, the non-vanishing complex phase of the CKM matrix introduces CP violation in the flavor sector of the Standard Model.

3.1.3. Experimental status of the CKM triangles

A multitude of measurements have been performed to determine the CKM elements and to overconstrain the CKM triangles. Figure 3.2 shows the status of the "B_d^0" triangle as of summer 2018. The elements $|V_{ub}|^2$ and $|V_{cb}|^2$, defining the length of the left side of the

triangle, are determined from measurements in semi-leptonic b-hadron decays, such as $\Lambda_b \to p\mu^-\nu$ [26], whereas the length of the right side can be constrained from measurements of the mixing frequency of the neutral B_d^0 [27] and B_s^0 [28] mesons. The angles are measured in CP-violation measurements of b-meson decays, such as the presented measurement that is sensitive to γ.

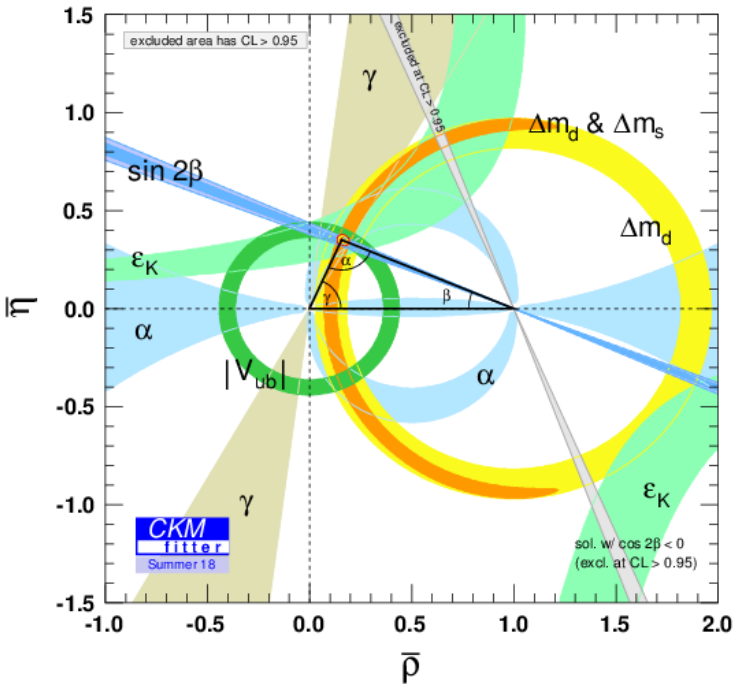

Figure 3.2.: Experimental status of the "B_d^0" triangle in the complex plain. The red hashed region corresponds to the 68 % confidence level interval. Figure taken from [29].

3.1.4. Neutral b-meson mixing

For the neutral B_s^0 meson, which is a bound flavor eigenstate consisting of a $\bar{b}s$ quark-antiquark pair, the allowed quark transitions discussed in Chapter 3.1.2 lead to the phenomena of neutral meson mixing. The appearance of mixing is equivalent to the fact that the flavor eigenstates $|B_s^0\rangle$ and $|\bar{B}_s^0\rangle$ are not equal to the mass eigenstates $|B_H\rangle$ and $|B_L\rangle$, which are eigenstates of the effective Hamiltonian $\mathcal{H}$. The behavior of the B_s^0 mesons can be expressed by an effective Schrödinger equation [30]:

$$-\frac{\partial}{\partial t}\begin{pmatrix}|B_s^0\rangle\\|\bar{B}_s^0\rangle\end{pmatrix} = (M-\frac{i}{2}\Gamma)\begin{pmatrix}|B_s^0\rangle\\|\bar{B}_s^0\rangle\end{pmatrix}, \tag{3.21}$$

where M and Γ are hermitian mass and decay matrices of $\mathcal{H}$ with off-diagonal elements that allow for transitions of the flavor eigenstates. Assuming equal masses and decay width for the B_s^0 and $\bar{B}_s^0$ mesons, as required by CPT symmetry, the matrix elements of M_{ii} and Γ_{ii} are constrained to

$$M_{11} = M_{22} = m_s, \tag{3.22}$$
$$\Gamma_{11} = \Gamma_{22} = \Gamma_s, \tag{3.23}$$

while

$$M_{21} = M_{12}^*, \tag{3.24}$$
$$\Gamma_{21} = \Gamma_{12}^*, \tag{3.25}$$

follows from the hermitian nature of the matrix. The phase of the complex element M_{12} is defined as the mixing phase and determined by the CKM elements V_{ts} and V_{tb} [31],

$$\phi_M = arg(M_{12}) \approx arg(V_{tb}V_{ts}^*). \tag{3.26}$$

Diagonalizing the matrices, one finds the eigenvalues $M_{H/L}$ and $\Gamma_{H/L}$ being the masses and decay widths of the heavy and light mass eigenstates, $|B_H\rangle$ and $|B_L\rangle$, which are connected to the flavor eigenstates B_s^0 and $\bar{B}_s^0$:

$$|B_H\rangle = p|B_s^0\rangle - q|\overline{B_s^0}\rangle, \tag{3.27}$$
$$|B_L\rangle = p|B_s^0\rangle + q|\overline{B_s^0}\rangle, \tag{3.28}$$

with p and q being complex coefficients and $|p|^2 + |q|^2 = 1$. The mass and flavor eigenbasis can be expressed through each other:

$$m_s = \frac{M_H + M_L}{2},\ \Delta m_s = M_H - M_L, \tag{3.29}$$
$$\Gamma_s = \frac{\Gamma_H + \Gamma_L}{2},\ \Delta\Gamma_s = \Gamma_H - \Gamma_L, \tag{3.30}$$

with Δm_s being the mass difference and $\Delta\Gamma_s$[1] being the decay width difference of the heavy and light mass eigenstates. The time-development of the mass eigenstates can be expressed as

$$|B_H\rangle(t) = e^{-(iM_H+\Gamma_H/2)t}|B_H\rangle, \tag{3.31}$$
$$|B_L\rangle(t) = e^{-(iM_L+\Gamma_L/2)t}|B_L\rangle. \tag{3.32}$$

Inserting the expressions into the flavor states introduced in Equations 3.27 and 3.28, their time evolution can be written as

$$|B_s^0\rangle(t) = \frac{1}{2p}\left(e^{-(iM_L+\Gamma_L/2)t}|B_L\rangle + e^{-(iM_H+\Gamma_H/2)t}|B_H\rangle\right), \tag{3.33}$$
$$|\bar{B_s^0}\rangle(t) = \frac{1}{2q}\left(e^{-(iM_L+\Gamma_L/2)t}|B_L\rangle - e^{-(iM_H+\Gamma_H/2)t}|B_H\rangle\right). \tag{3.34}$$

The amplitude to observe an initially-produced B_s^0 in the same flavor or in the opposite flavor after the time t is derived by projecting the time-dependent flavor states on the pure flavor states:

$$\begin{aligned}\langle B_s^0|B_s^0(t)\rangle &= e^{(m_s-i\Gamma_s)/2)t}\left(\cosh(\frac{\Delta\Gamma_s t}{4})\cos(\frac{\Delta m_s t}{2}) - i\sinh(\frac{\Delta\Gamma_s t}{4})\sin(\frac{\Delta m_s t}{2})\right)\\ &\approx e^{-i(m_s-i\Gamma_s/2)t}\cos(\frac{\Delta m_s t}{2}),\end{aligned} \tag{3.35}$$

$$\begin{aligned}\langle \bar{B_s^0}|B_s^0(t)\rangle &= e^{(m_s-i\Gamma_s)/2)t}\frac{q}{p}\left(-\sinh(\frac{\Delta\Gamma_s t}{4})\cos(\frac{\Delta m_s t}{2}) - i\cosh(\frac{\Delta\Gamma_s t}{4})\sin(\frac{\Delta m_s t}{2})\right)\\ &\approx e^{-i(m_s-i\Gamma_s/2)t}\frac{q}{p}i\sin(\frac{\Delta m_s t}{2}),\end{aligned} \tag{3.36}$$

where $|\Delta\Gamma_s| << |\Gamma|$ is used and the probability to find an initial B_s^0 in the respective state is given by the square of the amplitude. For the $\bar{B_s^0}$ amplitude fraction of the time-dependent state $B_s^0(t)$ (mixed fraction) $\langle\bar{B_s^0}|B_s^0(t)\rangle$, a complex phase is introduced through the ratio of the complex coefficients $\frac{q}{p}$ and $i = e^{i\pi/2}$. Computing the CP-conjugated mixed amplitude, it is observed that the ratio of the complex coefficients flips

[1] In this convention, the decay width difference is negative, $\Delta\Gamma_s < 0$

$$\langle B_s^0 | \bar{B}_s^0(t) \rangle \propto \frac{p}{q}. \tag{3.37}$$

Therefore, the phase of the ratio of p and q is related to the weak phase introduced in Equation 3.26.
The oscillations of $B_s^0 - \bar{B}_s^0$ mesons proceed via the exchange of two virtual W bosons, together with an up, charm or top quark which build a so-called loop process. The corresponding Feynman diagrams, also called box-diagrams, are shown in Figure 3.3.

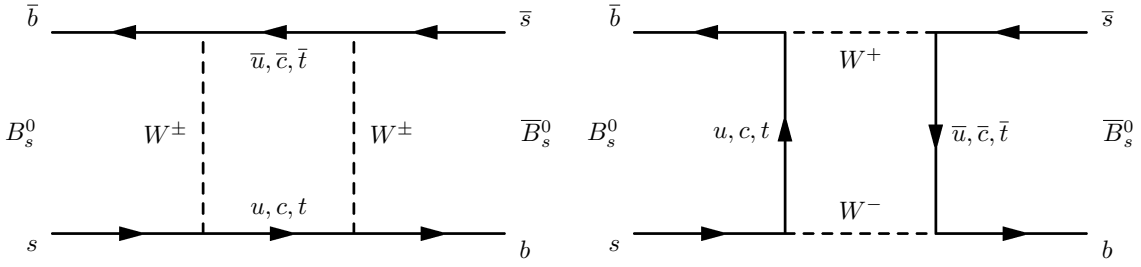

Figure 3.3.: Feynman diagrams contributing to $B_s^0 - \bar{B}_s^0$ mixing, taken from [32].

In case of equal quark masses, the GIM mechanism [33] predicts a full cancellation of the different quark contributions. Since the top quark is much heavier than the charm- and up-quark, the corresponding dominant CKM matrix elements for the processes shown in Figure 3.3 are $|V_{tb}|$ and $|V_{ts}|$, as expressed in Equation 3.26. Because $|V_{ts}|$ is an order of magnitude larger than $|V_{td}|$, which would be the corresponding element for the $B^0 - \bar{B}^0$ oscillation diagram, the mixing in the B_s^0 sector is significantly larger than in the B^0 system. This is expressed by the larger mixing frequency $\Delta m_s > \Delta m_d$.

3.2. Introduction to CP violation

The CP transformation is defined as a parity (P) and a charge (C) transformation carried out successively, which is equivalent to replacing a particle by its charge-conjugate, the antiparticle, and mirroring the coordinate system. Considering a state $|\psi\rangle$ of an arbitrary particle being the eigenstate of C and P, the transformations can be expressed as

$$P|\psi\rangle = \eta_P|\psi\rangle, \tag{3.38}$$

$$C|\psi\rangle = \eta_C|\psi\rangle, \tag{3.39}$$

$$CP|\psi\rangle = \eta_C\eta_P|\psi\rangle = \eta_{CP}|\psi\rangle, \tag{3.40}$$

where η_p, η_C and η_{CP} are the eigenvalues of the P, C and CP operators. Those eigenvalues can take ± 1, where the positive sign is referred to as a *CP even* and the negative sign is referred to as a *CP odd* behavior. In this context, CP symmetry corresponds to particle-antiparticle symmetry, while CP violation causes the particle-antiparticle symmetry to be violated in a physical processes.
CP violation is one of the necessary conditions for the observed matter excess over anti-matter present in our universe, also called baryon asymmetry [34]. The CKM mechanism described in Chapter 3.1.2 is the only source of CP violation in the Standard Model, with the predicted CP violation being several orders of magnitude too small to explain the observed asymmetry between baryonic matter and anti-matter and the resulting baryogenesis in the early universe. Several models extend the Standard Model of particle physics, where additional sources of CP violation are introduced and described by contributions that are not included in the Standard Model. Thus, precise measurements of CP violation in different physical systems, e.g. in the mixing and decay of B mesons, are crucial. There are three different types of CP violation:

- CP violation in decay
- CP violation in neutral meson mixing
- CP violation in the interference between decay and mixing

The first case is referred to as direct CP violation, whereas the other two cases are called indirect CP violation and are a consequence of the mixing of neutral mesons. Several forms of CP violation can occur at the same time. The following sections will give a brief overview of each of the three cases.

3.2.1. Direct CP violation

For direct CP violation, the decay amplitude for a particle X into a final state f, $\mathcal{A}_{X\to f}$, is not equal to the amplitude of the CP-conjugated process,

$$\left|\frac{\mathcal{A}_{X\to f}}{\mathcal{A}_{\overline{X}\to\overline{f}}}\right| \neq 1. \tag{3.41}$$

Experimentally, this observable is accessed by measuring the decay rate of both processes and determining the asymmetry

$$A_f = \frac{\Gamma(\overline{X} \to \overline{f}) - \Gamma(X \to f)}{\Gamma(X \to f) + \Gamma(\overline{X} \to \overline{f})} = \frac{1 - \left|\frac{\mathcal{A}_{X\to f}}{\mathcal{A}_{\overline{X}\to\overline{f}}}\right|^2}{1 + \left|\frac{\mathcal{A}_{X\to f}}{\mathcal{A}_{\overline{X}\to\overline{f}}}\right|^2}, \tag{3.42}$$

between the yields of the decays $X \to f$ and $\overline{X} \to \overline{f}$, where $A_f \neq 0$ indicates direct CP violation.

3.2.2. CP violation in mixing

CP violation in mixing can be expressed in terms of the previously introduced coefficients p and q, defined in Equations 3.27 and 3.28, which connect the mass and flavor eigenstates of the neutral B meson. CP violation occurs if

$$\left|\frac{q}{p}\right|^2 \neq 1, \tag{3.43}$$

which corresponds to different transition probabilities $P(B^0 \to \overline{B}^0) \neq P(\overline{B}^0 \to B^0)$. The suitable CP observable in this case is the mixing asymmetry defined as:

$$A_{\text{mixing}} = \frac{\Gamma(\overline{B}^0 \to B^0 \to f) - \Gamma(B^0 \to \overline{B}^0 \to \overline{f})}{\Gamma(\overline{B}^0 \to B^0 \to f) + \Gamma(B^0 \to \overline{B}^0 \to \overline{f})}, \tag{3.44}$$

assuming the absence of direct CP violation in the decay $B^0(\bar{B}^0) \to f(\bar{f})$. In this definition, $A_{\text{mixing}} = 0$ indicates CP conservation while a non-vanishing asymmetry indicates CP violation. Equation 3.44 can also be expressed in terms of the coefficients q and p:

$$A_{\text{mixing}} = \frac{1 - \left|\frac{q}{p}\right|^4}{1 + \left|\frac{q}{p}\right|^4}. \tag{3.45}$$

3.2.3. CP violation in the interference of mixing and decay

CP violation in the interference between mixing and decay occurs in neutral meson decays, where the meson can either directly decay into a final CP-eigenstate f_{CP} or can oscillate first and then decay to the same final state. For this process, both flavor eigenstates, e.g. B_s^0 and $\bar{B}_s^0$, have to be able to decay into the same CP eigenstate with $\eta_{CP} = \pm 1$. Figure 3.4 visualizes the process, introducing the amplitudes for the decay

of a B_s^0 ($\bar{B}_s^0$) into a CP eigenstate f_{CP},

$$A_{f_{CP}} = \langle f_{CP}|B_s^0\rangle,\ \bar{A}_{f_{CP}} = \langle f_{CP}|\bar{B}_s^0\rangle. \tag{3.46}$$

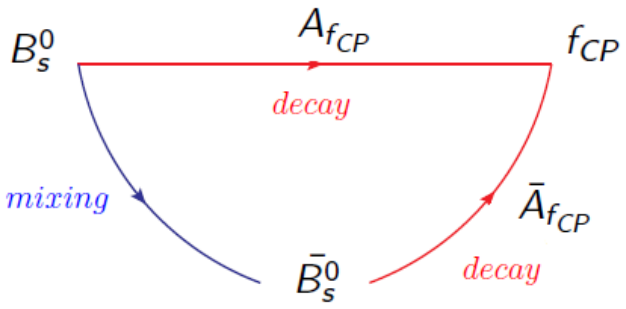

Figure 3.4.: Illustration of the interference between direct decays of B mesons to f_{CP} and decays of mixed B mesons.

The CP violation for this case can be investigated by comparing the time-dependent decay rates of, in this case B_s^0 and $\bar{B}_s^0$, mesons into the same CP final state and calculating the asymmetry:

$$A(t)_{\text{mix\&decay}} = \frac{\Gamma(\overline{B_s^0} \to f_{CP})(t) - \Gamma(B_s^0 \to f_{CP})(t)}{\Gamma(\overline{B_s^0} \to f_{CP})(t) + \Gamma(B_s^0 \to f_{CP})(t)}. \tag{3.47}$$

To obtain analytical expressions for the decay rates $\Gamma(B_s^0 \to f_{CP})(t)$ and $\Gamma(\overline{B_s^0} \to f_{CP})(t)$, the time-dependent Schrödinger Equation 3.21 needs to be solved. For this, the key quantity for CP violation [31]

$$\lambda_{f_{CP}} \equiv \frac{q}{p}\frac{\bar{A}_{f_{CP}}}{A_{f_{CP}}}, \tag{3.48}$$

where q and p are the complex mixing coefficients introduced in Chapter 3.1.4, is used. Furthermore, the eigenvalues of $(M - \frac{i}{2}\Gamma)$ from Equation 3.21 can be expanded in terms of $\frac{q}{p}$ and $\frac{\Gamma_{12}}{M_{12}}$, using the experimental fact that $\Delta m_s >> \Gamma_s$ [31]. It is found that

$$\begin{aligned} \Delta m_s &\approx 2|M_{12},| \\ \Delta\Gamma_s &\approx 2|\Gamma_{12}|, \\ \frac{q}{p} &\approx e^{-i\phi_M}, \end{aligned} \tag{3.49}$$

with the weak mixing phase ϕ_M, introduced in Equation 3.26. Solving the Schrödinger

equation using the established relations 3.49, the decay rates for a B_s^0 ($\bar{B}_s^0$) going into a CP eigenstate f_{CP} can be written as [35]:

$$\Gamma(B_s^0 \to f_{CP})(t) \propto e^{-\Gamma_s} \cdot [\cosh\left(\frac{\Delta\Gamma_s\, t}{2}\right) + A_{CP}^{dir} \cos\left(\Delta m_s\, t\right) + A_\Delta \sinh\left(\frac{\Delta\Gamma_s\, t}{2}\right) + A_{CP}^{mix} \sin\left(\Delta m_s\, t\right)], \tag{3.50}$$

$$\Gamma(\overline{B_s^0} \to f_{CP})(t) \propto e^{-\Gamma_s} \cdot [\cosh\left(\frac{\Delta\Gamma_s\, t}{2}\right) - A_{CP}^{dir} \cos\left(\Delta m_s\, t\right) + A_\Delta \sinh\left(\frac{\Delta\Gamma_s\, t}{2}\right) - A_{CP}^{mix} \sin\left(\Delta m_s\, t\right)]. \tag{3.51}$$

In Equations 3.50 and 3.51, the CP asymmetries

$$A_{CP}^{dir} = \frac{1-|\lambda_f|^2}{1+|\lambda_f|^2},\ A_{CP}^{mix} = -\frac{2Im(\lambda_f)}{1+|\lambda_f|^2},\ A_\Delta = -\frac{2Re(\lambda_f)}{1+|\lambda_f|^2}, \tag{3.52}$$

where a non-vanishing A_{CP}^{dir} signals direct CP violation, a non-vanishing A_{CP}^{mix} signals CP violation in the interference of $B_s^0 \to f_{CP}$ and $\bar{B}_s^0 \to f_{CP}$, and a non-vanishing A_Δ originates from a non-zero value of $\Delta\Gamma_s$, are introduced.
The following section will focus on the description of the decay rates for the $B_s^0 \to D_s^- K^+\pi^-\pi^+$ decay, where two complications to the formalism above are encountered: On the one hand, the ($D_s^- K^+\pi^-\pi^+$) final state is not a CP eigenstate of the B_s^0. On the other hand, different sets of decay amplitudes are needed to describe the $B_s^0 \to f$ and $\bar{B}_s^0 \to f$ decays, since one is mediated by a $b \to c$ transition at quark level, while the other is mediated by a $b \to u$ transition.

3.3. Phenomenology of the $B_s^0 \to D_s^- K^+\pi^-\pi^+$ decay

This section covers the theoretical description of the decay of B_s^0 mesons into the Cabbibo suppressed $D_s^+ K^-\pi^+\pi^-$ and Cabbibo favored $D_s^- K^+\pi^+\pi^-$ final states. The D_s^- decays further and is reconstructed in the three-body final states $K^-K^+\pi^-$, $K^-\pi^+\pi^-$ or $\pi^-\pi^+\pi^-$. While the different D_s^- final states pose an experimental challenge that is discussed in detail in Chapter 6, the respective final state in which the D_s^- is reconstructed does not influence the theoretical description of the $B_s^0 \to D_s^- K^+\pi^-\pi^+$ decay rate.

First, the decay channel is introduced and the different hadronic contributions are discussed. Then, the differential decay rate for $B_s^0/\bar{B}_s^0$ mesons decaying into the specific final state is formulated, together with the definition of the CP observables that are measured in this analysis. After that, two approaches to measure CP violation in this decay are discussed, where one model-independent approach is to purely describe the decay-time distribution of B_s^0 candidates, integrating over all possible contributing hadronic decay amplitudes, and the second approach is to explicitly account for these amplitudes using a six-dimensional (five invariant masses + B_s^0 decay time) fit model.
The decay $B_s^0 \to D_s^- K^+\pi^-\pi^+$ is mediated by a charge current $b \to c$ or $b \to u$ transition, accompanied by a W-boson. Figure 3.5 shows the Feynman diagrams of this process at quark level, highlighting the contributing CKM matrix elements $|V_{cb}|$ and $|V_{ub}|e^{-i\gamma}$, as defined in Equation 3.19.

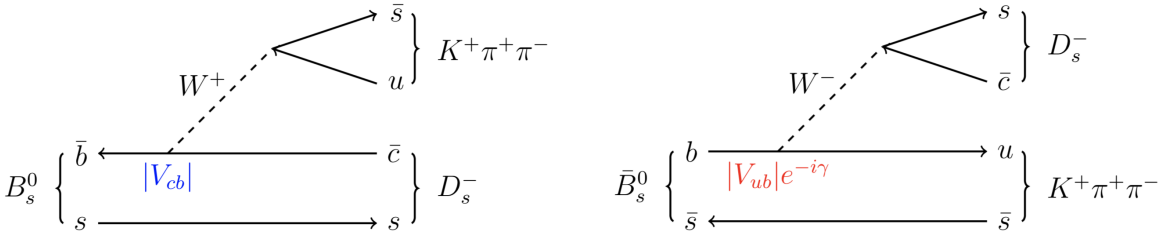

Figure 3.5.: The Feynman diagrams for (left) $B_s^0 \to D_s^- K^+\pi^-\pi^+$ and (right) $\bar{B}_s^0 \to D_s^- K^+\pi^-\pi^+$ decays, with the contributing CKM matrix element shown in blue and red, respectively.

In this decay, the $(u\bar{s})$ subsystem is dominated by the excited kaon resonances $K_1^*(1270)$ and $K_1^*(1400)$ [36], which further decay to the $K^+\pi^-\pi^+$ final state, e.g. $B_s^0 \to D_s^- K_1^+(1270) \to D_s^- K^+\pi^-\pi^+$. The fact that several resonances contribute to this decay results in a non-constant hadronic phase, which varies across the phase space available for this process. Depending on the theoretical model, this adds at least one additional hadronic parameter to the description of $B_s^0 \to D_s^- K^+\pi^-\pi^+$ decays. Figure 3.6 visualizes the $B_s^0 \to D_s^- K^+\pi^-\pi^+$ decay schematically, introducing the different decay amplitudes $\mathcal{A}_f^{b\to c}$ and $\mathcal{A}_f^{b\to u}$ for the decay of a B_s^0 ($\bar{B}_s^0$) meson to the final state $f = (D_s^- K^+\pi^-\pi^+)$ via a $b \to c$ ($b \to u$) transition at quark level.

The amplitudes used in Figure 3.6 are defined as:

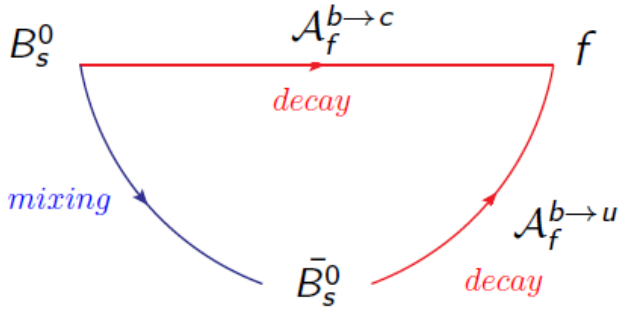

Figure 3.6.: Illustration of the interference between direct decays of B_s^0 mesons to f and decays of mixed $\bar{B}_s^0$ mesons, where different amplitudes for the $b \to c$ and $b \to u$ transitions occur.

$$\mathcal{A}(B_s^0 \to D_s^- K^+ \pi^- \pi^+) \equiv \mathcal{A}_f^{b\to c}(\vec{x}) = \sum_i a_i^{b\to c}\, \mathcal{A}_i(\vec{x}), \tag{3.53}$$

$$\mathcal{A}(\bar{B}_s^0 \to D_s^- K^+ \pi^- \pi^+) \equiv \mathcal{A}_f^{b\to u}(\vec{x}) = \sum_i a_i^{b\to u}\, \mathcal{A}_i(\vec{x}), \tag{3.54}$$

where each amplitude is defined by a coherent sum over all contributing intermediate state amplitudes $\mathcal{A}_i(\vec{x})$, each weighted by a complex coefficient $a_i^{b\to c(u)}$. Here, the phase space point $\vec{x}$ is introduced, which labels the available phase space for the $B_s^0 \to D_s^- K^+ \pi^- \pi^+$ decay. Since this decay has a six-body final state, $\vec{x}$ can be parametrized using five invariant mass combinations of the B_s^0 decay products [5]:

$$\vec{x} = \left(m(K^+\pi^-\pi^+), m(D_s^-\pi^-\pi^+), m(K^+\pi^-), m(\pi^+\pi^-), m(D_s^-\pi^+)\right). \tag{3.55}$$

Both amplitudes, $\mathcal{A}_f^{b\to c}(\vec{x})$ and $\mathcal{A}_f^{b\to u}(\vec{x})$, are explicitly dependent on $\vec{x}$ due to the fact that different hadronic resonances with different amplitudes $\mathcal{A}_i(\vec{x})$ are dominating particular regions of the available $(D_s^- K^+ \pi^- \pi^+)$ phase space.
The sensitivity of the $B_s^0 \to D_s^- K^+ \pi^- \pi^+$ decay to the weak phase $\gamma \approx \arg(V_{ub})$ originates from the interference between $b \to c$ and $b \to u$ quark transitions, achieved through mixing of the neutral B_s^0 meson [13, 37]. Since in the amplitudes of both processes, the Wolfenstein parameter enters in equal order, $\mathcal{O}(\lambda^3)$, the interference effects are expected to be sizable. As a result of the interference between mixing and decay amplitudes, the CP-violating observables that are extracted in this analysis are a function of the CKM angle γ and the B_s^0 mixing phase β_s.

3.3.1. Definition of the decay rates and the CP observables

The differential decay rate of B_s^0 or $\bar{B}_s^0$ decays to the final state $D_s^- K^+\pi^+\pi^-$ or $D_s^+ K^-\pi^+\pi^-$ depends on the decay time t, as well as the 5-dimensional point in phase space $\vec{x}$ [5]. Using the abbreviation $\mathcal{A}_f^{b\to c}(\vec{x}) \equiv \mathcal{A}_f^c(\vec{x})$ and $\mathcal{A}_f^{b\to u}(\vec{x}) \equiv \mathcal{A}_f^u(\vec{x})$ for convenience, the decay rate in its most general form can be written as:

$$\begin{aligned}\frac{\mathrm{d}\Gamma(\vec{x},t,q,f)}{\mathrm{d}t\,\mathrm{d}\Phi_4} \propto e^{-\Gamma_s t}[&\left(|\mathcal{A}_f^c(\vec{x})|^2 + |\mathcal{A}_f^u(\vec{x})|^2\right)\cosh\left(\frac{\Delta\Gamma_s\, t}{2}\right)\\ &+ q\,f\,\left(|\mathcal{A}_f^c(\vec{x})|^2 - |\mathcal{A}_f^u(\vec{x})|^2\right)\cos\left(\Delta m_s\, t\right)\\ &- 2\mathrm{Re}\left(\mathcal{A}_f^c(\vec{x})^*\,\mathcal{A}_f^u(\vec{x})\,e^{-if(\gamma-2\beta_s)}\right)\sinh\left(\frac{\Delta\Gamma_s\, t}{2}\right)\\ &- 2\,q\,f\,\mathrm{Im}\left(\mathcal{A}_f^c(\vec{x})^*\,\mathcal{A}_f^u(\vec{x})\,e^{-if(\gamma-2\beta_s)}\right)\sin\left(\Delta m_s\, t\right)],\end{aligned} \tag{3.56}$$

where $q = +1$ (-1) refers to an initially produced B_s^0 ($\bar{B}_s^0$) flavor eigenstate (with $q = 0$ refering to an undetermined initial flavor), $f = +1$ or -1 denotes $D_s^- K^+\pi^+\pi^-$ or $D_s^+ K^-\pi^+\pi^-$ final states, $\mathcal{A}_f^c(\vec{x})$ and $\mathcal{A}_f^u(\vec{x})$ are the decay amplitudes for $b \to c$ and $b \to u$ transitions and Γ_s is the decay width of the $B_s^0/\bar{B}_s^0$. The decay width difference and mixing frequency $\Delta\Gamma_s < 0$ and $\Delta m_s > 0$ are chosen as defined in the previous section. For this parametrization, it is assumed that $|q/p| = 1$, i.e. there is no CP violation in the B_s^0 mixing. This assumption is reasonable since CP violation in the mixing of neutral B mesons is predicted to be of the order $\mathcal{O}(10^{-4})$ in the Standard Model, which is in agreement with a dedicated LHCb measurement [38]. The CKM angle γ appears in the interference terms of the decay rate shown in Equation 3.56, together with the $B_s^0 - \bar{B}_s^0$ mixing phase β_s. This means that an unambiguous determination of γ is possible when β_s is taken as an input from dedicated measurements [28].

The dimensionality of the decay rate, defined in Equation 3.56, is regulated by the phase space element $\mathrm{d}\Phi_4$. It is defined in terms of the set of five independent kinematic observables chosen to label each phase space point $\vec{x}$,

$$\mathrm{d}\Phi_4 = \phi_4(\vec{x})\mathrm{d}^5x, \tag{3.57}$$

with $\phi_4(\vec{x}) = |\frac{\partial\Phi_4}{\partial(x_1,\ldots x_5)}|$ being the phase space density. Since the four-body phase space density is not flat in the kinematic variables [3], an analytic expression for ϕ_4 is taken from [39]. The model-dependent description of the intermediate state amplitudes is discussed in the next Section 3.3.2.

For a model-independent description of this decay, the differential decay rate given in Equation 3.56 can be integrated across the phase space Φ_4, effectively averaging over the contributing hadronic amplitudes $\mathcal{A}_f^c(\vec{x})$ and $\mathcal{A}_f^u(\vec{x})$. In order to describe the phase-space integrated decay rate, one defines

$$r \equiv \frac{\sqrt{\int |\mathcal{A}_f^u(x)|^2 \, d\Phi_4}}{\sqrt{\int |\mathcal{A}_f^c(x)|^2 \, d\Phi_4}} \tag{3.58}$$

as the ratio of the Cabibbo suppressed ($b \to u$) over the Cabibbo favored ($b \to c$) amplitudes and

$$\kappa \equiv \frac{\int \mathcal{A}_f^c(x)^* \, \mathcal{A}_f^u(x) \, d\Phi_4}{\sqrt{\int |\mathcal{A}_f^c(x)|^2 \, d\Phi_4} \sqrt{\int |\mathcal{A}_f^u(x)|^2 \, d\Phi_4}} \, e^{-i\delta} \tag{3.59}$$

as the hadronic coherence factor, which quantifies the dilution of the sensitivity to the weak phases in Equation 3.56, due to the integration over interfering hadronic amplitudes across the available phase space. The value of κ is constrained to lie within [0...1]. In Equation 3.59, δ is defined as the strong phase difference between those amplitudes. Using the definitions of δ, κ and r, the phase-space integrated decay rate can be written as:

$$\begin{aligned} \int \frac{\mathrm{d}\Gamma(\vec{x}, t, q, f)}{\mathrm{d}t \, \mathrm{d}\Phi_4} \, \mathrm{d}\Phi_4 \propto \; & e^{-\Gamma_s t} [\cosh\left(\frac{\Delta\Gamma_s \, t}{2}\right) + q \, f \, \frac{1 - r^2}{1 + r^2} \cos\left(\Delta m_s \, t\right) \\ & - \frac{2 \, r \, \kappa \cos\left(\delta - q \, (\gamma - 2\beta_s)\right)}{1 + r^2} \sinh\left(\frac{\Delta\Gamma_s \, t}{2}\right) \\ & - q \, f \, \frac{2 \, r \, \kappa \sin\left(\delta - q \, (\gamma - 2\beta_s)\right)}{1 + r^2} \sin\left(\Delta m_s \, t\right)]. \end{aligned} \tag{3.60}$$

As observed in Equation 3.60, the hadronic coherence factor κ appears in the interference terms sensitive to the weak phases γ and β_s. A value for κ equal to one would be reached in the limit of only one dominating intermediate hadronic amplitude contributing to the $B_s^0 \to D_s^- K^+ \pi^- \pi^+$ decay. For this case, the statistical power of the analyzed sample, and with that the sensitivity to γ and β_s, would be undiluted. In the case of $\kappa = 0$, the interference terms would vanish and the model-independent measurement would not be sensitive to γ and β_s at all.
Using the conventions of the CP observables chosen in the closely related analysis of

$B_s^0 \to D_s^- K^+$ decays [4], one defines:

$$C = \frac{1 - r^2}{1 + r^2} \tag{3.61}$$

$$D_f = -\frac{2\, r\, \kappa \cos\left(\delta - f\left(\gamma - 2\beta_s\right)\right)}{1 + r^2}, \tag{3.62}$$

$$S_f = f\, \frac{2\, r\, \kappa \sin\left(\delta - f\left(\gamma - 2\beta_s\right)\right)}{1 + r^2}. \tag{3.63}$$

With that, the phase space integrated decay rate given in Equation 3.60 can be expressed similarly to the general decay rates for a B_s^0 ($\bar{B}_s^0$) decay 3.50 (3.51) with CP violation in the interference of mixing and decay, developed in Chapter 3.2.3, despite the fact that the $(D_s^- K^+ \pi^- \pi^+)$ final state is not a CP eigenstate of the B_s^0 and different amplitudes $\mathcal{A}_f^c(\vec{x})$ and $\mathcal{A}_f^u(\vec{x})$ are contributing to the decay. Using C, D_f and S_f defined above, the decay rate can be written as:

$$\begin{aligned}\int \frac{\mathrm{d}\Gamma(\vec{x}, t, q, f)}{e^{-\Gamma_s t}\, \mathrm{d}t\, \mathrm{d}\Phi_4}\, \mathrm{d}\Phi_4 \propto\ & \cosh\left(\frac{\Delta\Gamma_s\, t}{2}\right) + q\, f\, C \cos\left(\Delta m_s\, t\right) \\ & + D_f \sinh\left(\frac{\Delta\Gamma_s\, t}{2}\right) - q\, S_f \sin\left(\Delta m_s\, t\right).\end{aligned} \tag{3.64}$$

The CP parameters C, D_f, $D_{\bar{f}}$, S_f and $S_{\bar{f}}$ are the quantities measured in the presented model-independent analysis, from which the CKM angle γ is determined.

3.3.2. Amplitude model

To set up the amplitude model for the $B_s^0 \to D_s^- K^+ \pi^- \pi^+$ decay, it is crucial to correctly construct the intermediate state amplitudes $A_i(\vec{x})$. For this the isobar approach is used, assuming that the decay process can be factorized into subsequent two-body decays [40, 41, 42]. The isobar approach gives rise to two kinds of decay topologies, where one is a quasi two-body decay of the form

$$B_s^0 \to (R_1 \to h_1 h_2)(R_2 \to h_3 h_4) \tag{3.65}$$

and the other is a cascade decay of the form

$$B_s^0 \to h_1 [R_1 \to h_2 (R_2 \to h_3 h_4)]. \tag{3.66}$$

For both forms, R_i is the resonance describing the particular intermediate amplitude

and h_j are the final state hadrons. In both cases, the intermediate state amplitudes are parametrized by their angular orbital momentum L, form factors B_L for each vertex of the (cascade or quasi two-body) decay tree, a Breit-Wigner propagator T_R for each resonance R and the overall angular momentum structure of each intermediate amplitude, described by a so-called spin factor S [2]:

$$A_i(\vec{x}) = B_{L_{B_s}}(\mathbf{x})\,[B_{L_{R_1}}(\vec{x})\,T_{R_1}(\vec{x})]\,[B_{L_{R_2}}(\vec{x})\,T_{R_2}(\vec{x})]\,S_i(\vec{x})\,. \tag{3.67}$$

This set of parameters is briefly discussed in the following. A thorough description of all parameters can be found in [3].

Form factors

To account for the finite size of the intermediate resonances $R_{1,2}$ and their orbital angular momentum L, the form factors $B_{L_{R_i}}$ are introduced. A square well interaction potential with radius r_{BW} and the breakup momentum q is chosen to model the (cascade or quasi two-body) decay of R_1 and R_2, from which the Blatt-Weisskopf penetration factors [43] are derived and used as analytical representation of the angular momentum dependent form factors $B_L(q, r_{BW})$. Their explicit form for relative angular orbital momenta of $L = 0, 1, 2$ between the resonance daughters is given as

$$\begin{aligned} B_0(q, r_{BW}) &= 1, \\ B_1(q, r_{BW}) &= 1/\sqrt{1 + (q\,r_{\mathrm{BW}})^2}, \\ B_2(q, r_{BW}) &= 1/\sqrt{9 + 3\,(q\,r_{\mathrm{BW}})^2 + (q\,r_{\mathrm{BW}})^4}, \end{aligned} \tag{3.68}$$

effectively suppressing contributions from resonances with higher relative angular orbital momenta, $B_2(q, r_{BW}) < B_1(q, r_{BW}) < B_0(q, r_{BW})$.

Propagators

The propagators of the different resonant contributions are described in terms of the energy transfer squared, s, as well as the total decay width $\Gamma(s)$ which is normalized to give the nominal width Γ_0 of the respective resonance, when evaluated at its nominal mass m_0, $\Gamma(m_0) \equiv \Gamma_0$. The analytic form of the propagators is given by a relativistic Breit-Wigner shape with energy depended width,

$$T(s) = \frac{1}{m_0^2 - s - i\, m_0\, \Gamma(s)}\,. \tag{3.69}$$

Different expressions for the total widths $\Gamma(s)$ are needed for the the amplitudes containing quasi two-body decays, $\Gamma^{(2)}_{R\to h_1 h_2}(s)$, or the three-body transition $\Gamma^{(2)}_{R\to h_1 h_2 h_3}(s)$. While there is an analytical expression for the two-body decay [44],

$$\Gamma^{(2)}_{R\to h_1 h_2}(s) = \Gamma_0\, \frac{m_0}{\sqrt{s}} \left(\frac{q}{q_0}\right)^{2L+1} \frac{B_L(q)^2}{B_L(q_0)^2}\,, \tag{3.70}$$

where q_0 denotes the value of the breakup energy at the resonance pole, no general analytical expression is available for the three-body case. The decay width can however be determined numerically by integrating the transition amplitudes $|A_{R\to h_1 h_2 h_3}|$ over the phase space,

$$\Gamma^{(3)}_{R\to h_1 h_2 h_3}(s) = \frac{1}{2\sqrt{s}} \int |A_{R\to h_1 h_2 h_3}|^2\, \mathrm{d}\Phi_3. \tag{3.71}$$

The technical details of this integration, as well as the choice of propagator models for each resonance, are discussed in detail in [5].

Spin factors

The spin factors are a phenomenological description of the angular structure of the intermediate decay processes which need to be Lorentz invariant, as well as conserving angular momentum and parity. They are constructed using the covariant Zemach [45] and Rarita-Schwinger [46, 47] tensor formalism. In the following, a brief summary of the derivation of the spin factors is given. Further details on the procedure can be found in [48, 49].

A particle having spin-S with four-momentum p, and spin projection λ, is represented by the polarization tensor $\epsilon_{(S)}(p,\lambda)$, which is symmetric, traceless and orthogonal to p. These Rarita-Schwinger conditions reduce the 4^S elements of the rank-S tensor to $2S+1$ independent elements, in accordance with the number of degrees of freedom of a spin-S state[46, 50]. The spin projection operator $P^{\mu_1\dots\mu_S\nu_1\dots\nu_S}_{(S)}(p_R)$, for a resonance R with spin $S = \{0, 1, 2\}$ and the four-momentum p_R, is given by [49]:

$$
\begin{aligned}
P^{\mu\nu}_{(0)}(p_R) &= 1 \\
P^{\mu\nu}_{(1)}(p_R) &= -g^{\mu\nu} + \frac{p^\mu_R\, p^\nu_R}{p^2_R} \\
P^{\mu\nu\alpha\beta}_{(2)}(p_R) &= \frac{1}{2}\left[P^{\mu\alpha}_{(1)}(p_R)\, P^{\nu\beta}_{(1)}(p_R) + P^{\mu\beta}_{(1)}(p_R)\, P^{\nu\alpha}_{(1)}(p_R)\right] - \frac{1}{3}\, P^{\mu\nu}_{(1)}(p_R)\, P^{\alpha\beta}_{(1)}(p_R)\,,
\end{aligned}
\tag{3.72}
$$

where $g^{\mu\nu} = \mathrm{diag}(+1, -1, -1, -, 1)$ is the metric of Minkowski space. Contracted with an arbitrary tensor, the projection operator selects the part of the tensor which satisfies the Rarita-Schwinger conditions. For a decay process $R \to h_1 h_2$, with relative orbital angular momentum L between the final state particles h_1 and h_2, the angular momentum tensor is obtained by projecting the rank-L tensor $q^{\nu_1}_R\, q^{\nu_2}_R \ldots q^{\nu_L}_R$, constructed from the relative momenta $q_R = p_A - p_B$, onto the spin-L subspace,

$$
L_{(L)\mu_1\ldots\mu_L}(p_R, q_R) = (-1)^L\, P_{(L)\mu_1\ldots\mu_L\nu_1\ldots\nu_L}(p_R)\, q^{\nu_1}_R \ldots q^{\nu_L}_R. \tag{3.73}
$$

Following the isobar approach, each two-body decay $R \to h_1 h_2$ with relative orbital angular momentum $L_{h_1h_2}$ and intrinsic spin $S_{h_1h_2}$ contributes a term to the overall spin factor of the respective amplitude of the form

$$
S_{R\to h_1h_2}(L_{h_1h_2}, S_{h_1h_2}; \lambda_R, \lambda_{h_1}, \lambda_{h_2}) \propto \epsilon_{(S)}(p_R, \lambda_R)\, L_{(L_{h_1h_2})}(p_R, q_R).
$$

The spin factor for the complete decay chain, i.e. for the case $B^0_s \to (R_1 \to h_1h_2)(R_2 \to h_3h_4)$, is given by the sum over all intermediate spin projections,

$$
\sum_{\lambda_{R_1},\lambda_{R_2}} S_{R\to R_1R_2}(\mathbf{x}|L_{R_1R_2}; \lambda_{R_1}, \lambda_{R_2})\, S_{R_1\to h_1h_2}(\mathbf{x}|L_{h_1h_2}; \lambda_{R_1})\, S_{R_2\to h_3h_4}(\mathbf{x}|L_{h_3h_4}; \lambda_{R_2}). \tag{3.74}
$$

3.3.3. Experimental status

The $B^0_s \to D^-_s K^+\pi^-\pi^+$ decay was first observed in 2012 by the LHCb collaboration, using a data sample that consists of $1 fb^{-1}$ of integrated luminosity, collected during Run I of the LHC in the year 2011 at a center of mass energy of $\sqrt{s} = 7\ TeV$ [51]. A measurement of the branching ratio of this decay relative to the $B^0_s \to D^-_s\pi^+\pi^-\pi^+$ channel was performed:

$$\frac{\mathcal{B}(\bar{B}_s^0 \to D_s^+ K^- \pi^+ \pi^-)}{\mathcal{B}(\bar{B}_s^0 \to D_s^+ \pi^- \pi^+ \pi^-)} = (5.2 \pm 0.5 \pm 0.3) \cdot 10^{-2}, \tag{3.75}$$

where the first uncertainty is statistical and the second is systematic. Using the absolute branching ratio of $B_s^0 \to D_s^- \pi^+ \pi^- \pi^+$ decays [20], the ratio of $B_s^0 \to D_s^- K^+ \pi^- \pi^+$ decays with respect to all possible B_s^0 decay channels can be computed:

$$\mathcal{B}(\bar{B}_s^0 \to D_s^+ K^- \pi^+ \pi^-) = (3.2 \pm 0.6) \cdot 10^{-4}, \tag{3.76}$$

where the statistical error, as well as the systematic uncertainty and the uncertainty on the absolute $B_s^0 \to D_s^- \pi^+ \pi^- \pi^+$ branching ratio is combined. Due to the low statistics available for the first observation, no search for CP violation was performed.

Chapter 4

The LHCb Experiment

Modern high-energy physics experiments require sophisticated tools and instruments to measure properties of sub-atomic particles. The presented analysis is performed using data provided by the Large Hadron Collider beauty (LHCb) collaboration. This chapter describes the LHCb detector, which is one of the four major experiments located at the Large Hadron Collider (LHC). It is dedicated to precision measurements of parameters within the flavor sector of the Standard Model. Most prominently, LHCb performs world's best measurements of CP violation in b-and c-hadron decays.

4.1. The Large Hadron Collider

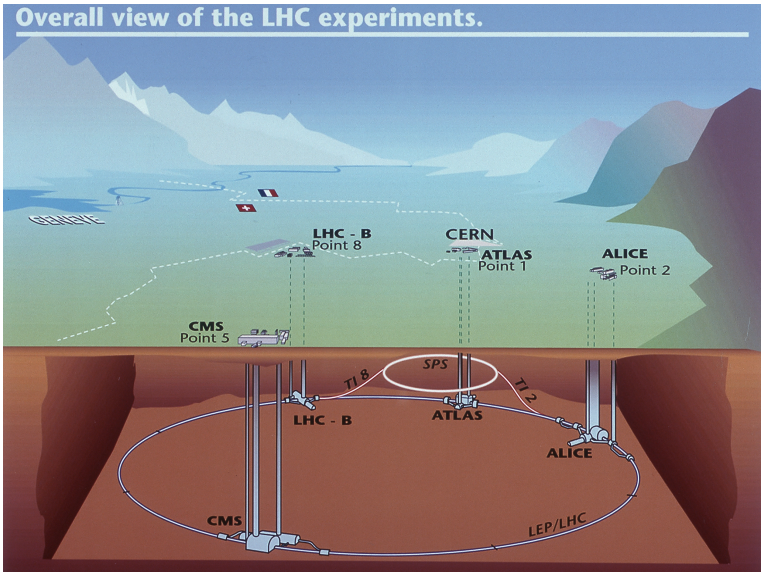

Figure 4.1.: Schematic view of the LHC taken from [52].

The LHC is the world's largest particle accelerator, located at the European Laboratory for Particle Physics CERN in Geneva. It is a proton-proton ring collider with a circumference of approximately 27 km and a designed center of mass energy of up to $\sqrt{s} = 14$ TeV, making it the first machine to reach this energy scale. The four major experiments ATLAS (A Toroidal LHC Apparatus), CMS (Compact Muon Solenoid), ALICE (A Large Ion Collider Experiment) and LHCb are located at the four proton interaction points, which can be seen in a schematic overview in Figure 4.1. A proton beam is divided into bunches, where each bunch roughly contains 10^{11} protons. Through a chain of accelerator facilities (Linac, PS, SPS) the protons are pre-accelerated to 450 GeV [53] and injected into the LHC, where they are further accelerated to the design energy of up to 7 TeV. At the interaction points, some protons of a bunch interact with protons in the oppositely circulating bunch. During a fill, the number of simultaneously circulating bunches can reach up to 2808, leading to an instantaneous luminosity of $\mathcal{L} = 10^{34} cm^{-2} s^{-1}$ [54]. At a bunch spacing of 25 ns, this results in a bunch-crossing rate of 40 MHz.

The data used in this analysis was taken during the first and second run of the LHC in the years 2011 & 2012 (Run I) and 2015, 2016 & 2017 (Run II). During the first run, the LHC was operating at a center of mass energy of 7 (2011) and 8 (2012) TeV and the integrated luminosity recorded by LHCb in these years amounts to $\mathcal{L}_{Run\ \mathrm{I}} = 3\mathrm{fb}^{-1}$. During the first three years of the second run, the LHC increased the center of mass energy to $\sqrt{s} = 13$ TeV, and LHCb collected an integrated luminosity of $\mathcal{L}_{15-17} = 3.7\mathrm{fb}^{-1}$. In total, the data used for this analysis corresponds to an integrated luminosity of $\mathcal{L} \approx 6.7 fb^{-1}$. The delivered and collected integrated luminosity for the years 2010-2017 is shown in Figure 4.2.

4.2. Beauty hadrons at the LHC

Beauty quarks are dominantly produced in gluon fusion and quark-anti-quark annihilation at the LHC. The leading order Feynman diagrams for these processes are shown in Figure 4.3, where a) corresponds to the annihilation process and b)-d) to gluon fusion. At LHC energies, the processes b)-d) are the by far dominating contributions to the production of beauty quarks [55]. A produced b quark can hadronize and form a charged or neutral B meson or a Λ_b^0 baryon. Due to the low energy threshold of $b\bar{b}$ pair production of approximately 8.5 GeV, compared to the large center of mass energy, it is likely that gluons with very different momenta annihilate to a pair of beauty quarks. This results

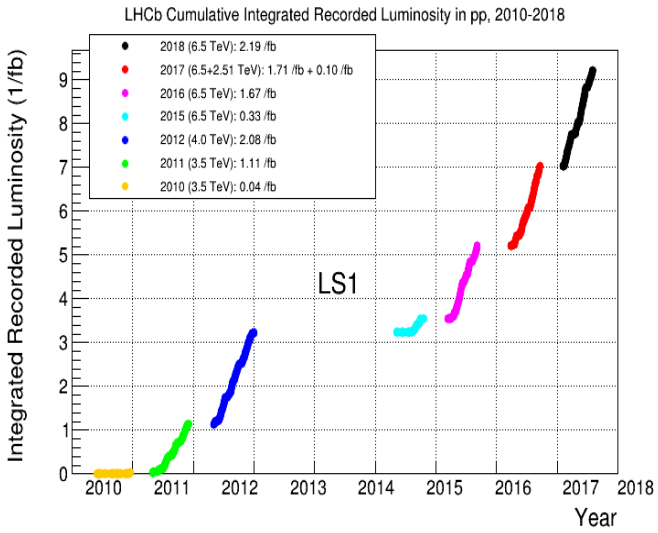

Figure 4.2.: Recorded integrated luminosity by LHCb for the years 2010-2018 [52].

into a boost in the lab system and the majority of $b\bar{b}$ pairs being emitted along the z-direction close to the beam axis. As a consequence of this boost, the average flight distance of a b-hadron is on the scale of 1 cm, allowing for the precise decay-time resolution of the LHCb detector. The right hand side of Figure 4.3 shows the simulated polar angle distribution $\theta_{1,2}$ of the b and $\bar{b}$ quarks at $\sqrt{s} = 14$ TeV. The spatial distributions of b and $\bar{b}$ quarks clearly peak in the $\theta = 0°$ (forward) and $\theta = 180°$ backward direction of the beam axis. Regarding this fact, the LHCb detector is build as a single-arm forward spectrometer as shown in Figure 4.4. Approximately 25% of the produced $b\bar{b}$ pairs lie inside the LHCb detector acceptance.

4.3. The LHCb Detector

The LHCb detector is positioned in a cavern 100 m underground at a CERN facility near Ferney Voltaire, France. A schematic view of the LHCb Detector is shown in Figure 4.4. This section will summarize the individual detector components [57], which can generally be divided into components for tracking and for particle identification.

The region of the proton-proton interactions is surrounded by the Vertex Locator (VELO), which is a silicon strip detector that provides excellent spatial resolution of the vertices of proton-proton interactions and the displaced decay vertices of charm and beauty hadrons. Two additional tracking systems are placed farther downstream in the detector to track the signature of the charged decay products of the b and c hadrons.

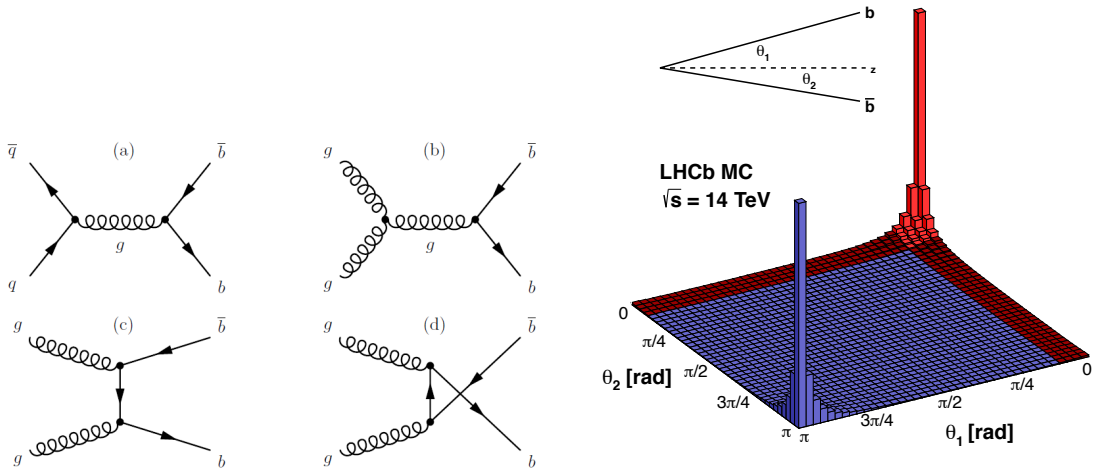

Figure 4.3.: (left) Leading order Feynman diagrams for $b\bar{b}$ production at the LHC [56] and (right) simulated distribution of the polar angles θ_1 and θ_2 of $b\bar{b}$ quark pairs. The geometrical acceptance of the LHCb detector is indicated in red [52].

The Tracker Turicensis (TT) is located upstream of the dipole magnet, giving information about particle tracks before they are bent in the magnetic field. Behind the magnet, the tracking stations (T1-T3) give information on particle trajectories after the bending, allowing for the measurement of their momenta. T1-T3 are divided into the Inner Tracker (IT), made of silicon strips, covering the part of the detector around the beam axis where particle multiplicities are high, and the Outer Tracker (OT), consisting of straw-tube gas detectors, covering the outer region of the detector. The dipole magnet bends the tracks of charged particles in the x-z plane, where the z-direction is defined by the beam line.

There are two ring-imaging Cherenkov detectors (RICH1,RICH2) used for particle identification. RICH1 is located behind the VELO, upstream of the dipole magnet and RICH2 is situated downstream of the tracking stations T1-T3. These detectors are able to distinguish between incoming pions, kaons and protons by the angle under which the particles emit Cherenkov radiation. Located downstream of RICH2 are the Pre-Shower (PS) and the Scintillating Pad Detector (SPD). They are followed by the electromagnetic and hadronic calorimeters (ECAL and HCAL) in which particles deposit energy via electromagnetic or hadronic showers. Apart from the energy measurement, the calorimeter

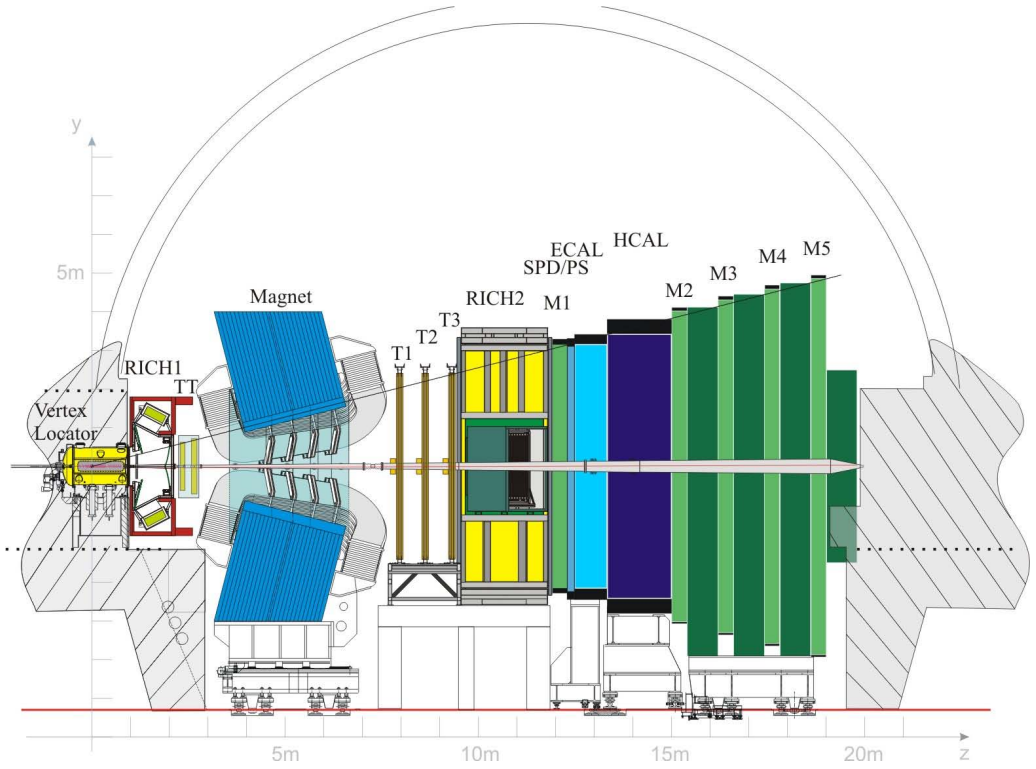

Figure 4.4.: Schematic side view of the LHCb-detector taken from [52]. The proton-proton collision takes place on the left, inside the Vertex Locator VELO; RICH1 and RICH2 are ring-imaging Cherenkov detectors; TT is the Tracker Turicensis, T1 - T3 the main tracking system, SPD is the Scintillating Pad Detector and PS the Preshower detector; ECAL is the electromagnetic calorimeter, HCAL the hadronic calorimeter and M1 - M5 the muon chambers. All mentioned components of the LHCb detector are discussed in the text.

system provides trigger signals for further analysis of the detector output. Five chambers at the end of the detector (M1-M5), composed of multi-wire proportional chambers (MWPC) and, in case of M1, triple-gas electron multipliers (GEM), are dedicated to the detection of muons. They are used to identify and give additional tracking information on muons, where M1 is placed in front and M2-M5 are placed behind the calorimeters. Due to the fact that these leptons interact very weakly with the detector material, they are the only particles expected to penetrate M2-M5.

4.3.1. Tracking detectors

A charged particle leaves signatures in the VELO, the TT before and in the tracking stations T1-T3 after the dipole magnet. With this information, the trajectory of the particle can be reconstructed and the bending of the track due to the dipole magnet is used to measure its momentum. It should be noted that the polarity of the magnet can be reversed in order to study detection asymmetries for charged particles. Additionally, the spatial resolution of the pp interaction point and the displaced b,c hadron decay vertex in the VELO allows for the determination of the decay time of the respective hadron.

Vertex Locator

The VELO consists of disk-shaped silicon modules and surrounds the pp interaction point. At each station, two sub sensors are used to measure the radial and azimuthal coordinates R and ϕ of a charged particle with a minimal pitch of 40 μm across the sensors [58]. The VELO is used to precisely determine the particle tracks produced in the pp interaction and to distinguish these from tracks originating from a secondary vertex, which is produced when a particle with significant lifetime decays. The VELO is arranged along the beam axis to detect heavy-flavor hadrons. Figure 4.5 gives a schematic overview of the VELO geometry.

Tracker Turicensis

The TT consists of four detector layers which are installed in pairs called (x,u) and(v,x) stations. The layers are made of silicon microstrip sensors, which are suitable to handle the high particle multiplicity in front of the dipole magnet. To achieve additional spatial resolution in the y-direction, the u and v layer are rotated by an angle of $\pm 5^\circ$ with respect to the two vertical x layers. Figure 4.6 visualizes the geometry and the length scale of the TT. The single hit resolution of a single track is approximately $50 \mu m$ [54].

The Inner and Outer Tracker

The IT and OT are located behind the magnet with the IT covering the high occupancy area around the beam axis and the OT covering the outer region of the detector.
The IT consists of silicon microstrip sensors similar to the TT. Each of the three stations T1-T3 consists of four layers following a (x,u,v,x) scheme, where the u and v layers are rotated by $\pm 5^\circ$ with respect to the x layers. Figure 4.7 visualizes the geometry and length scale of one IT x layer. The spatial single hit resolution is comparable to the TT

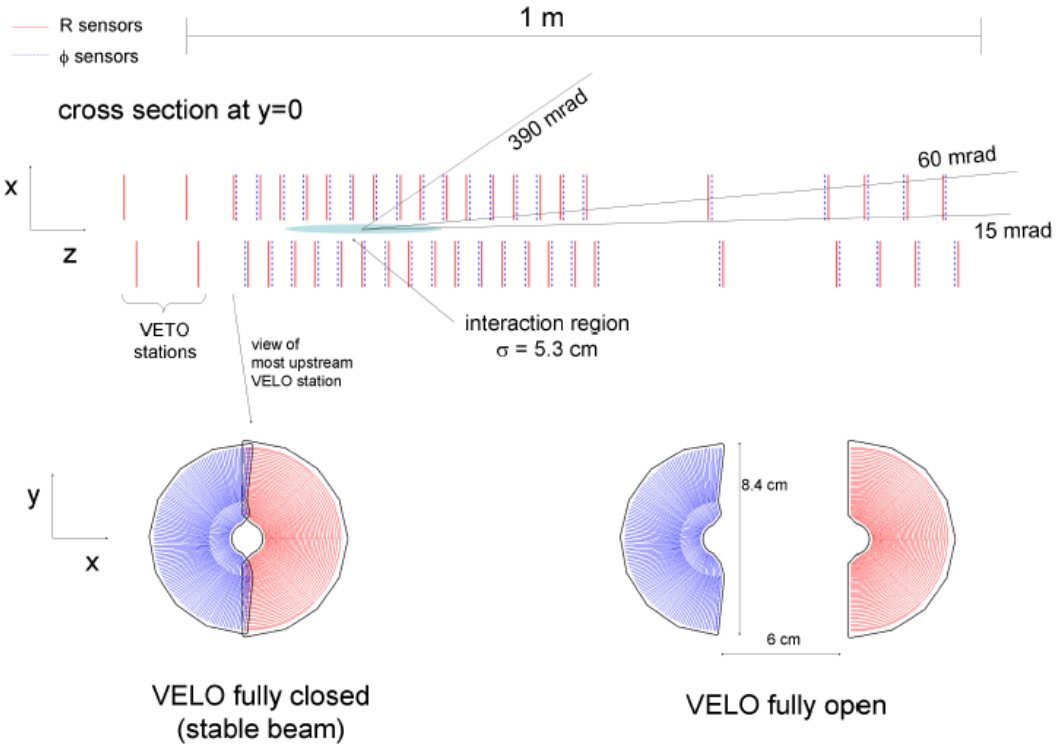

Figure 4.5.: (top) Geometry of the LHCb VELO along the beam pipe and (bottom) sketch of a silicon disk with (blue) R and (red) ϕ sensors. Images taken from [57].

with approximately $50\mu m$ [54].

The OT is built as a gas detector with straw tubes and filled with a mixture of Argon, CO_2 and oxygen. It covers the large outer detector region of $6 \cdot 5\ m = 30\ m^2$ and achieves a spatial hit resolution of approximately $200\mu m$, while exhibiting a maximum drift time of approximately 45 ns [60]. The layout of the OT modules, as well as the arrangement of the tubes inside the OT, is shown in Figure 4.8.

Track reconstruction

In the first step, a pattern recognition software assigns hits in the different tracking systems to a track. After that, the tracks are fit by an implementation of a Kalman filter algorithm [61] which accounts for multiple scattering of individual particles. As a measure of the fit quality, the track fit χ^2 is divided by the number of degrees of freedom of the fit $n_{d.o.f.}$ and saved along with the reconstructed track. For a good quality fit, one expects $\chi^2/n_{d.o.f} \approx 1$.

At LHCb, a track is categorized by the tracking systems in which it can be reconstructed

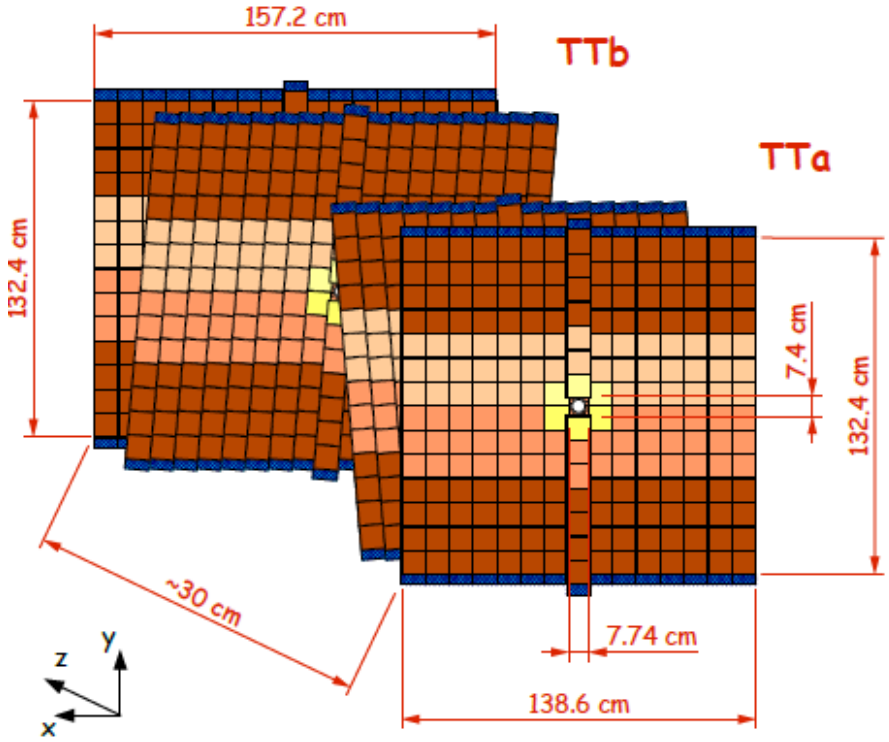

Figure 4.6.: Sketch of the geometry and length scale of the TT taken from [59].

by the pattern recognition. Tracks with the highest momentum resolution are so-called long tracks, with hits in the VELO and the main tracking stations T1-T3. Due to the long lever arm, they can be reconstructed with a momentum resolution ranging from $\sigma(p)/p = 0.35\%$ for low-momentum tracks ($p < 20\ GeV$) to $\sigma(p)/p = 0.55\%$ for the highest-momentum tracks ($p > 120\ GeV$) [57]. The other two categories are upstream tracks, which are reconstructed from hits in the VELO and the TT and downstream tracks, which are reconstructed in the TT and the tracking stations T1-T3.
The combined track reconstruction efficiency for tracks in the momentum region from 5 GeV to 200 GeV (majority of tracks at LHCb) is about 95 % [62].

4.3.2. Particle identification

For every data analysis, it is crucial to determine the particle type associated with a reconstructed track. At LHCb, this is achieved using the combined information of the Ring-Imaging Cherenkov Detectors (RICH 1 & RICH 2), the calorimeter systems (PS, SPD, ECAL & HCAL) and the muon chambers (M1-M5).

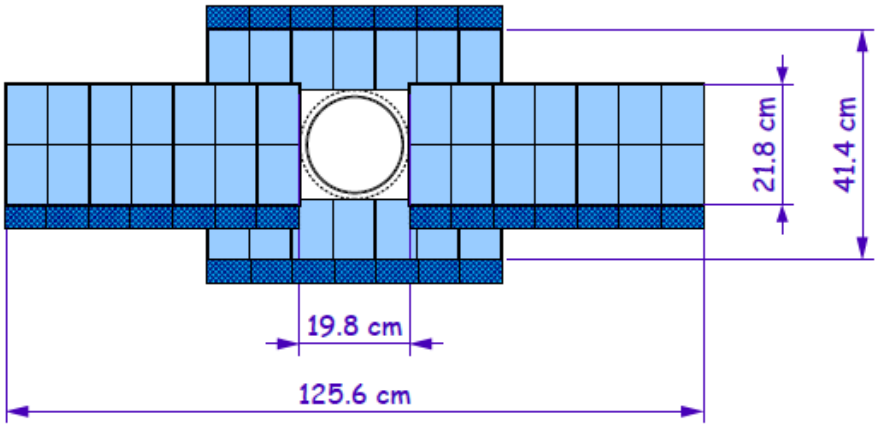

Figure 4.7.: Geometry and length scale of an IT x layer. Figure taken from [59].

Ring Imaging Cherenkov Detectors

The RICH Detectors are used to identify charged particles based on Cherenkov radiation. A particle that traverses a medium faster than the speed of light in this medium $c^{'} = \frac{c}{n}$, where c is the speed of light in vacuum and n is the refractive index of the particular medium, emits photons under an angle ϑ that is directly related to the particles velocity by

$$cos(\vartheta) = \frac{1}{\beta n} = \frac{c^{'}}{v}, \tag{4.1}$$

where $\beta = \frac{v}{c}$ is the velocity fraction with respect to the speed of light in vacuum.
The Cherenkov light is guided through the RICH using mirrors until it reaches the Hybrid Photo Detectors (HPD). Photons emitted by a charged particle form a cone which is then detected as a ring, where the radius of the ring is proportional to the cone angle ϑ under which the photons were radiated and thus a measure of β. Together with the momentum information from the tracking stations, the rest mass of the particle can be determined:

$$m_0 = \frac{p}{\beta\gamma}, \tag{4.2}$$

where $\gamma = \frac{1}{\sqrt{1-\beta^2}}$. The knowledge of the rest mass allows the determination of the particle type. For the purpose of LHCb, the charged particles which have to be identified and separated from each other by the RICH detectors are mainly muons, pions, kaons and protons.

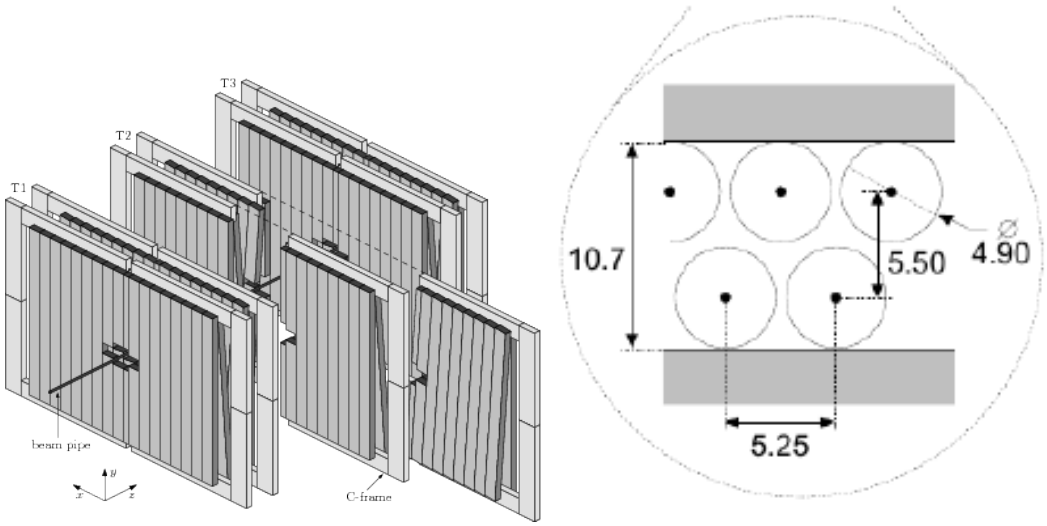

Figure 4.8.: (left) Sketch of the arrangement of the OT modules and (right) layout of the straw tubes inside an OT module. All numbers are given in mm [60].

RICH1 uses C_4F_{10} as medium and is located upstream of the dipole magnet, covering a momentum range from approximately 1 to 60 GeV/c. RICH2 is placed behind the main tracking stations and covers the higher momentum range from approximately 15 to 100 GeV/c, using the optical dense CF_4 gas [57]. The geometry of the RICH1 detector, as well as the distribution of measured Cherenkov angles as function of the momentum of the respective particle species, is shown in Figure 4.9.

Calorimeters

With the calorimeter system photons, electrons and hadrons can be identified and, as they are mostly stopped inside the calorimeters, their energy can be measured from the deposited energy. The calorimeters use the fact that an incoming particle produces a shower of secondary particles in the thick metal absorber layers and light in the interleaved plastic scintillators, which is then detected using Photo Multiplier Tubes (PMTs). The four components of the calorimeter system in the LHCb detector are the Preshower Detector (PS), the Scintillator Pad Detector (SPD), the Electromagnetic Calorimeter (ECAL) and the Hadronic Calorimeter (HCAL) [64]. Their alignment is shown in Figure 4.4.

The SPD consists of scintillating layers which are 15 mm thick. Its main purpose is to detect electrons with this setup. Photons are visible in the PS due to a 12 mm thick lead absorber between the SPD and the PS, where this absorber is used to induce electromagnetic showers inside the PS.

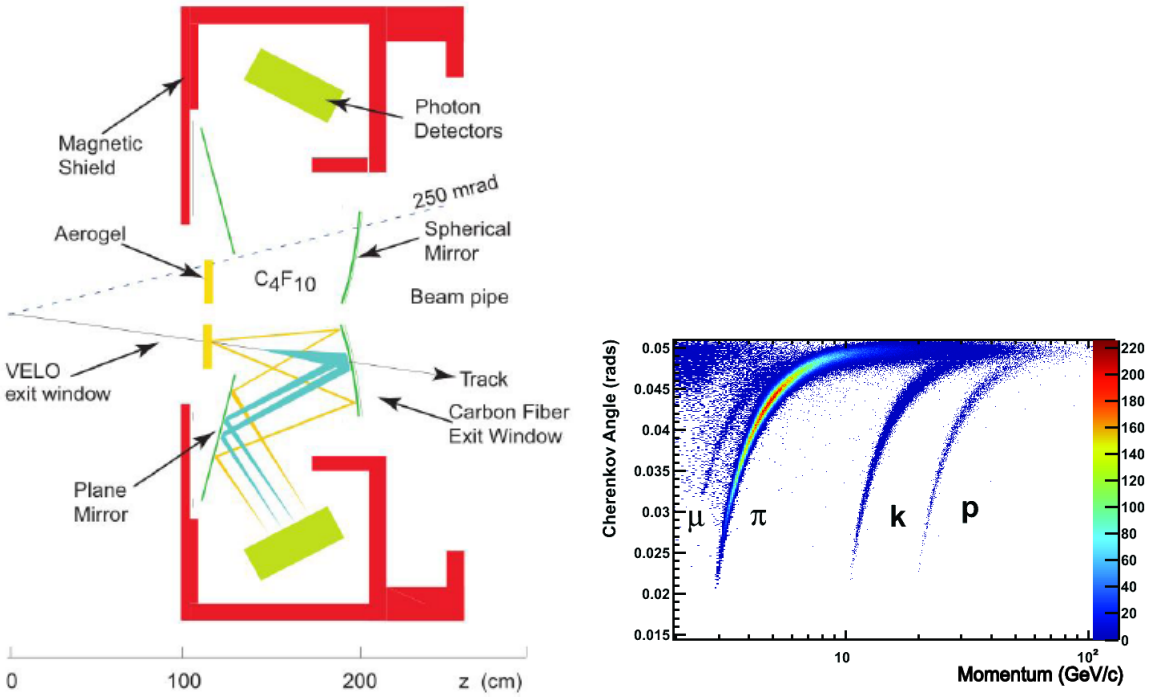

Figure 4.9.: (left) Geometry of the RICH1 detector (side view) taken from [57] and (right) Cherenkov angle as a function of the momentum of different hadron species, taken from [63].

The PS is built similarly to the SPD. It is used to distinguish between hadronic and electromagnetic showers using the fact that hadrons in general deposit very little energy in the calorimeter systems until they reach the HCAL.

The ECAL is composed of alternating layers of active material (4 mm thick scintillating pads) and absorbers (2 mm thick lead). With this specific design, the size of the ECAL can be held compact while it is likely that an electron or photon deposits its entire energy in the calorimeter, as the material thickness corresponds to 25 radiation lengths. It is also used to distinguish electrons and photons from hadrons, where the former are absorbed in the ECAL while the latter also cause a hadronic shower in the subsequent hadronic calorimeter (HCAL). Showers induced in the ECAL by electrons and photons via bremsstrahlung and e^+e^--pair production are detected by PMTs. The obtained energy resolution is [64]

$$\frac{\sigma(E)}{E} = \frac{10\%}{\sqrt{E}} \oplus 1.5\%, \tag{4.3}$$

where the $\oplus$ symbolizes quadratic summation and the energy is measured in GeV.

The HCAL is structured similarly to the ECAL with absorber layers of iron that are 1 cm thick. The total length of absorber and scintillating material corresponds to 5.6 hadronic interaction lengths and ensures that hadronic showers are initiated and can be detected. The energy resolution of the HCAL is [64]:

$$\frac{\sigma(E)}{E} = \frac{80\%}{\sqrt{E}} \oplus 10\%. \tag{4.4}$$

4.3.3. The muon system

Muons produced at LHCb are typically minimally ionizing, hardly affected by bremsstrahlung due to their large mass compared to the electron and do not interact via the strong nuclear force. Therefore, they pass mostly undisturbed through the LHCb detector and can be detected in a dedicated system. This system is comprised of the five muon stations M1-M5, where M1 is located in front of the calorimeters and M2-M5 are downstream of the calorimeters at the end of the detector. The muon chambers M2-M5 consist of Multi Wire Proportional Chambers (MWPCs) which use gaseous ionization detection to measure the trajectory of a muon. The M1 chamber is built differently due to the higher particle flux that is expected in its inner part where it consists of a gas electron multiplier (GEM) detector. The achieved momentum dependent muon identification probability is between 97% and 99% [65].

4.3.4. Event reconstruction

The information of all detector components is combined and used to fully reconstruct decay signatures of interest, e.g. for this analysis the $B_s^0 \to D_s^- K^+ \pi^- \pi^+$ decay. In natural units, the four momentum vector of a particle $\mathbf{p}$ can be expressed through the energy $E = \sqrt{m^2 + \vec{p}^2}$ and the three-momentum vector $\vec{p}$. The masses of the final state particles for the presented analysis are not directly measured at LHCb. Therefore, the value given by the PDG (particle data group [20]) corresponding to the respective particle hypothesis is assigned as particle mass. The resulting four momentum is then given by:

$$\mathbf{p} = (E, \vec{p}) = (\sqrt{m_{PDG}^2 + \vec{p}^2}, \vec{p}). \tag{4.5}$$

For the decay $B_s^0 \to D_s^- K^+ \pi^- \pi^+$, where $D_s^- \to h^+ h^- h^-$ with $h = K, \pi$, the tracks of the (hhh) triplet are used to reconstruct the decay vertex of the D_s^- mesons, while the other three tracks of the $(X_s^+ = K^+ \pi^+ \pi^-)$ system point to the decay vertex of the B_s^0

candidate. The four momentum $\mathbf{p}_{D_s^-}$ of the D_s^- meson is calculated as the sum of the three hadrons four momenta

$$\mathbf{p}_{D_s^-} = \mathbf{p}_{h_1^-} + \mathbf{p}_{h_2^+} + \mathbf{p}_{h_3^-}. \tag{4.6}$$

The information of all six tracks and the decay vertices of the D_s^- mesons and the X_s^+ system is combined to reconstruct the decay vertex of the B_s^0 meson. This vertex is also called secondary vertex (SV). Since the B_s^0 meson is directly produced in the pp collisions, the production vertex of the B_s^0 is the pp interaction point which is called primary vertex (PV). The four-momentum of the B_s^0 meson is computed using the reconstructed D_s^- and $(K^+\pi^+\pi^-)$ momenta:

$$\mathbf{p}_{B_s^0} = \mathbf{p}_{D_s^-} + \mathbf{p}_{K^+\pi^+\pi^-}. \tag{4.7}$$

Figure 4.10 shows the decay signature of $B_s^0 \to D_s^- X_s^+ \to h^+h^-h^-K^+\pi^+\pi^-$ decays.

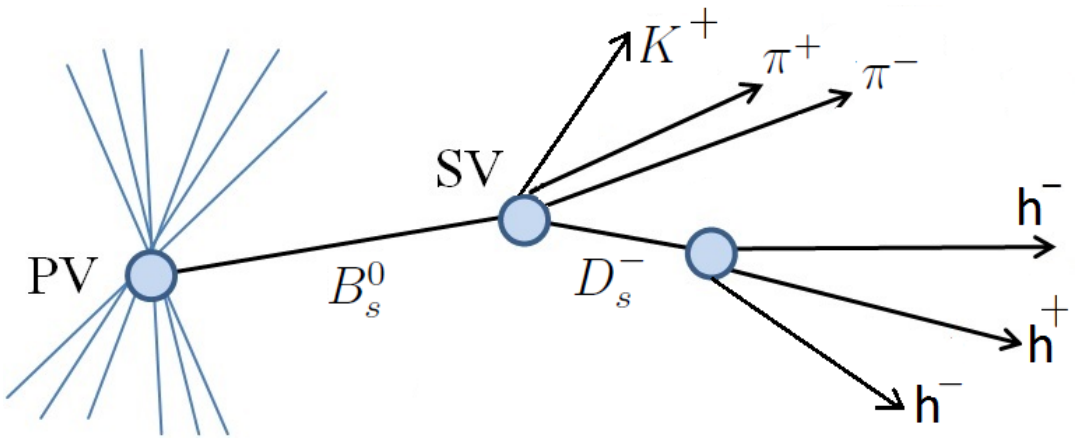

Figure 4.10.: Illustration of the reconstruction of the decay $B_s^0 \to D_s^- K^+\pi^-\pi^+$. PV is the primary vertex and SV the secondary vertex.

Once the decay signature is fully reconstructed, the decay time of the B_s^0 meson can be determined. Denoting $\vec{s_{pv}}$ as the spatial position vector of the primary vertex and $\vec{s_{sv}}$ as the spatial position vector of the secondary vertex, the flight distance s of the B_s^0 meson can be expressed as $|\vec{s}| = |\vec{s_{sv}} - \vec{s_{pv}}|$. Using the velocity $v = \beta = \frac{p}{E}$ (in natural units), the measured momentum $\vec{p}$ of the B_s^0, the relativistic dispersion relation $E = \sqrt{p^2 + m^2}$ and the Lorentz factor $\gamma = 1/\sqrt{1-\beta^2}$, the decay time t of the B_s^0 meson can be calculated as:

$$t = \frac{|\vec{s}|}{\gamma v} = \frac{|\vec{s}|}{\gamma \beta} = |\vec{s}|\sqrt{\frac{1}{\beta^2} - 1} = |\vec{s}|\sqrt{\frac{E^2}{p^2} - 1} = \frac{m|\vec{s}|}{|\vec{p}|} \overset{\vec{p}\parallel\vec{s}}{=} \frac{m\vec{s}\cdot\vec{p}}{|\vec{p}|^2} = \frac{m\cdot(\vec{s_{sv}} - \vec{s_{pv}})\cdot\vec{p}}{|\vec{p}|^2}. \tag{4.8}$$

4.3.5. The LHCb trigger system

Events used in this analysis are required to pass a hardware trigger stage, followed by the two software trigger stages of LHCb. The stages are designed to reduce the event rate from the nominal beam crossing rate of 40 MHz to roughly 5 (Run 1) or 12 (Run 2) kHz, filtering out events with decays of interest while rejecting others. The filtered events are recorded and saved on disk for physics analysis. Figure 4.11 shows the trigger scheme for the first two runs of LHCb.

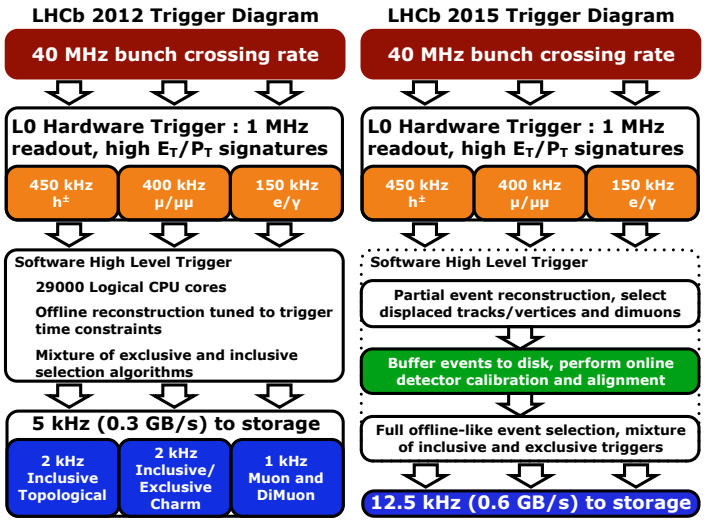

Figure 4.11.: LHCb Trigger scheme for data recorded in (left) Run I and (right) Run II, taken from [52].

Hardware Trigger

The first stage is the L0 hardware trigger which reduces the event rate to approximately 1.1 MHz. This is sufficient to enable the electronics to read out the whole LHCb detector. Since the B mesons mass is relatively high, the L0 trigger searches for final state particles with relatively high transverse energies E_t and momenta p_t, using information from the calorimeter system and the muon chambers. Signals in the calorimeter are used to form

clusters of cells, from which the the transverse energy of electrons, photons and hadrons can be measured. The muon trigger provides the reconstruction of tracks in the muon chambers and an estimate of the transverse momentum by using the slope of the track and an average pp collision point [66]. All available information is combined to assign a particle hypothesis to tracks accepted by the L0 trigger (L0-Hadron, L0-Photon, L0-Electron, L0-Muon). At LHCb, an event containing a signal candidate, for instance a B_s^0, can be triggered because of the signal B_s^0 candidate itself, which is called L0-TOS (triggered on signal), or by another trigger object that is not the signal candidate, which is called L0-TIS (triggered independent of signal). In both cases, the event is recorded and available for further analysis.

Software Trigger

The software trigger consists of two stages which are called the High Level Trigger HLT1 and HLT2. They are based on offline software applications utilizing large computing resources and time, which are used to precisely determine particles momenta and reconstruct vertices in a given event.

In the HLT1, events are partially reconstructed using the VELO information as well as information from the TT and T1-T3 stations with the purpose of fast track reconstruction. HLT1 uses the partial reconstruction to confirm trigger objects formed by the L0 stage. This procedure further reduces the event rate to roughly 30 kHz.

The HLT2 stage fully reconstructs events using all available information from the tracking and particle identification. At this stage, information from the RICH detectors is used to separate different hadron species and specific decay modes can be reconstructed using loose selection criteria. Tracks are reconstructed to meet requirements for certain composite particles, for example the combination of two muons to the decay $J/\psi \to \mu^+\mu^-$. The topological trigger lines in HLT2 attempt to reconstruct b-hadron decays with two or more particles in the final state by exploiting their typical topology of a small amount of tracks that exhibit large transverse momenta, large impact parameters to any PV and can be joined at a common vertex. With this stage, the event rate is reduced to the targeted rate, with which the data is reconstructed.

Chapter 5

Analysis strategy

In the presented analysis, the CP violation parameters C, D_f, $D_{\bar{f}}$, S_f and $S_{\bar{f}}$ are obtained from a fit to the reconstructed decay time of B_s^0 mesons, exploiting the decay-time dependent asymmetry between both states. The results, together with the B_s^0 mixing phase β_s as input, are used to determine the CKM angle γ, along with the ratio of decay amplitudes r and the strong phase difference δ.
For the extraction of the CP violation parameters, an unbinned maximum likelihood fit [67] of the theoretical $B_s^0 \to D_s^- K^+ \pi^- \pi^+$ decay rate, given by Equation 3.64, is performed to the measured B_s^0 and $\bar{B}_s^0$ decay-time distribution. Several intermediate steps are necessary to complete the fit model and obtain the final analysis sample:

- The six-particle final state is fully reconstructed to obtain a sample of $B_s^0 \to D_s^- K^+ \pi^- \pi^+$ signal candidates, where the D_s^- mesons are reconstructed in the final states $D_s^- \to K^- K^+ \pi^-$, $D_s^- \to K^- \pi^+ \pi^-$ and $D_s^- \to \pi^- \pi^+ \pi^-$. For the reconstruction, signals from the calorimeters are processed by the hardware trigger system to find hadrons with large transverse momentum that are identified by the RICH system as either kaons or pions. Consequently, the B_s^0 signal candidates are reconstructed and selected by requiring a displaced decay vertex, exploiting that they typically travel a significant distance away from the primary pp interaction point before decaying.

- Combinatorial and physical background is removed by a combination of selection requirements, that select signal-like B_s^0 hadrons while vetoing specific decays that could contribute as a possible background source. These requirements are followed by a multivariate analysis using machine learning tools to further discriminate signal-like and background-like event signatures. The residual background is determined by a fit to the invariant mass distribution of B_s^0 candidates and statistically subtracted for further analysis steps.

- The finite decay-time resolution of the measurement leads to a dilution of the $B_s^0 - \bar{B}_s^0$ oscillation and an effective damping of the CP violation parameters which needs to be accounted for. The decay-time resolution depends on the kinematics of the final-state particles and is determined from a study of fully simulated events (Run I) or using D_s^- mesons produced directly in the pp interaction (Run II).

- Due to the detector geometry, as well as the reconstruction and selection process, the measured decay-time distribution is deformed with respect to the theoretically predicted one. The decay-time acceptance model describes this efficiency as function of the measured B_s^0 decay time. It is determined using data from the control sample, consisting of $B_s^0 \to D_s^- \pi^+ \pi^- \pi^+$ decays, as well as simulated signal samples.

- To determine the time-dependent $B_s^0 - \bar{B}_s^0$ oscillation and the CP violation parameters, information on the initial flavor of the b-hadron is essential. The flavor can be determined using so-called tagging algorithms that exploit characteristic signatures of the hadronization of the signal b-quark, as well as signatures concerning the other b from the $b\bar{b}$ pair produced in the pp interaction. All used tagging algorithms are calibrated with a time-dependent maximum likelihood fit to $B_s^0 \to D_s^- \pi^+ \pi^- \pi^+$ candidates, taking advantage of the fact that for this decay the initial flavor is given by the charge distribution of the final state particles.

The first two steps listed above are crucial to obtain a pure sample of $B_s^0 \to D_s^- K^+ \pi^- \pi^+$ signal candidates, while the next three steps are essential as input for the time-dependent fit model. Additionally, a time-dependent amplitude fit model is developed that describes the intermediate hadronic structure of the $B_s^0 \to D_s^- K^+ \pi^- \pi^+$ decay in terms of the contributing amplitudes $\mathcal{A}_f^{b\to c}(\vec{x})$ and $\mathcal{A}_f^{b\to u}(\vec{x})$. For the time-dependent amplitude fit, in addition to the input described above, a model for the contributing hadronic resonances is determined.

Chapter 6

Selection of B_s^0 signal candidates

This Chapter summarizes the steps carried out to isolate the signal decays $B_s^0 \to D_s^- K^+\pi^-\pi^+$ and decays of the control channel $B_s^0 \to D_s^-\pi^+\pi^-\pi^+$ from the large LHCb dataset. The former B_s^0 decay channel is used to measure time-dependent CP violation, which allows for the determination of the CKM angle γ, while the latter is used as a calibration mode for the presented analysis. For both decay channels, the D_s^- meson is reconstructed in the three-body final states $D_s^- \to K^+K^-\pi^+$, $D_s^- \to K^+\pi^-\pi^+$ and $D_s^- \to \pi^+\pi^-\pi^+$.
The data samples used in this analysis correspond to 1 fb^{-1} of proton-proton collision data collected in 2011 at a center of mass energy $\sqrt{s} = 7$ TeV, 2 fb^{-1} collected in 2012 with $\sqrt{s} = 7$ TeV and 3.7 fb^{-1} collected in the years 2015, 2016 and 2017 with $\sqrt{s} = 13$ TeV.

6.1. Trigger strategy

Events that are further used for analysis have to pass requirements of all three trigger stages introduced in Chapter 4.3.5.
At the hardware trigger stage, information from the electromagnetic and hadronic calorimeters is used to select hadrons with large transverse momenta and energies. An event containing a B_s^0 candidate is accepted (L0 Hadron-TOS, triggered on signal) when the combined transverse energy E_T measured in electromagnetic and hadronic showers is larger than 3.5 GeV. Only selecting events which fulfill this requirement would yield a rather pure sample with little background, however, it would also reject a significant amount of events with B_s^0 signal candidates which do not have showers that deposit sufficient energy in the calorimeters. Therefore, events are also selected if any other level-0 trigger requirement is met by a trigger object in the event, which is not the B_s^0

signal candidate (L0 Global-TIS, triggered independent of signal). The way in which each event is selected at the hardware trigger stage, L0 Hadron-TOS or L0 Global-TIS, is mutually exclusive and is later used to categorize the data sample.
Events that satisfy the hardware trigger requirements are processed in the first software trigger stage HLT1, in which all tracks associated to the trigger signal candidate are reconstructed and their momenta are measured. An event is accepted if at least one track passes the requirements listed in Appendix A.1. At the second stage of the high-level-trigger, events have to either pass a dedicated set of requirements, used to explicitly reconstruct the decay $\phi \to (K^+K^-)$[1], which can occur in the decay of the most abundant D_s^- final state $D_s^- \to \phi\pi^+ \to K^+K^-\pi^+$, or have to pass a so-called topological trigger requirement[2]. The explicit requirements imposed at the second stage of the high-level-trigger are summarized in Appendix A.1.
The kinematics of B_s^0 signal candidates that pass all trigger stages show a residual dependence on whether the candidate was found in an event triggered by the level-0 hadron trigger or not. Furthermore, due to the different beam energies, the kinematic distributions also depend on whether an event was recorded during the first or second Run of the LHC. Since this analysis relies heavily on the correct description of the kinematics of the B_s^0 candidate to properly reconstruct its decay time, four disjoint data sample categories are introduced:

- Run I,L0 Hadron-TOS
- Run I,L0 Global-TIS
- Run II,L0 Hadron-TOS
- Run II,L0 Global-TIS

6.2. Pre-Selection of the $B_s^0 \to D_s^- K^+\pi^-\pi^+$ decay

The reconstruction of $B_s^0 \to D_s^- K^+\pi^-\pi^+$ decays is based on the selection of a signal D_s^- meson candidate with a significantly displaced vertex with respect to the B_s^0 decay vertex (SV), together with the selection of a oppositely charged kaon and a pion pair, which can be combined to a common vertex that is compatible with the SV. Apart from signal decays, two major background components are left in the data samples after the trigger

[1]The trigger line is called HLT2IncPhiDecision
[2]The used trigger lines are called HLT2Topo2/3/4BodyDecision

stages: Combinatorial background, where random tracks not associated with the signal decay are falsely added in the reconstruction of B_s^0 candidates and physical background, originating from decays of other b- and c-hadrons that are wrongly reconstructed as $B_s^0 \to D_s^- K^+ \pi^- \pi^+$ decays through particle mis-identification, non accurate information from the RICH detectors, or partial reconstruction. The following two sections summarize the selection requirements imposed to remove these backgrounds.

6.2.1. Criteria to reduce combinatorial background

Since the D_s^- meson is reconstructed in a three-body decay, there are in total six charged particles in the fully reconstructed B_s^0 signal decay. This gives rise to a large amount of possible combinatorial backgrounds, where at least one track is wrongly associated for either the D_s^- or the B_s^0 candidate. Therefore, a set of selection requirements is applied to both in order to reduce the amount of combinatorial background present in the analysis sample.
First, loose kinematic and topological requirements are imposed on the b-hadron:

- $\cos(\vartheta) > 0.99994$,
- flight distance (FD) $\chi^2 > 100$ to the PV,
- Vertex $\chi^2/\text{nDoF} < 8$,
- B_s^0 decay time $t_{B_s^0} > 0.4\ ps$,
- uncertainty on B_s^0 decay time $\delta t_{B_s^0} < 0.15\ ps$.

Here, $cos(\vartheta)$ is the cosine of the angle between the direction of the momentum and the flight direction of the B_s^0, the FD χ^2 is the goodness of the track reconstruction fit when assuming that the tracks of the B_s^0 daughters originate from the PV instead of the SV and the vertex χ^2 is the goodness of the B_s^0 vertex reconstruction. These requirements ensure that all selected B_s^0 candidates exhibit a significant, precisely measured decay length and are therefore spatially separated from the pp interaction point. Furthermore, they ensure that the decay vertex of the B_s^0 is measured with good accuracy and the tracks of the three B_s^0 daughters form a secondary vertex (SV).
After the data sample is pre-filtered using the requirements on the b-hadron described above, additional selection criteria are imposed on the D_s^- candidates. Of the different reconstructed final states, the $D_s^- \to K^+ K^- \pi^-$ is the most prominent one, occurring

roughly five times more frequently than the $D_s^- \to \pi^-\pi^+\pi^-$ decay and eight times more frequently than the $D_s^- \to K^-\pi^+\pi^-$ decay. For the $K^+K^-\pi^-$ final state, it is convenient to make use of its well known resonance structure [4]; the decay proceeds either via the narrow ϕ resonance, the broader K^{*0} resonance or as a non-resonant decay. Within the ϕ resonance region the sample is already sufficiently background free so that no additional criteria on the D_s^- daughters are imposed. For the K^{*0} and the non-resonant decay consecutively tighter requirements on the particle identification and the D_s^- flight-distance are applied and global requirements are imposed on the other two D_s^- final state. The following criteria are applied:

- $D_s^- \to \phi\pi^- \to K^+K^-\pi^-$
  - $m(K^+K^-) = m_\phi \pm 12\ MeV$
- $D_s^- \to K^{*0}K^- \to K^+\pi^-K^-$
  - $m(K^+K^-) \neq m_\phi \pm 12\ MeV$
  - $m(K^+\pi^-) = m_{K^{*0}} \pm 75\ MeV$
  - FD $\chi^2 > 0$
  - FD in z-direction > 0
  - $\Delta \log \mathcal{L}_{K-\pi}(K^\pm) > -5$
  - $\Delta \log \mathcal{L}_{K-\pi}(\pi^-) < 10$
- $D_s^- \to (K^+K^-\pi^-)_{NR}$
  - $m(K^+K^-) \neq m_\phi \pm 12\ MeV$
  - $m(K^+\pi^-) \neq m_{K^{*0}} \pm 75\ MeV$
  - $\Delta \log \mathcal{L}_{K-\pi}(K^\pm) > 5$
  - $\Delta \log \mathcal{L}_{K-\pi}(\pi^-) < 10$
  - FD $\chi^2 > 4$
  - FD in z-direction > 0
- $D_s^- \to \pi^+\pi^-\pi^-$
  - $\Delta \log \mathcal{L}_{K-\pi}(\pi^\pm) < 10$
  - $\Delta \log \mathcal{L}_{\pi-p}(\pi^\pm) < 20$

    * FD $\chi^2 > 9$
    * FD in z-direction > 0

- $D_s^- \to K^-\pi^+\pi^-$
    * $\Delta \log \mathcal{L}_{K-\pi}(K^-) > 8$
    * $\Delta \log \mathcal{L}_{K-\pi}(\pi^\pm) < 5$
    * $\Delta \log \mathcal{L}_{\pi-p}(\pi^\pm) < 20$
    * FD $\chi^2 > 9$
    * FD in z-direction > 0

Here, the difference of logarithmic likelihoods of particle hypothesis x and y $\Delta \log \mathcal{L}_{x-y}$ is formed using information provided by the two Cherenkov detectors RICH1 and RICH2. This criterion is used to suppress background from misidentified particles in the respective D_s^- final state. The masses of the ϕ and K^{*0} resonances m_ϕ and $m_{K^{*0}}$ are taken from the PDG [20]. Due to the smaller branching fractions of the $D_s^- \to K^-\pi^+\pi^-$ and $D_s^- \to \pi^-\pi^+\pi^-$ final states with respect to the $D_s^- \to K^-K^+\pi^-$ mode, as well as the abundance of pions over kaons in typical LHCb events, the amount of background for these two D_s^- modes is considerably larger than for the most prominent mode $D_s^- \to K^-K^+\pi^-$. Therefore, tighter selection criteria on the particle identification and the significance of the flight distance are imposed.

6.2.2. Vetoes to reduce physical background

Various physical backgrounds, which have either the same final state as the signal decay, or can contribute via a single misidentification of $K \leftrightarrow \pi$, $K \leftrightarrow p$ or $\pi \leftrightarrow p$, are still left in the data sample after imposing the requirements discussed in Section 6.2.1. Depending on the D_s^- final state, different vetoes are applied to the analysis sample in order to account for backgrounds originating from charm meson or charmed baryon decays.
In the following summary, the notation A_B is used for a particle which is identified as A, but its four-momentum $\mathbf{p}$ is computed using B as particle hypothesis, effectively changing the assigned mass from m_A to m_B in the computation of $\mathbf{p}$. For example, a particle that is identified as a kaon by the particle identification system, but which four-momentum is now computed under the pion hypothesis is expressed as K_π, with $\mathbf{p}^{K\to\pi} = (\sqrt{m_\pi^2 + \vec{p}^2}, \vec{p})$, where $\vec{p}$ is the measured three-momentum of the particle and m_π is the nominal mass of the pion, as given by the PDG [20]. The abbreviation

PID for particle identification is used throughout. The following summary gives an overview of the vetoes applied for the different D_s^- final states. First, the specific D_s^- final state is given, which is enumerated by 1-3. Under each final state, the possible physical backgrounds are mentioned, labeled by a), b) etc., together with the selection requirement that is imposed to veto the specific background.

1. Contributions to $D_s^- \to K^+K^-\pi^-$ from:

   a) $D^- \to K^-\pi^+\pi^-$:
   This contribution is possible with the misidentification of a π^+ as K^+ and is vetoed by requiring $m(K^-K_\pi^+\pi^-) \neq m(D^-) \pm 40$ MeV. A K^+ candidate from events that do not pass this veto has to fulfill more stringent PID criteria depending on the resonant D_s^- decay (see Table 6.1).

   b) $\Lambda_c^- \to K^-p\pi^-$:
   This contribution is possible with the misidentification of a p as K^+ and is vetoed by requiring $m(K^-K_p^+\pi^-) \neq m(\Lambda_c^-) \pm 40$ MeV. A K^+ candidate from events that do not pass this veto has to fulfill more stringent PID criteria depending on the resonant D_s^- decay (see Table 6.1).

   c) $D^0 \to K^+K^-$:
   A D^0 meson combined with a random π^- can mimic a $D_s^- \to K^+K^-\pi^-$ decay, this is vetoed by requiring $m(K^+K^-) < 1840$ MeV for all selected events. This ensures that the invariant mass of the K^+K^- system is lower than the threshold for the $D^0 \to K^+K^-$ decay [20].

2. Contributions to $D_s^- \to \pi^+\pi^-\pi^-$ from:

   a) $D^0 \to \pi^+\pi^-$:
   A D^0 meson combined with a random π^- can mimic a $D_s^- \to \pi^+\pi^-\pi^-$ decay, this is vetoed by requiring both possible combinations to have $m(\pi^+\pi^-) < 1700$ MeV, which ensures that the invariant mass of both $\pi^+\pi^-$ system is lower than the threshold for the $D^0 \to \pi^+\pi^-$ decay [20].

3. Contributions to $D_s^- \to K^-\pi^-\pi^+$ from:

   a) $D^- \to \pi^-\pi^-\pi^+$:
   This contribution is possible with the misidentification of a π^- as K^- and is vetoed by requiring $m(K_\pi^-\pi^-\pi^+) \neq m(D^-) \pm 40$ MeV. A K^- candidate from events that do not pass this veto has to fulfill $\Delta \log \mathcal{L}_{K-\pi}(K^-) > 15$.

b) $\Lambda_c^- \to \pi^-\pi^+\bar{p}$:
This contribution is possible with the misidentification of a $\bar{p}$ as K^- and is vetoed by requiring $m(K_{\bar{p}}^-\pi^-\pi^+) \neq m(\Lambda_c^-) \pm 40$ MeV.A K^- candidate from events that do not pass this veto has to fulfill $\Delta \log \mathcal{L}_{K-p}(K^-) > 5$.

c) $D^0 \to K^-\pi^+$:
A D^0 meson combined with a random π^- can mimic a $D_s^- \to K^-\pi^+\pi^-$ decay. This is vetoed by requiring $m(K^-\pi^+) < 1750$ MeV for all selected candidates, which ensures that the invariant mass of the $K^-\pi^+$ system is lower than the threshold for the $D^0 \to K^-\pi^+$ decay [20].

The effects of these veto requirements on the invariant D_s^- mass, reconstructed under the respective background hypothesis, are illustrated in Figures A.1,A.2 and A.3. To reduce physical background from the calibration channel $B_s^0 \to D_s^-\pi^+\pi^-\pi^+$, contributing to the signal channel $B_s^0 \to D_s^-K^+\pi^-\pi^+$, a tight PID requirement on the kaon of the $(D_s^-K^+\pi^-\pi^+)$ final state is applied. In addition, a veto for $B_s^0 \to D_s^-D_s^+$ decays is imposed, which is illustrated in Figure A.4. Furthermore, additional veto selections are applied for the three final state particle coming from the B_s^0 decay, for the signal $(X_s^+ \to K^+\pi^+\pi^-)$ and calibration $(X_d^+ \to \pi^+\pi^+\pi^-)$ channel:

1. Contributions to the signal channel $B_s^0 \to D_s^-X_s^+$, $X_s^+ \to K^+\pi^+\pi^-$:

   a) $B_s^0 \to D_s^-\pi^+\pi^-\pi^+$:
   This contribution is possible with the misidentification of a π^+ as K^+ and is suppressed with the very strict PID requirement $\Delta \log \mathcal{L}_{K-\pi}(K^+) > 10$.

   b) $B_s^0 \to D_s^-(D_s^+ \to K^-K^+\pi^+)$:
   To suppress the physical background from $B_s^0 \to D_s^-K^-K^+\pi^+$ decays, possible with the misidentification of a K^- as π^-, $\Delta \log \mathcal{L}_{K-\pi}(\pi^-) < 0$ is required. In case the invariant mass of the $(K^+\pi^+\pi^-)$ system, recomputed assuming the kaon mass hypothesis for the π^-, is close to the D_s mass, $m(K^+\pi^+\pi_K^-) = m(D_s) \pm 20$ MeV, the particle identification requirement on the π^- is further tightened to $\Delta \log \mathcal{L}_{K-\pi}(\pi^-) < -5$.

2. Contributions to the calibration channel $B_s^0 \to D_s^-X_d^+$, $X_d^+ \to \pi^+\pi^+\pi^-$:

   a) $B_s^0 \to D_s^-K^+\pi^+\pi^-$:
   This contribution is possible with the misidentification of a K^+ as π^+ and is suppressed by imposing $\Delta \log \mathcal{L}_{K-\pi}(\pi^+) < 0$ for both possible π^+ candidates.

b) $B_s^0 \to D_s^-(D_s^+ \to K^+\pi^+\pi^-)$:
This contribution is possible with the misidentification of a K^+ as π^+ and is vetoed by requiring $m(\pi^+\pi_K^+\pi^-) \neq m(D_s) \pm 20$ MeV for both π^+ candidates. Both candidates from events that do not pass this veto have to fulfill the more stringent PID requirement $\Delta \log \mathcal{L}_{K-\pi}(\pi^+) < -5$.

6.3. Multivariate selection stage

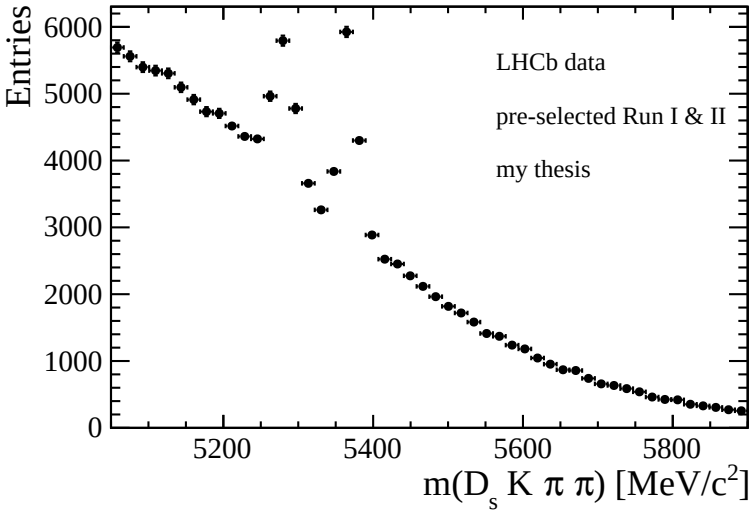

Figure 6.1.: Invariant mass distribution of $B_s^0 \to D_s^- K^+\pi^-\pi^+$ candidates, subjected to the pre-selection requirements summarized in Chapter 6.1 and 6.2. The B_d^0 and B_s^0 peaks are clearly visible, although a significant amount of background is still present in the distribution.

Figure 6.1 shows the reconstructed B_s^0 invariant mass distribution for the selected $B_s^0 \to D_s^- K^+\pi^-\pi^+$ candidates, after the requirements described above are imposed. Two peaks can be observed, one at the nominal B_d^0 and one at the B_s^0 mass, as well as a significant amount of combinatorial background and a small, peaking structure in the lower mass region. The latter component is found to be irreducible physical background from $B_s^0 \to D_s^{-*} K^+\pi^+\pi^-$ and $B_d^0 \to D^{-*} K^+\pi^+\pi^-$ decays, where the charm meson radiates a photon or a neutral pion $D_s^{-*} \to D_s^-\pi^0/\gamma$. Since the π^0/γ is not reconstructed, this decay results in the same visible final state as the signal candidates. The removal of this component from the final sample is discussed in Chapter 7.
The amount of combinatorial background from random tracks, wrongly associated with

the signal decay, can be further reduced using a multivariate selection technique (TMVA) [68]. The TMVA toolkit combines multiple variables which provide separation power between signal-like and background-like events and returns a single dimensionless response for every event. In practice, this is achieved by comparing typical signal and background events using a so-called *boosted decision tree (BDT)* [69]. A schematic view of a basic decision tree is given in Figure 6.2.

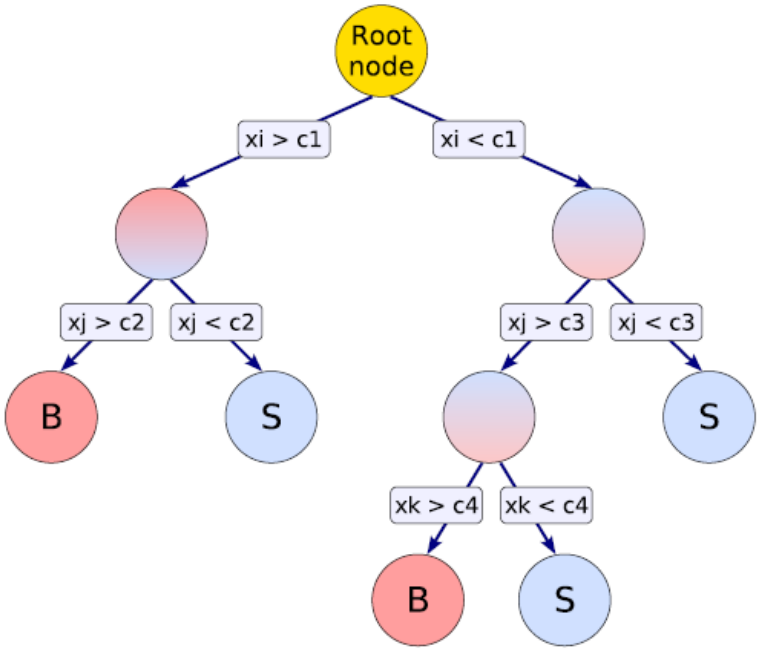

Figure 6.2.: Schematic view of a decision tree taken from [68]. Starting from the "Root Node" a sequence of binary splits is performed using the discriminating variable x_i to separate between signal-like and background-like events. Each node represents a decision similar to a cut-based selection. The final leafs are labeled signal (S) or background (B) depending on the structure of the majority of events that end up in a certain leaf.

The splitting condition at each node is obtained from two input samples, one containing pure signal and one pure background events. This process is called *training* and has the advantage, compared to a selection based on one-dimensional selection requirements, that selection criteria are applied in a higher dimensional grid of input variables. In this way, multi-dimensional correlations between the variables are taken into account. The *boosting* signalizes that the training process is repeated multiple times, giving rise to a multitude of decision trees called *decision forest.*In each iteration, sample events which are assigned to a wrong leaf, i.e. background events that end up in a signal leaf

or vice versa, are given a larger weight [70]. This procedure increases the robustness of the BDT against statistical fluctuations in the input samples. The final classification of signal-like or background-like for each event is obtained by looping over all decision trees and assigning a weight of +1 for every tree in which the event ends up in a signal leaf and -1 for each tree the event ends up in a background leaf.
Due to the kinematic similarity of the $B_s^0 \to D_s^- K^+\pi^-\pi^+$ and $B_s^0 \to D_s^-\pi^+\pi^-\pi^+$ decay, as well as the similar relative amount of B_s^0 signal candidates and combinatorial background, the shape of the distribution of combinatorial background in the invariant B_s^0 mass spectrum is very similar between the two decay channels. Since the relative branching ratio of $B_s^0 \to D_s^-\pi^+\pi^-\pi^+$ decays is one order of magnitude higher than the branching ratio for $B_s^0 \to D_s^- K^+\pi^-\pi^+$ decays, a significantly larger data sample of $B_s^0 \to D_s^-\pi^+\pi^-\pi^+$ decays is available at LHCb. Therefore, $B_s^0 \to D_s^-\pi^+\pi^-\pi^+$ decays that pass the pre-selection requirements are used as signal proxy input for the BDT training. The residual background in the sample is statistically subtracted [71] using a fit to the reconstructed mass of the B_s^0 candidates. The general procedure is explained in detail in Chapter 7. Figure 6.3 shows the invariant mass distribution with the fit overlaid.

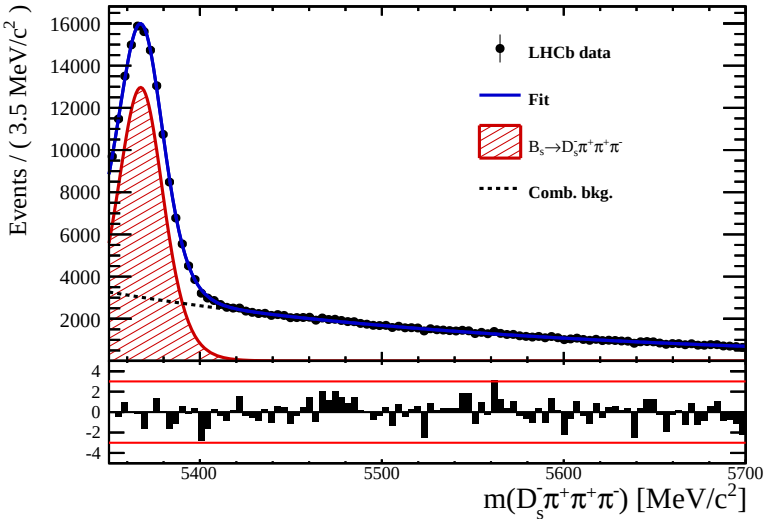

Figure 6.3.: Reconstructed B_s mass for $B_s \to D_s\pi\pi\pi$ candidates that pass the preselection. The fitted curve is shown in blue, the Gaussian-like signal component in red (filled area) and the exponential background component in black (dotted line).

As background input for the training, events with $B_s^0 \to D_s^-\pi^+\pi^-\pi^+$ or $B_s^0 \to D_s^- K^+\pi^-\pi^+$ candidates with a reconstructed mass above $m_{B_s^0} > 5500$ MeV are used

as proxy. This mass region is sufficiently far away from the nominal B_s^0 mass of 5366 MeV [20] and fully dominated by combinatorial background, as can be seen in Figure 6.3. The following discriminating variables, which are related to the decay kinematics, as well as the reconstruction and separation of the secondary decay vertices, are used for the BDTG training:

- The logarithm of the B_s impact-parameter χ^2, B_s $\log(\chi^2_{IP})$.
- The logarithm of the cosine of the B_s direction angle, $\log(\cos(\vartheta))$.
- Fit quality of the decay tree fit (DTF) with PV constrain, χ^2_{DTF}/n.d.f., where n.d.f. abbreviates the number of degrees of freedom.
- The logarithm of the difference in vertex fit quality when adding one extra particle track to the reconstruction algorithm, $\log(\Delta\chi^2_{add-track})$.
- The difference between the transverse momentum of the B_s^0 candidate and the transverse momentum of all particles reconstructed within a cone of radius $r = \sqrt{(\Delta\Phi)^2 + (\Delta\eta)^2} < 1$ rad around the B_s^0 candidate, $A_{p_T}^{cone}$. Here, Φ and η are the azimuthal and polar angle of the LHCb detector coordinate system, respectively.
- Logarithm of the the smallest X_s daughter impact-parameter χ^2 to the PV, $\log(min^{X_s}(\chi^2_{IP}))$.
- Maximum distance of closest approach of the X_s daughters, max(DOCA).
- Cosine of the largest opening angle between the D_s^- and any bachelor track h_i in the plane transverse to the beam, $\cos(\max\theta_{D_s^- h_i})$.
- Logarithm of the the smallest D_s^- daughter impact-parameter χ^2 to the PV, $\log(min^{D_s^-}(\chi^2_{IP}))$.
- Logarithm of the D_s^- flight-distance significance, D_s^- $\log(\chi^2_{FD})$.
- Logarithm of the D_s^- radial flight-distance, D_s^- $\log(RFD)$.

Separate boosted decision trees are trained for the four sample categories (Run I,II and L0 Hadron-TOS,Global-TIS) defined in Chapter 6.1 to account for differences in the distributions of the kinematic variables due to the different center of mass energies and trigger schemes. Training the classifier on a sub-sample which is supposed to be used in the analysis might cause a bias, as the classifier selects, in case of large statistical fluctuations of one or more variables in the sample, the training events more efficiently. As

this so-called overtraining can not be completely avoided, the signal and the background training samples are split into two disjoint sub-samples according to whether the event number is even or odd. Then, the classifier is trained on the even sample and applied to the odd one, and vice-versa (cross-training).
The distributions of all signal and background input variables are shown in Appendix A.3 and the resulting classifier response for $B_s^0 \to D_s^- \pi^+ \pi^- \pi^+$ data is shown in Figure 6.4 for each category (even and odd test samples combined).

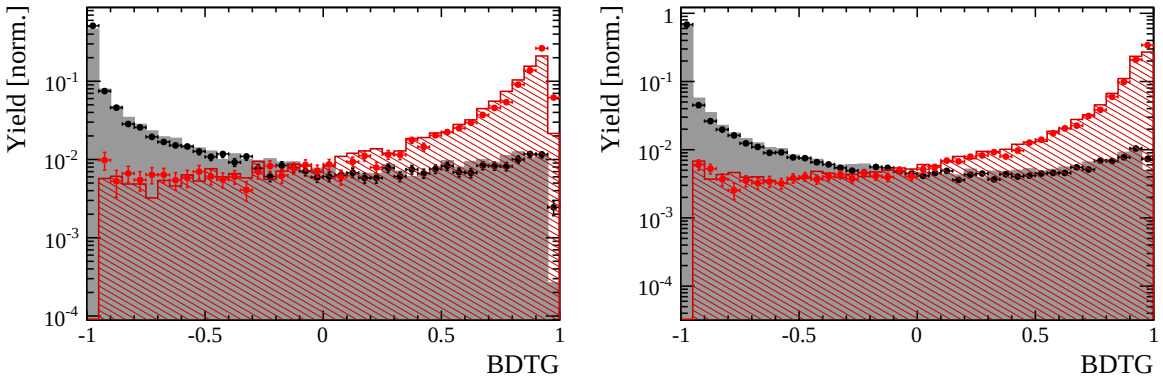

Figure 6.4.: Signal (red) and background (black) distributions for the classifier response for Run I (left) and Run II (right) data. Filled histograms (data points) show the BDT response for the L0-TOS (L0-TIS) category. Even and odd test samples are combined.

After the similarity of all distributions of crucial observables for both decay channels, $B_s^0 \to D_s^- \pi^+ \pi^- \pi^+$ and $B_s^0 \to D_s^- K^+ \pi^- \pi^+$, is checked extensively [5], the trained classifier is applied to remove combinatorial background from the $B_s^0 \to D_s^- K^+ \pi^- \pi^+$ sample. For this purpose, it is crucial to determine the optimal selection requirement on the classifier response for each of the four disjoint data categories. In the presented analysis, the signal significance is used as a figure of merit (FOM):

$$\mathrm{FOM(BDTG)} = \frac{N_s(\mathrm{BDTG})}{\sqrt{N_s(\mathrm{BDTG}) + N_b(\mathrm{BDTG})}}, \tag{6.1}$$

where N_s(BDTG) is the $B_s^0 \to D_s^- K^+ \pi^- \pi^+$ signal yield for a given selection criteria on the classifier output response and N_b(BDTG) is the yield of combinatorial background in the signal region, defined as $m_{B_s^0,\mathrm{PDG}} \pm 40 MeV$.

To determine the $B_s^0 \to D_s^- K^+ \pi^- \pi^+$ yields as function of the BDT response, $N_{s,b}$(BDTG), the BDT selection efficiencies $\epsilon_{s,b}$, evaluated on the corresponding test samples of $B_s^0 \to D_s^- \pi^+ \pi^- \pi^+$ decays are used. Careful cross-checks are performed to justify the portability

of the BDT selection efficiencies from the $B_s^0 \to D_s^- \pi^+ \pi^- \pi^+$ to the $B_s^0 \to D_s^- K^+ \pi^- \pi^+$ decay channel [5].

In order to fix the overall scale, it is required to know the yields at (at least) one point of the scanned range $[-1; 1]$ of the classifier response. This fix point is chosen to be at BDT response > 0, for which a fit to the reconstructed B_s^0 mass is performed using a fit model described in Chapter 7, to obtain the corresponding yields $N_{s,b}(0)$ of $B_s^0 \to D_s^- K^+ \pi^- \pi^+$ candidates. These yields are then scaled with the efficiency ratio $\epsilon_{s,b}(\text{BDTG})/\epsilon_{s,b}(0)$, provided by the TMVA software for a given criteria on the classifier output response, to calculate the yields for this response:

$$N_{s,b}(\text{BDTG}) = N_{s,b}(0) \cdot \frac{\epsilon_{s,b}(\text{BDTG})}{\epsilon_{s,b}(0)}. \tag{6.2}$$

Figure 6.5 shows the resulting scans of the normalized FOM, over the selection criteria on the output response, $BDTG > [-1; 1]$, for each training category.

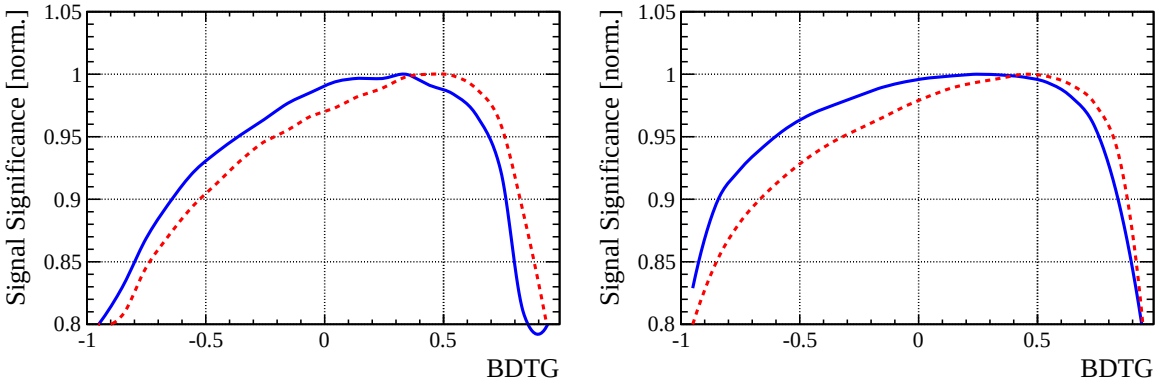

Figure 6.5.: Signal significance as a function of the applied requirement on the BDT classifier response for Run I (left) and Run II (right) $B_s^0 \to D_s^- K^+ \pi^- \pi^+$ data. The scans for the L0-TOS (L0-TIS) category are shown in blue (red). The signal significance is normalized to be 1 at the optimal BDTG cut value.

The respective maxima of the distributions shown in Figure 6.5 are the optimal working points found for the chosen BDT classifier.

6.4. Summary of the selection procedure

Tables 6.1 and 6.2 summarize all selection requirements imposed on the $B_s^0 \to D_s^- K^+ \pi^- \pi^+$ and $B_s^0 \to D_s^- \pi^+ \pi^- \pi^+$ candidates used in this analysis, including the criteria used on the neural network response for the four disjoint data categories. Every selection stage is

described in detail in the previous Chapters 6.1, 6.2 and 6.3. For simplicity, the particle identification requirements $\Delta \log \mathcal{L}_{K-\pi}$ and $\Delta \log \mathcal{L}_{p-\pi}$ are abbreviated with PIDK and PIDp, respectively.

Table 6.1.: Selection requirements for $D_s \to 3h$ candidates.

	Description	Requirement
$D_s \to hhh$	$m(hhh)$	$= m_{D_s} \pm 25$ MeV
$D_s^- \to KK\pi^-$	D^0 veto	$m(KK) < 1840$ MeV
$D_s^- \to \phi\pi^-$	$m(KK)$	$= m_\phi \pm 12$ MeV
	PIDK(K^+)	> -10
	PIDK(K^-)	> -10
	PIDK(π^-)	< 20
	χ^2_{FD}	> 0
	FD in z	> -1
	D^- veto	$m(K^+K^-_\pi\pi^-) \neq m(D^-) \pm 40$ MeV || PIDK(K^-) > 5
	Λ_c veto	$m(K^+K^-_p\pi^-) \neq m(\Lambda_c) \pm 40$ MeV || PIDK(K^-) $-$ PIDp(K^-) > 2
$D_s^- \to K^*(892)K^-$	$m(KK)$	$\neq m_\phi \pm 12$ MeV
	$m(K^+\pi^-)$	$= m_{K^*(892)} \pm 75$ MeV
	PIDK(K^+)	> -10
	PIDK(K^-)	> -5
	PIDK(π^-)	< 10
	χ^2_{FD}	> 0
	FD in z	> 0
	D^- veto	$m(K^+K^-_\pi\pi^-) \neq m(D^-) \pm 40$ MeV || PIDK(K^-) > 15
	Λ_c veto	$m(K^+K^-_p\pi^-) \neq m(\Lambda_c) \pm 40$ MeV || PIDK(K^-) $-$ PIDp(K^-) > 5
$D_s^- \to (KK\pi^-)_{NR}$	$m(KK)$	$\neq m_\phi \pm 12$ MeV
	$m(K^+\pi^-)$	$\neq m_{K^*(892)} \pm 75$ MeV
	PIDK(K^+)	> 5
	PIDK(K^-)	> 5
	PIDK(π^-)	< 10
	χ^2_{FD}	> 4
	FD in z	> 0
	D^- veto	$m(K^+K^-_\pi\pi^-) \neq m(D^-) \pm 40$ MeV || PIDK(K^-) > 15
	Λ_c veto	$m(K^+K^-_p\pi^-) \neq m(\Lambda_c) \pm 40$ MeV || PIDK(K^-) $-$ PIDp(K^-) > 5
$D_s \to \pi\pi\pi$	PIDK(π)	< 10
	PIDp(π)	< 20
	D^0 veto	$m(\pi^+\pi^-) < 1700$ MeV
	χ^2_{FD}	> 9
	FD in z	> 0
$D_s^- \to K^-\pi^+\pi^-$	PIDK(K)	> 8
	PIDK(π)	< 5
	PIDp(π)	< 20
	D^0 veto	$m(K^-\pi^+) < 1750$ MeV
	χ^2_{FD}	> 9
	FD in z	> 0
	D^- veto	$m(K^-_\pi\pi^+\pi^-) \neq m(D^-) \pm 40$ MeV || PIDK(K^-) > 15
	Λ_c veto	$m(K^-_p\pi^+\pi^-) \neq m(\Lambda_c) \pm 40$ MeV || PIDK(K^-) $-$ PIDp(K^-) > 5

Table 6.2.: Selection requirements for $B_s \to D_s K\pi\pi(D_s\pi\pi\pi)$ candidates.

	Description	Requirement
$B_s \to D_s h\pi\pi$	$m(D_s h\pi\pi)$	> 5200 MeV
	χ^2_{vtx}/ndof	< 8
	$\cos\vartheta$	> 0.99994
	χ^2_{FD}	> 100
	χ^2_{IP}	< 16
	χ^2_{DTF}/ndof	< 15
	$\Delta\chi^2_{add-track}$	> 2
	$\cos(\max\theta_{D_s^- h_i})$	> -0.9
	t	$> 0.4\ ps$
	δt	$< 0.15\ ps$
	Phasespace region	$m(h\pi\pi) < 1.95$ GeV
		$m(h\pi) < 1.2$ GeV
		$m(\pi\pi) < 1.2$ GeV
	Wrong PV veto	nPV $= 1$ || $\min(\Delta\chi^2_{IP}) > 20$
	BDTG	> 0.35 [Run I,L0-TOS]
		> 0.45 [Run I,L0-TIS]
		> 0.25 [Run II,L0-TOS]
		> 0.45 [Run II,L0-TIS]
$X_s^+ \to K^+\pi^+\pi^-$	PIDK(K)	> 10
	PIDK(π^+)	< 10
	PIDK(π^-)	< 0
	D_s veto	$m(K^+\pi^+\pi^-_K) \neq m(D_s) \pm 20$ MeV || PIDK(π^-) < -5
$X_s^+ \to \pi^+\pi^+\pi^-$	PIDK(π^+)	< 0
	PIDK(π^-)	< 10
	D_s veto	$m(\pi^+\pi^+_K\pi^-) \neq m(D_s) \pm 20$ MeV || PIDK(π^+) < -5
All tracks	hasRich	$= 1$

Chapter 7

Description of the invariant mass distributions of B_s^0 signal candidates

In this Chapter, the determination of the yields of the signal and background contributions, present in the selected data samples of $B_s^0 \to D_s^- K^+\pi^-\pi^+$ and $B_s^0 \to D_s^-\pi^+\pi^-\pi^+$ candidates after all selection stages discussed in Chapter 6 are applied, is discussed. The mathematical models, used to describe the invariant mass distributions of both decays, are further used in various steps of the presented analysis to statistically subtract the background [71] from other distributions of interest, such as the decay time distribution of B_s^0 candidates, $t_{B_s^0}$.
Unbinned maximum likelihood fits [67] to the reconstructed mass of the selected B_s^0 candidates are performed for the calibration and signal channel, separately. The invariant mass, $m_{B_s^0} \equiv m(D_s^- h^+\pi^+\pi^-)$, is determined using an algorithm that fits the decay chain of the $B_s^0 \to D_s^- h^+\pi^-\pi^+$ decay, starting with the six particle final state and consecutively fitting the vertices of the mother particles. This algorithm is called decay tree fit [72] and, for the presented analysis, it constrains the mass of the D_s^- to match the world average [20] and the position of the proton-proton interaction point in the respective event. The probability density functions (PDFs) used to describe the signal and background components are described in the following.

7.1. Signal model

The mass distribution of signal B_s^0 candidates for both modes, $B_s^0 \to D_s^- K^+\pi^-\pi^+$ and $B_s^0 \to D_s^-\pi^+\pi^-\pi^+$, is modeled using a Johnson's SU function [73], which results from a variable transformation of a normal distribution to allow for asymmetric tails:

$$\mathcal{J}(x|\mu,\sigma,\nu,\tau) = \frac{e^{-\frac{1}{2}r^2}}{2\pi \cdot c \cdot \sigma \cdot \tau \cdot \sqrt{z^2+1}}, \text{ with} \tag{7.1}$$

$$r = -\nu + \frac{\text{asinh}(z)}{\tau} \tag{7.2}$$

$$z = \frac{x - (\mu - c \cdot \sigma \cdot e^{\tau}\text{sinh}(\nu \cdot \tau))}{c \cdot \tau} \tag{7.3}$$

$$c = \frac{e^{\tau^2} - 1}{2\sqrt{e^{\tau^2} \cdot \cosh(2\nu \cdot \tau) + 1}}. \tag{7.4}$$

It is expressed in terms of the central moments up to order four: The mean of the distribution μ, the standard deviation σ, the skewness ν and the kurtosis τ. The Johnson's SU model allows for an adequate description of the signal distribution which, in general, is Gaussian distributed with a width that represents a mixture of the natural decay width of the B_s^0 meson and the mass resolution of the detector. The small skewness and kurtosis of the tails of the distribution originates from minor distortions due to the reconstruction process and the selection requirements imposed on the final state particles. These two parameters are determined from a fit to simulated $B_s^0 \to D_s^- K^+\pi^-\pi^+$ and $B_s^0 \to D_s^-\pi^+\pi^-\pi^+$ signal candidates, shown in Figure 7.1, that have to pass the same selection stages as data candidates.

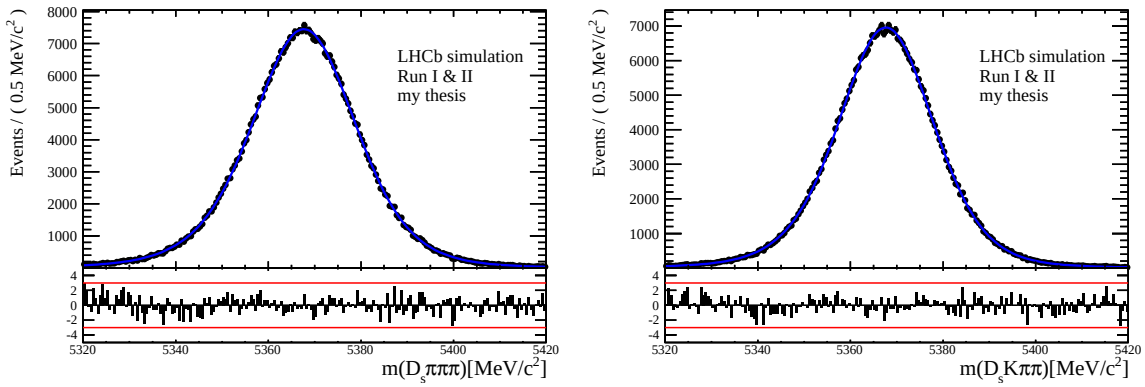

Figure 7.1.: Invariant mass distributions of simulated (left) $B_s^0 \to D_s^-\pi^+\pi^-\pi^+$ and (right) $B_s^0 \to D_s^- K^+\pi^-\pi^+$ events. A fit with a Johnson's SU PDF is overlaid. The pull distributions in the bottom of the figures show the deviation between the fit model and data.

7.2. Background models

After the full selection, the following residual background components are still present in the final samples and have to be accounted for:

Combinatorial background
The combinatorial background is shaped without any peaking structures in $m(D_s^- h^+\pi^+\pi^-)$, due to the combination of particle tracks that do not originate from the mother particle and therefore do not peak in the invariant mass distribution. This component is described by a second order polynomial $\mathcal{P}(\mathcal{O}(m^2))$.

Physical background from $B_d^0 \to D_s^- K^+\pi^+\pi^-$ decays
The signal-like shape originating from decays of B_d^0 mesons into the $D_s^- h^+\pi^+\pi^-$ final state, present in both invariant mass distributions ($h = K/\pi$), is described by the B_s^0 signal model where the mean μ is shifted by the known mass difference $m_{B_s} - m_{B_d}$ of both mesons [20].

Partially reconstructed background
Partially reconstructed $B_s^0 \to D_s^{-*}\pi^+\pi^+\pi^-$ decays, where the excited D_s^{-*} meson decays into a photon $D_s^{-*} \to D_s^-\gamma$ or a neutral pion $D_s^{-*} \to D_s^-\pi^0$, are expected to be peaking at lower values compared to the signal decays in the $m(D_s^-\pi^+\pi^-\pi^+)$ mass spectrum due to the missing momentum, carried away by the undetected π^0 or γ. Furthermore, this contribution has large tails to its peaking structure, because the unreconstructed momentum p_{γ/π^0} is continuously distributed. An empirical description for the shape of this background in $m(D_s^-\pi^+\pi^-\pi^+)$ is derived from a simulated $B_s^0 \to D_s^{-*}\pi^+\pi^+\pi^-$ sample subject to the full $B_s^0 \to D_s^-\pi^+\pi^+\pi^-$ selection. Figure 7.2 (left) shows the respective reconstructed $m(D_s^-\pi^+\pi^-\pi^+)$ distribution. A sum of three Gaussian functions with asymmetric widths, $\sum_{i=1}^{3}(\mathcal{AG}_i)$, is found to describe the shape of the $m(D_s^{-*}\pi^+\pi^-\pi^+)$ distribution and is therefore used to model it. Since the choice of this model is not unique, different alternative models are considered, as further discussed in Chapter 10.3.2. In the fit of the chosen model to data, all parameters are constrained to the ones obtained from this fit to the simulated sample.
The equivalent $B_s^0 \to D_s^- K^+\pi^-\pi^+$ component contributing to the $B_s^0 \to D_s^{-*}K^+\pi^+\pi^-$ data sample is described by the same model. Contributions from $B_d^0 \to D_s^{-*}K^+\pi^+\pi^-$ decays are described with the $B_s^0 \to D_s^{-*}K^+\pi^+\pi^-$ model, shifted by $m_{B_s^0} - m_{B_d^0}$. The

respective B_d^0 decay into $D_s^-\pi^+\pi^-\pi^+$ (calibration sample) is found to be negligible.

Misidentified background in $B_s^0 \to D_s^- K^+\pi^-\pi^+$

A small fraction of $B_s^0 \to D_s^-\pi^+\pi^-\pi^+$ and $B_s^0 \to D_s^{-*}\pi^+\pi^+\pi^-$ decays, where one of the positively charged pions is misidentified as a kaon, contaminate the $B_s^0 \to D_s^- K^+\pi^-\pi^+$ sample. The contamination is enhanced due to the fact that the branching fraction of the $B_s^0 \to D_s^-\pi^+\pi^-\pi^+$ decay is approximately one order of magnitude larger than the branching fraction of $B_s^0 \to D_s^- K^+\pi^-\pi^+$ decays. To determine the corresponding shapes of the $m(D_s^- K^+\pi^+\pi^-)$ distribution, simulated samples of these fully and partially reconstructed backgrounds, passing the full selection, except for the requirement on the particle identification of the bachelor π^+, are used. It is well known and studied in LHCb that the PID information is not accurately described in the simulation. Therefore, a dedicated LHCb software package, called PIDCalib [74], is used to determine the transverse momentum p_T and pseudorapidity η dependent $\pi^+ \to K^+$ misidentification probability for each pion. Consequently, the particle hypothesis for the pion with the higher misidentification probability is changed to the kaon hypothesis. The corresponding four-momentum of the particle, defined in Equation 4.5 is changed by replacing $m_\pi \to m_K$. Finally, the invariant B_s^0 mass, $m(D_s^-\pi_K^+\pi^+\pi^-)$ is recomputed to evaluate the shape of the misidentified background.

The resulting distributions are shown in Figure 7.2 (middle,right) and empirically modeled by the sum of two Crystal Ball functions $\sum_{i=1}^{2}(F_{CB,i})$. The Crystal Ball function is given by a Gaussian core with an exponential tail on one side [75],

$$F_{CB}(m;\mu,n,\alpha,\sigma) = N \cdot \begin{cases} exp\left(-\frac{(m-\mu)^2}{2\sigma^2}\right) & \text{for } \frac{m-\mu}{\sigma} < \alpha \\ A \cdot \left(B - \frac{m-\mu}{\sigma}\right)^{-n} & \text{for } \frac{m-\mu}{\sigma} \geq \alpha \end{cases}, \tag{7.5}$$

where μ and σ are the mean and width of the Gaussian function, n parametrizes the slope of the exponential tail and α determines the cut-off value from which the tail starts. A and B are coefficients determined by n and α.

The expected yield of misidentified $B_s^0 \to D_s^-\pi^+\pi^-\pi^+$ ($B_s^0 \to D_s^{-*}\pi^+\pi^+\pi^-$) candidates in the $B_s^0 \to D_s^- K^+\pi^-\pi^+$ sample is computed by multiplying the misidentification probability of 0.61%, which gives the combined chance that one of the two π^+ candidates is wrongly identified as a K^+ and is derived from the LHCb software package [74], by the number of $B_s^0 \to D_s^-\pi^+\pi^-\pi^+$ ($B_s^0 \to D_s^{-*}\pi^+\pi^+\pi^-$) candidates as determined in the fit to the $B_s^0 \to D_s^-\pi^+\pi^-\pi^+$ data sample. In the fit to the invariant mass of $B_s^0 \to D_s^- K^+\pi^-\pi^+$ candidates, the misidentified background yields are fixed to the predicted ones.

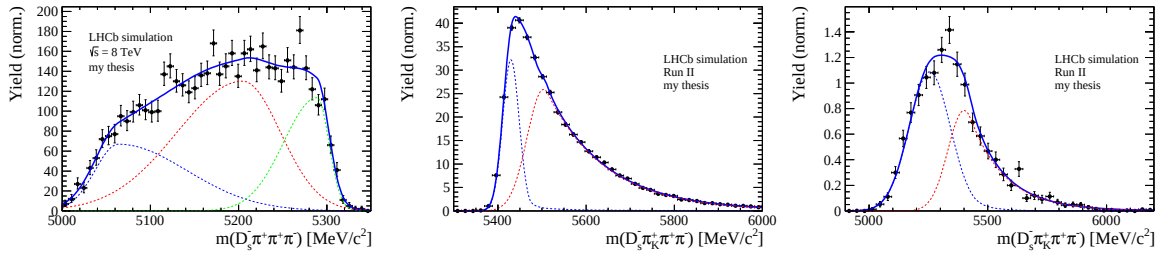

Figure 7.2.: Left: Invariant mass distribution of simulated $B_s^0 \to D_s^{-*}\pi^+\pi^+\pi^-$ events, where the γ/π^0 is excluded from the reconstruction. The distribution is described by the sum of three Gaussian functions with asymmetric tails, overlaid in (doted lines) blue, red and green. The combined model is shown in (solid line) blue.
Middle: Invariant mass distribution of simulated $B_s^0 \to D_s^-\pi^+\pi^+\pi^-$ events, where one of the pions is reconstructed as a kaon taking the misidentification probability into account.
Right: Invariant mass distribution for simulated $B_s^0 \to D_s^{-*}\pi^+\pi^+\pi^-$ events, where the γ/π^0 from the D_s^{+*} is excluded from reconstruction and one of the pions is reconstructed as a kaon taking the misidentification probability into account. The middle and right distributions are described by the sum of two Crystal Ball functions, with their components overlaid in (doted lines) red and blue. The combined models are shown in (solid line) blue.

7.3. Fit of the invariant B_s^0 mass

The models for the description of the signal and background components, discussed in the previous two Sections 7.1 and 7.2, are combined to form the final fit model for the $m(D_s^-\pi^+\pi^-\pi^+)$ and $m(D_s^-K^+\pi^-\pi^+)$ distributions. For $m(D_s^-\pi^+\pi^-\pi^+)$ the combined model is

$$\mathcal{PDF}(m(D_s^-\pi^+\pi^-\pi^+)|\vec{\lambda}) = N_{Sig}\cdot\mathcal{J}(m_{B_s^0}|\vec{\lambda}) + N_{part.Reco.}\cdot\sum_{i=1}^{3}(\mathcal{AG}_i(m_{B_s^0}|\vec{\lambda})) + N_{Comb.Bkg.}\cdot\mathcal{P}(\mathcal{O}(m^2))(m_{B_s^0}|\vec{\lambda}),$$

where N_x is the yield of the component x, $m_{B_s^0}$ is the invariant mass of the B_s^0 candidates, $\vec{\lambda}$ is the vector of fit parameters, $\mathcal{J}$ is the Johnson SU function, $\mathcal{AG}$ is an asymmetric Gaussian function and $\mathcal{P}(\mathcal{O}(m^2))$ is a second order polynomial. For the $m(D_s^-K^+\pi^-\pi^+)$ distribution, the misidentified background, modeled by the Crystal Ball functions F_{CB}, needs to be taken into account as additional contribution:

$$\mathcal{PDF}(m(D_s^- K^+\pi^-\pi^+)|\vec{\lambda}) = N_{Sig}\cdot\mathcal{J}(m_{B_s^0}|\vec{\lambda}) + N_{part.Reco.}\cdot\sum_{i=1}^{3}(\mathcal{AG}_i(m_{B_s^0}|\vec{\lambda}))$$
$$+ N_{Comb.Bkg.}\cdot\mathcal{P}(\mathcal{O}(m^2))(m_{B_s^0}|\vec{\lambda}) + N_{mis-ID}\cdot\sum_{i=1}^{2}(F_{CB,i}(m_{B_s^0}|\vec{\lambda})).$$

In general, a probability density function is normalized to one ($\int\mathcal{PDF}(m)dm = 1$), whereas the fit used to describe the mass distributions in this analysis is performed as extended maximum likelihood fit, extending the normalization of the $\mathcal{PDF}$ to be the sum of all entries in the fit sample, $\int\mathcal{PDF}(m)dm = N_{total}$. Using this extension, the yields of the different components can be extracted as fit parameters N_x.
Figure 7.3 shows the invariant mass distribution for $B_s^0 \to D_s^-\pi^+\pi^-\pi^+$ and $B_s^0 \to D_s^- K^+\pi^-\pi^+$ candidates passing all selection criteria. The combined model, fitted to the data sample, is overlaid. The obtained signal and background yields are listed in Tables 7.1 and 7.2.

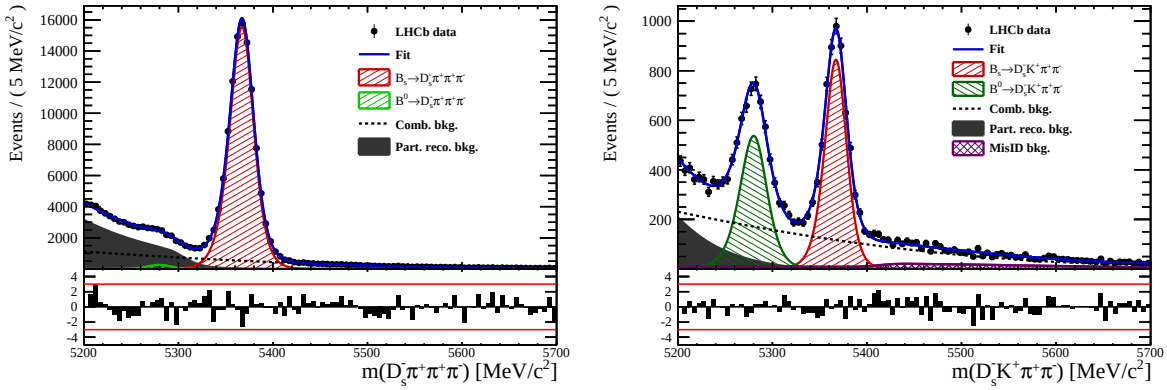

Figure 7.3.: Invariant mass distribution of $B_s^0 \to D_s^-\pi^+\pi^-\pi^+$ (left) and $B_s^0 \to D_s^- K^+\pi^-\pi^+$ (right) candidates. The fit, performed using the combined model discussed in the text, is overlaid in blue.

Table 7.1.: Total signal and background yields found in the $B_s^0 \to D_s^- \pi^+ \pi^- \pi^+$ sample (left) and signal yield for the different D_s^- final states contributing to the $B_s^0 \to D_s^- \pi^+ \pi^- \pi^+$ decay in the presented analysis (right).

Component	Yield
$B_s \to D_s \pi\pi\pi$	104176 ± 356
$B^0 \to D_s \pi\pi\pi$	1742 ± 363
Partially reco. bkg.	43157 ± 407
Combinatorial bkg.	40992 ± 455

D_s final state	Signal yield
$D_s^- \to \phi^0(1020)\pi^-$	35429 ± 202
$D_s^- \to K^{*0}(892)K^-$	29388 ± 194
$D_s^- \to (K^- h^+ \pi^-)$	21695 ± 164
$D_s^- \to \pi^+\pi^-\pi^-$	17665 ± 148

Table 7.2.: Total signal and background yields found in the $B_s^0 \to D_s^- K^+ \pi^- \pi^+$ sample (left) and signal yield for the different D_s^- final states contributing to the $B_s^0 \to D_s^- K^+ \pi^- \pi^+$ decay in the presented analysis (right).

Component	Yield
$B_s \to D_s K\pi\pi$	5172 ± 88
$B^0 \to D_s K\pi\pi$	4109 ± 100
Partially reco. bkg.	1825 ± 204
Misidentified bkg.	1186 ± 0
Combinatorial bkg.	9172 ± 221

D_s final state	Signal yield
$D_s^- \to \phi^0(1020)\pi^-$	1637 ± 47
$D_s^- \to K^{*0}(892)K^-$	1537 ± 47
$D_s^- \to (K^- h^+ \pi^-)$	1134 ± 41
$D_s^- \to \pi^+\pi^-\pi^-$	864 ± 41

Chapter 8

Determination of the decay-time acceptance and resolution correction

The correct description of the decay-time distribution of the B_s^0 mesons in the decay $B_s^0 \to D_s^- K^+ \pi^- \pi^+$ is the central objective of the presented analysis. There are two major effects, which lead to a distortion of the observed distribution with respect to the theoretically expected, time-dependent decay rate given in Equation 3.56.
On one hand, the decay-time distribution of B_s^0 candidates is sculpted due to the geometry of the LHCb detector and the applied selection requirements, which are described in Chapter 6. In particular, the requirement on the flight distance of the B_s^0, the impact parameter with respect to the proton-proton interaction point and the direction angle $\cos(\vartheta)$, as well as the direct selection requirement on the decay-time, $t_{B_s^0} > 0.4\ ps$, leads to a time-dependent selection efficiency $\epsilon(t_{B_s^0})$. On the other hand, the finite decay-time resolution of the detector, which generally depends on the number of final-state particles and their kinematics, dilutes the sensitivity to the $B_s^0 - \bar{B}_s^0$ oscillation and the CP parameters C, D_f and S_f. This effective damping of the observables has to be accounted for in the time-dependent fit by introducing a decay-time uncertainty $\sigma(t_{B_s^0})$ and including it in the fit model.
The studies to determine $\sigma(t_{B_s^0})$ and $\epsilon(t_{B_s^0})$ are summarized in the next two sections.

8.1. Decay-time resolution

Considering that the measured oscillation frequency of the B_s^0 [20] and the average LHCb detector resolution [54] are both $\mathcal{O}(50 fs^{-1})$, it is crucial to correctly describe the decay time resolution in order to avoid a bias on the measurement of time-dependent CP violation. Since the resolution depends on the particular event, especially the decay time

$t_{B_s^0}$ itself, the sensitivity on the CP observables, and therefore also on the CKM angle γ, can be significantly improved by using an event-dependent resolution model rather than an average resolution. For this purpose, the per-event decay time error $\sigma_i(t_{B_s^0})$, which is estimated based on the uncertainty obtained from the global kinematic fit of the momenta and vertex positions (DTF) [76] with constraints on the primary vertex position and the D_s^- mass, is used. To utilize this event-dependent uncertainty, the per-event decay-time error has to be properly calibrated [4]. Concretely, a scaling function that scales a given, uncalibrated error to the effective decay-time resolution $\sigma_{i,eff}(t_{B_s^0})$ of the given event has to be found:

$$\mathcal{F}(\sigma_i(t_{B_s^0})) = \sigma_{i,eff}(t_{B_s^0}). \tag{8.1}$$

The uncalibrated decay time error distribution for $B_s^0 \to D_s^-\pi^+\pi^-\pi^+$ signal candidates are shown in Figure 8.1 for data taken during Run I and Run II. Significant deviations between the distributions from those two different data taking periods are observed due to the increase in center-of-mass energy from Run I to Run II, as well as changing procedures in the pattern and vertex reconstruction between the runs. Consequently, the decay time error calibration is performed separately for both data taking periods.

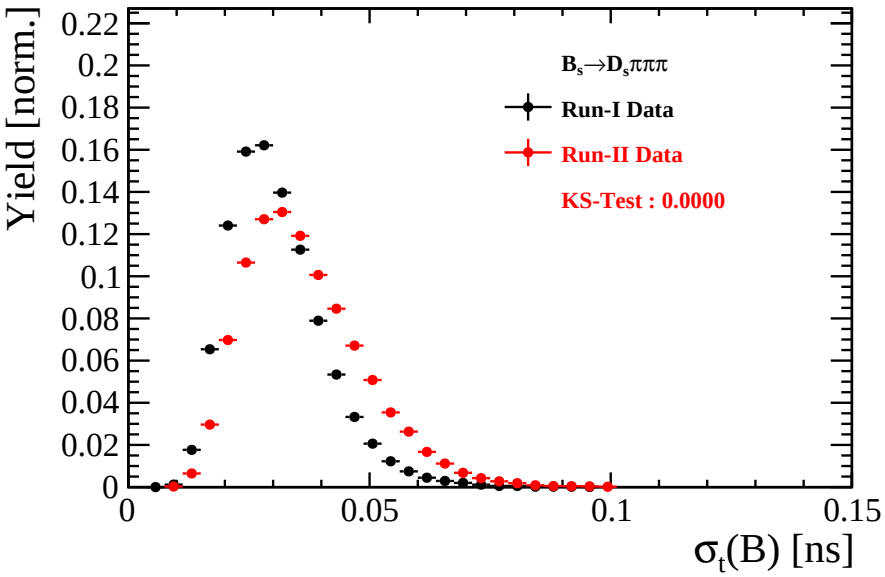

Figure 8.1.: Distribution of the decay time error for $B_s^0 \to D_s^-\pi^+\pi^-\pi^+$ signal candidates for Run I (black) and Run II (red) data.

Different approaches have to be used to obtain the correct scaling function $\mathcal{F}(\sigma_i(t_{B_s^0}))$ for the two different run periods.

Due to the fact that no dedicated samples that allow the calibration of the decay-time errors for $B_s^0 \to D_s^- K^+\pi^-\pi^+$ decays are available for Run I, the calibration has to be taken as an input from another time-dependent analysis [4] and can only be validated using simulated $B_s^0 \to D_s^- K^+\pi^-\pi^+$ decays. This procedure is described in detail in the following Section.
For $B_s^0 \to D_s^- K^+\pi^-\pi^+$ data recorded during Run II, an additional data sample, containing the same final state particles as the analyzed signal decay, but reconstructing D_s^- mesons that originate from the proton-proton interaction, is available. The reconstruction of D_s^- candidates originating from the PV ensures that almost no physical B_s^0 candidates are present in the sample[1] and that the true decay-time of the so-called fake B_s^0 meson is $t_{true}(fake\ B_s^0) \equiv 0$. Without time-resolution effects, the expected decay-time distribution of the fake B_s^0 candidates should follow a delta function, with a sharp peak at $t(fake\ B_s^0) = 0$. The decay-time resolution effect is broadening this distribution to a Gaussian shape with significant width, centered around zero. Therefore, analyzing the decay-time of non-physical B_s^0 candidates, reconstructed in this particular way, provides information about the effective decay-time resolution.

8.1.1. Calibration for data taken in Run I

For Run I data, a calibration using the closely related analysis of $B_s^0 \to D_s^- K^+$ decays at LHCb [4], is used. This calibration is done using a sample containing D_s^- mesons originating from the primary vertex, as discussed in the previous section. The portability of this calibration to the presented decay channel is verified in the following, using a simulated sample of signal $B_s^0 \to D_s^- K^+\pi^-\pi^+$ decays.
For simulated $B_s^0 \to D_s^- K^+\pi^-\pi^+$ events, the distribution of the differences between the reconstructed decay time and the decay time used for the generation of the particular candidate (true decay time),

$$\Delta t(B_s^0) = t_{reco}(B_s^0) - t(B_s^0)_{true}, \tag{8.2}$$

is a direct measure of the decay time resolution. To determine the spread of this distribution, the sum of two Gaussian functions with a common mean but independent widths is used, as shown on the left side of Figure 8.2. The effective damping of the mixing and the time-dependent CP amplitudes due to the finite time resolution is described by the dilution $\mathcal{D}$, which can take values between 1 and 0. In the case of an infinitely precise

[1] A small fraction of real B_s^0 candidates with decay times very close to zero are still left in this sample

decay-time measurement, there would be no damping and therefore $\mathcal{D} = 1$ would hold, while for a resolution that is much larger than the B_s^0 oscillation frequency, $\mathcal{D}$ would approach 0. For a double-Gaussian resolution model, the dilution is given by

$$\mathcal{D} = f_1 e^{-\sigma_1^2 \Delta m_s^2/2} + (1 - f_1) e^{-\sigma_2^2 \Delta m_s^2/2}, \tag{8.3}$$

where σ_1 and σ_2 are the widths of the two Gaussians, f_1 is the relative fraction of candidates described by the first Gaussian with respect to the second and Δm_s is the oscillation frequency of B_s^0 mesons. An effective resolution is calculated from the dilution as,

$$\sigma_{eff} = \sqrt{(-2/\Delta m_s^2) \ln \mathcal{D}}, \tag{8.4}$$

which expresses the resolution effects in one quantity that causes a damping of the magnitude of the B_s^0 oscillation. For the analyzed sample of simulated Run I $B_s^0 \to D_s^- K^+ \pi^- \pi^+$ candidates, the effective average resolution is found to be $\sigma_{eff} = 39.1 \pm 0.3$ fs. To determine the relation between the per-event decay time error $\sigma_{i,t}$ and the actual resolution $\sigma_{i,eff}$, the simulated sample is divided into equal-statistics slices of $\sigma_i(t_{B_s^0})$. For each slice, the effective resolution is determined as described above. The detailed fit results in each slice are shown in Appendix B. The right side of Figure 8.2 shows the obtained values for σ_{eff} as a function of the per-event decay time error σ_t.

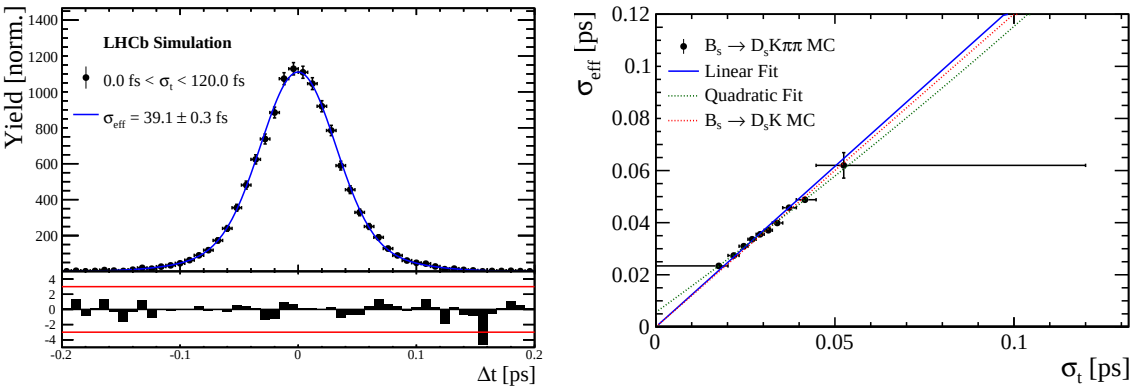

Figure 8.2.: (Left) Difference of the true and measured decay time of simulated $B_s^0 \to D_s^- K^+ \pi^- \pi^+$ candidates. The fit performed using two Gaussian functions is overlaid. (Right) The measured resolution σ_{eff} as function of the per-event decay time error estimate σ_t for $B_s^0 \to D_s^- K^+ \pi^- \pi^+$ candidates, simulated under Run I conditions. The fitted calibration curve is shown in blue.

A linear function, with a fixed offset of zero is used to parametrize the distribution

and the obtained values are

$$\sigma_{eff}^{MC}(\sigma_t) = (1.232 \pm 0.010)\,\sigma_t \tag{8.5}$$

.

For comparison, the calibration function found for simulated $B_s^0 \to D_s^- K^-$ candidates is also shown in Figure 8.2 [4]:

$$\sigma_{eff}^{D_s K,sim}(\sigma_t) = (1.201 \pm 0.013)\,\sigma_t. \tag{8.6}$$

Due to the reasonable agreement between the scale factors for simulated Run I samples of $B_s^0 \to D_s^- K^+\pi^-\pi^+$ and $B_s^0 \to D_s^- K^+$ decays, it is justifiable to take the resolution scaling for $B_s^0 \to D_s^- K^+$ data from Run I as input for the selected $B_s^0 \to D_s^- K^+\pi^-\pi^+$ Run I data. The calibration function is given by [4]

$$\sigma_{eff}^{D_s K,data}(\sigma_t) = (10.26 \pm 1.52)\,\text{fs} + (1.280 \pm 0.042)\,\sigma_t, \tag{8.7}$$

and is used to calibrate the per-event decay-time errors $\sigma_i(t_{B_s^0})$ of $B_s^0 \to D_s^- K^+\pi^-\pi^+$ signal candidates for Run I.

8.1.2. Calibration for data taken in Run II

For the resolution calibration of Run II data, a dedicated sample of fake $B_s^0 \to D_s^- K^+\pi^-\pi^+$ candidates, where the D_s^- candidates originate from the primary vertex, is selected. No selection requirements related to lifetime or impact parameter of the B_s^0 candidate is applied, allowing for a study of the resolution. Each D_s^- candidate is combined with a kaon and two pions, which originate from the PV and are not related to a specific mother particle. Imposing this selection, a sample of fake B_s^0 candidates with a known true decay-time of $t_{true} = 0$ is obtained and the difference of the measured decay time, t, of these candidates with respect to the true decay time is attributed to the decay time resolution. Due to changes in the VELO algorithm that estimates the uncertainty on the B_s^0 decay time after 2016, the shape of the distributions of the unscaled decay time errors $\sigma_i(t_{B_s^0})$ for data samples taken in 2016 and 2017 are significantly different. This difference is shown in Figure B.2, in the Appendix. Therefore, the scaling of the decay-time uncertainty is treated separately for data taken during Run II, before the change (2015 and 2016) and after it (2017).
The complete set of selection requirements used to isolate D_s^- mesons originating from

the PV and combining them with $(K^+\pi^-\pi^+)$ candidates from the PV is summarized in Table 8.1. The invariant mass distribution of the selected D_s^- candidates is shown in Figure 8.3. A fit to the data is overlaid, where an exponential function is used for the description of the combinatorial background and combined with a Gaussian function to model the signal peak. To separate true D_s^- candidates from random combinations, the sPlot method [71] is used to statistically subtract the background from the sample. Figure 8.4 shows the negative side of the background subtracted decay-time distribution of the fake B_s^0 candidates. Since some D_s^- candidates might actually originate from true, physical decays of B_s^0 mesons with very short lifetimes, the decay-time distribution of the fake B_s^0 candidates might show a bias towards positive decay times. Therefore, the decay-time resolution is determined exclusively from the negative decay-time distribution, choosing them sum of two single-side Gaussian functions as fit model.

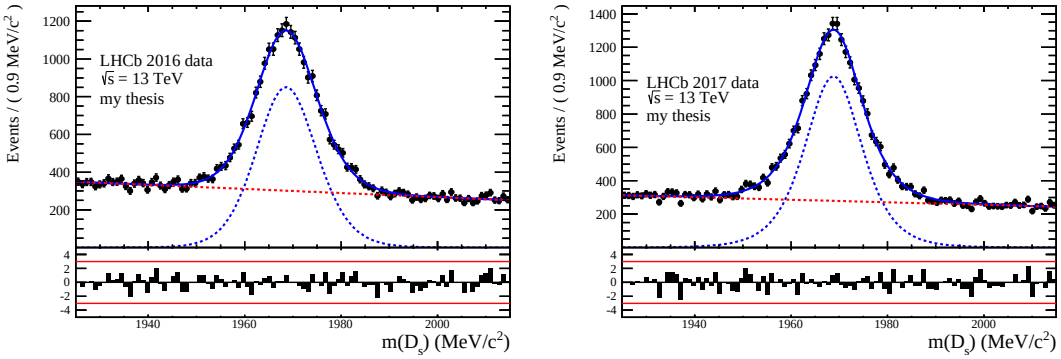

Figure 8.3.: The invariant mass distribution for D_s^- candidates that originate from the primary vertex for data taken in (left) 2016 and (right) 2017. The fit described in the text is overlaid.

Similar to the previous section, the analysis is performed in slices of the per-event decay-time error and as discussed, only the left side of the Gaussian is used for the determination of the spread of the distribution. Details of the fit results in each slice are shown in Appendix B.
The resulting calibration functions for data taken in 2015+2016 and 2017 are:

$$\sigma_{eff}^{Data,16}(\sigma_t) = (11.6 \pm 1.6)\,\text{fs} + (0.877 \pm 0.040)\,\sigma_t, \tag{8.8}$$

$$\sigma_{eff}^{Data,17}(\sigma_t) = (6.5 \pm 1.4)\,\text{fs} + (0.961 \pm 0.036)\,\sigma_t, \tag{8.9}$$

where the uncertainties are purely statistical.

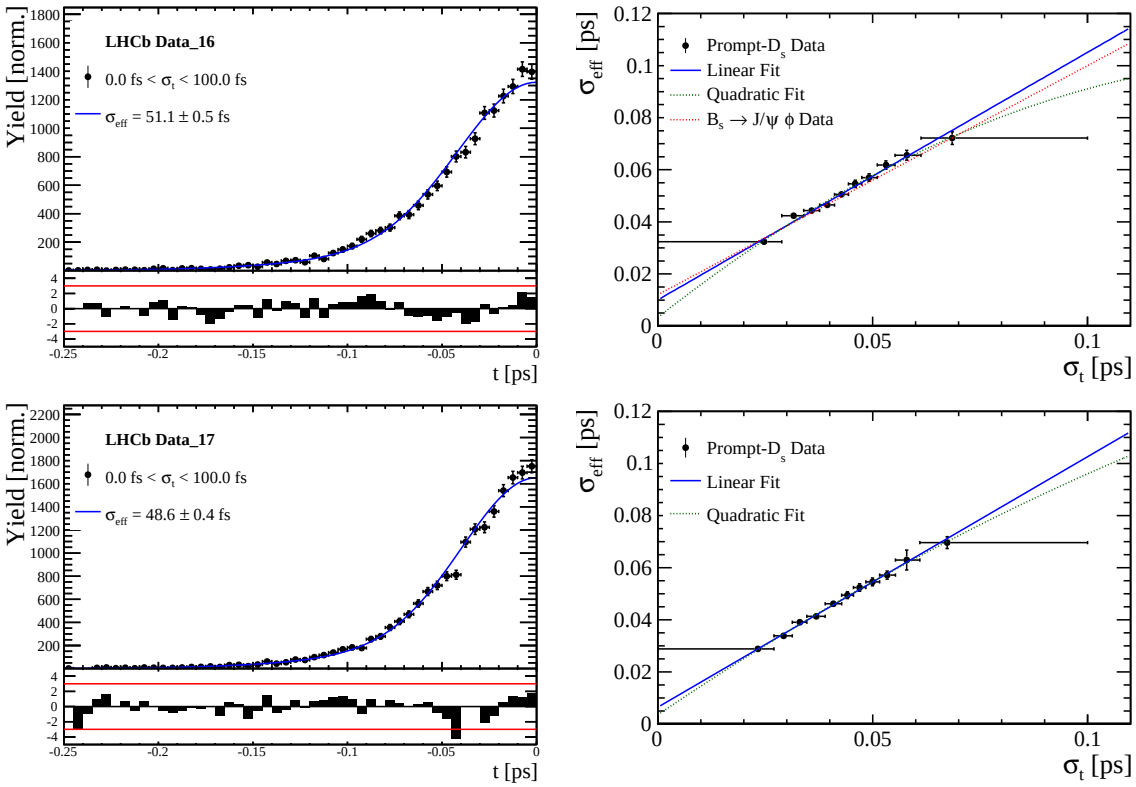

Figure 8.4.: (Left) Decay-time distribution for fake B_s^0 candidates from D_s^- candidates produced in the PV, combined with a random $K^-\pi^+\pi^-$ triplet, originating from the PV. The fit discussed in the text is overlaid. (Right) The measured resolution σ_{eff} as function of the per-event decay time error estimate σ_t for fake B_s candidates. The fitted calibration curve is shown in blue. The top column shows the distributions for 2016 data, while the distributions for 2017 data are shown in the bottom.

8.2. Decay-time acceptance

The decay-time distribution of the B_s^0 mesons is sculpted due to the geometry of the LHCb detector and the applied selection requirements, which are described in Chapter 6. The observed decay-time distribution is therefore distorted from the theoretically predicted one:

$$\frac{\Gamma(t)^{observed}}{dt} = \frac{\Gamma(t)^{theory}}{dt} \cdot \epsilon(t), \tag{8.10}$$

where $\epsilon(t)$ is the analytic shape of the decay-time acceptance. Due to the strong correlation of the CP observables and the acceptance shape, a direct determination from $B_s^0 \to D_s^- K^+\pi^-\pi^+$ signal decays along with the measurement of C, D_f and S_f is

not possible. Therefore, the acceptance effect for the decay-time distribution of $B_s^0 \to D_s^- K^+\pi^-\pi^+$ signal candidates is evaluated using a combination of simulated and real data for $B_s^0 \to D_s^-\pi^+\pi^-\pi^+$ decays, as well as $B_d^0 \to D_s^- K^+\pi^-\pi^+$ candidates.
The shape of the decay time acceptance can be determined using a time-dependent fit to the combined decay-time distribution of $B_s^0 \to D_s^-\pi^+\pi^-\pi^+$ and $\bar{B}_s^0 \to D_s^+\pi^-\pi^+\pi^-$ candidates in data, where the CP coefficients vanish in the decay rate, because of the flavor specific nature of this decay:

$$\frac{\Gamma(t)^{observed}_{B_s^0/\bar{B}_s^0}}{dt} \propto (\cos(\frac{\Delta\Gamma_s\, t'}{2})e^{-\Gamma_s\, t}) \cdot \epsilon(t)_{D_s^-\pi^+\pi^-\pi^+}, \tag{8.11}$$

where $\Gamma(t)^{observed}_{B_s^0/\bar{B}_s^0}$ symbolizes the flavor-averaged decay rate without information on the production flavor of the B_s^0 and $\Delta\Gamma_s$ is the lifetime difference of the low and high mass eigenstates, B_H and B_L, of the B_s^0 system as discussed in Chapter 3. In addition, the shape obtained from a fit to this distribution needs to be corrected for the small difference observed between the $B_s^0 \to D_s^- K^+\pi^-\pi^+$ and $B_s^0 \to D_s^-\pi^+\pi^-\pi^+$ decays. To allow for a straightforward propagation of uncertainties, a simultaneous, time-dependent fit to signal candidates from $B_s^0 \to D_s^-\pi^+\pi^-\pi^+$ data, $B_d^0 \to D_s^- K^-\pi^+\pi^-$ data, $B_s^0 \to D_s^- K^+\pi^-\pi^+$ simulation and $B_s^0 \to D_s^-\pi^+\pi^-\pi^+$ simulation is performed. The shape of the acceptances in those 4 samples is assumed to be:

- $B_s^0 \to D_s^- K^-\pi^+\pi^-$ simulation: $\epsilon^{Sim}_{D_s^- K^-\pi^+\pi^-}(t)$.
- $B_s^0 \to D_s^-\pi^-\pi^+\pi^-$ simulation: $\epsilon^{Sim}_{D_s^-\pi^-\pi^+\pi^-}(t) = R(t) \cdot \epsilon^{Sim}_{D_s^- K^-\pi^+\pi^-}(t)$.
- $B_s^0 \to D_s^-\pi^-\pi^+\pi^-$ data: $\epsilon^{Data}_{D_s^-\pi^-\pi^+\pi^-}(t) = R(t) \cdot \epsilon^{Data}_{D_s^- K^-\pi^+\pi^-}(t)$.
- $B_d^0 \to D_s^- K^-\pi^+\pi^-$ data: $\epsilon^{Data}_{D_s^- K^-\pi^+\pi^-}(t)$,

where $\epsilon^{Sim}_{D_s^- K^+\pi^-\pi^+}(t)$ represents the acceptance in $B_s^0 \to D_s^- K^+\pi^-\pi^+$ simulation, $R(t)$ represents the ratio of acceptance shapes in the $B_s^0 \to D_s^-\pi^+\pi^-\pi^+$ and the $B_s^0 \to D_s^- K^+\pi^-\pi^+$ sample, which is assumed to be identical for the simulation and data, and the final acceptance shape in the $B_s^0 \to D_s^- K^+\pi^-\pi^+$ data sample is represented by $\epsilon^{Data}_{D_s^- K^+\pi^-\pi^+}(t)$. The control channel $B_d^0 \to D_s^- K^-\pi^+\pi^-$, that is expected to be similarly affected by the decay-time acceptance to the $B_s^0 \to D_s^- K^+\pi^-\pi^+$ channel, is included to increase the statistical precision of the simultaneous fit.
In each of the four cases, a fit model of the form

$$\mathcal{P}(t,\delta t) = \left[e^{-\Gamma\, t} \cdot \cosh\left(\frac{\Delta\Gamma\, t'}{2}\right) \otimes \mathcal{R}(t-t',\delta t)\right] \cdot \epsilon(t), \tag{8.12}$$

is used to describe the decay-time distribution. In Equation 8.12, the term describing the theoretical shape of the decay-time distribution, $e^{-\Gamma t} \cdot \cosh\left(\frac{\Delta\Gamma t'}{2}\right)$, is convoluted ($\otimes$) with the decay-time resolution model $\mathcal{R}(t - t', \delta t)$ that was determined in the previous Section (8.1). The resolution model transforms the theoretical decay time (t) into the measured time (t'), effectively smearing it with a Gaussian function of width δt, that represents the uncertainty on the decay-time measurement.
For the part of the simultaneous fit to real collision data samples, the values for $\Gamma_{s,d}$ and $\Delta\Gamma_{s,d}$ are fixed to the latest results from the Heavy Flavor Averaging Group [77], while for the fit to simulated samples, the generated values are used. The functional shape of the decay-time acceptance $\epsilon(t)$ is modeled using third order polynomials, so-called cubic splines, allowing for the analytical computation of the decay-time integrals appearing in the final time-dependent PDF [78]. The splines are parametrized by so-called knots, $t_0, t_1, \ldots, t_N$, which determine their respective boundaries. Two knots are located by default at the lower and upper edge of the interval allowed for the B_s^0/B_d^0 decay time and the remaining ones are chosen such that there is an approximately equal amount of signal candidates in-between two consecutive knots. In the basis of cubic b-splines, $b_i(t)$, where every b-spline is an independent cubic polynomial, the acceptance is constructed as:

$$\epsilon(t) = \sum_{i=0}^{N=6} v_i \, b_i(t), \tag{8.13}$$

where the spline coefficients v_i are determined from the simultaneous fit. Extensive studies were performed to determine the minimal amount of knots sufficient to properly describe the decay time acceptance. It was found that at least $N = 6$ knots are necessary for a sufficient fit quality. To normalize the overall scale of the acceptance function, one of the spline coefficients needs to be set to 1. For the presented analysis, the second to last coefficient v_{N-1} is fixed to unity for all acceptances. The regions of the distributions for very large $B_{s,d}^0$ decay-times suffer from little statistics. To ensure stability of the spline fit in that region, the last coefficient v_N is fixed using a linear extrapolation from the two previous coefficients:

$$v_N = v_{N-1} + \frac{v_{N-2} - v_{N-1}}{t_{N-2} - t_{N-1}} \cdot (t_N - t_{N-1}). \tag{8.14}$$

The shapes are determined individually for the four disjoint analysis sample introduced in Chapter 6.1. Representatively, the distributions and obtained fit values for the category Run I,L0-TOS are shown in Figure 8.5 and Table 8.2. All distributions and

Tables that summarize the shapes and the obtained fit values can be found in Appendix C.

In each distribution, the typical shape of $\epsilon(t)$ is observed: a steep rise from small decay-times, where the efficiency is low due to direct requirements on the flight distance and the lifetime of B_s^0 candidates; an almost constant, maximum efficiency for the region of medium decay-times; and an approximately linear drop of $\epsilon(t)$ for large decay-times, which can mainly be attributed to the geometry of the VELO [79].

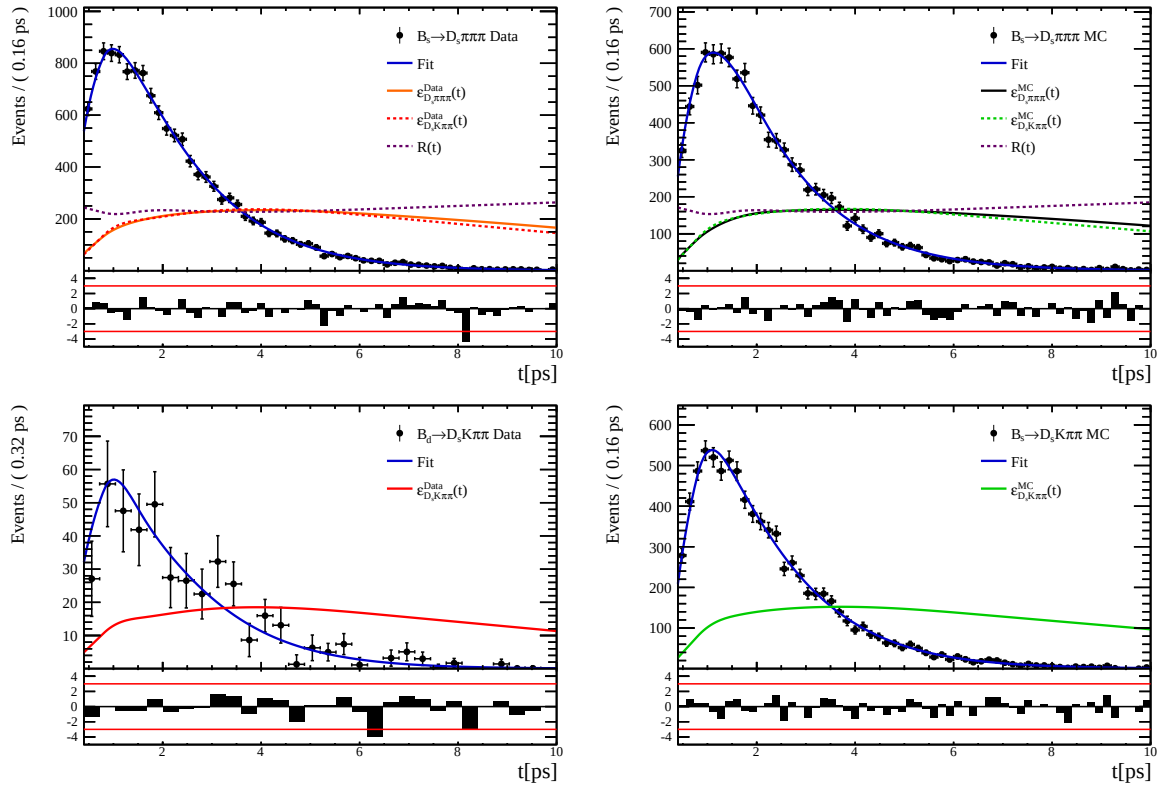

Figure 8.5.: Decay-time fit projections for $B_s^0 \to D_s^- \pi^+ \pi^- \pi^+$ data (top-left), $B_s^0 \to D_s^- \pi^+ \pi^- \pi^+$ simulation (top-right), $B_d^0 \to D_s^- K^- \pi^+ \pi^-$ data (bottom-left) and $B_s^0 \to D_s^- K^+ \pi^- \pi^+$ simulation (bottom-right), representatively shown for the data category Run I,L0-TOS. The respective acceptance functions are overlaid in an arbitrary scale.

Table 8.1.: Offline selection requirements for fake B_s candidates from promptly produced D_s candidates combined with random prompt $K\pi\pi$ bachelor tracks.

	Description	Requirement
$B_s^0 \to D_s^- K^+\pi^-\pi^+$	χ^2_{vtx}/ndof	< 8
	χ^2_{DTF}/ndof	< 15
	$t_{B_s^0}$	$< 0\ ps$
$D_s^- \to h^- h^* h^-$	χ^2_{vtx}/ndof	< 5
	$\cos(\vartheta)$	> 0.99994
	χ^2_{FD}	> 9
	p_T	> 1800 MeV
	χ^2_{IP}	< 9
	$\chi^2_{IP}(h)$	> 5
	Wrong PV veto	nPV $= 1$ $\|\|$ $\min(\Delta\chi^2_{IP}) > 20$
$D_s^- \to K^+K^-\pi^-$	D^0 veto	$m(K^+K^-) < 1840$ MeV
	D^- veto	$m(K^+K^-_\pi\pi^-) \neq m(D^-) \pm 30$ MeV
	Λ_c^- veto	$m(K^-K^+_p\pi^-) \neq m(\Lambda_c^-) \pm 30$ MeV
$D_s^- \to \phi\pi^-$	$m(K^-K^+)$	$= m_\phi \pm 20$ MeV
	$\Delta\log\mathcal{L}_{K-\pi}(K^+)$	> -10
	$\Delta\log\mathcal{L}_{K-\pi}(K^-)$	> -10
	$\Delta\log\mathcal{L}_{K-\pi}(\pi^-)$	< 20
$D_s^- \to K^*(892)K^-$	$m(K^+K^-)$	$\neq m_\phi \pm 20$ MeV
	$m(K^+\pi^-)$	$= m_{K^*(892)} \pm 75$ MeV
	$\Delta\log\mathcal{L}_{K-\pi}(K^+)$	> -10
	$\Delta\log\mathcal{L}_{K-\pi}(K^-)$	> -5
	$\Delta\log\mathcal{L}_{K-\pi}(\pi^-)$	< 20
$D_s^- \to (K^+K^-\pi^-)_{NR}$	$m(K^+K^-)$	$\neq m_\phi \pm 20$ MeV
	$m(K^+\pi^-)$	$\neq m_{K^*(892)} \pm 75$ MeV
	$\Delta\log\mathcal{L}_{K-\pi}(K^+)$	> 5
	$\Delta\log\mathcal{L}_{K-\pi}(K^-)$	> 5
	$\Delta\log\mathcal{L}_{K-\pi}(\pi^-)$	< 10
$D_s \to \pi^-\pi^+\pi^-$	$\Delta\log\mathcal{L}_{K-\pi}(h)$	< 10
	$\Delta\log\mathcal{L}_{K-p}(h^\pm)$	< 10
	D^0 veto	$m(\pi^+\pi^-) < 1700$ MeV
$X_s \to K^+\pi^+\pi^-$	$\chi^2_{IP}(h^\pm)$	< 40
	$\Delta\log\mathcal{L}_{K-\pi}(K^+)$	> 10
	$\Delta\log\mathcal{L}_{K-\pi}(\pi^\pm)$	< 5
All final state particles	p_T	> 500 MeV

Table 8.2.: Time acceptance parameters for events in category [Run I,L0-TOS].

Knot position	Coefficient	$B_s^0 \to D_s^- K\pi\pi$ data	$B_s^0 \to D_s^- K\pi\pi$ MC	Ratio
0.4	v_0	0.309 ± 0.018	0.410 ± 0.007	1.007 ± 0.029
0.5	v_1	0.694 ± 0.031	0.776 ± 0.011	0.936 ± 0.021
1.4	v_2	0.858 ± 0.043	0.896 ± 0.015	1.004 ± 0.024
2.5	v_3	1.090 ± 0.028	1.099 ± 0.009	0.992 ± 0.015
6.5	v_4	1.0 (fixed)	1.0 (fixed)	1.0 (fixed)
10.0	v_5	0.921 (interpolated)	0.913 (interpolated)	1.007 (interpolated)

Chapter 9

Determination of the B_s^0 production flavor

The knowledge of the initial flavor state of the B_s^0 meson is crucial for the measurement of the $B_s^0 - \bar{B}_s^0$ oscillation and the correct determination of the CP asymmetry in the time-dependent fit. At the LHCb experiment, there are two different sets of algorithms that *tag* the initial B_s^0 flavor: the opposite-side [80] and the same-side [81] tagging algorithms, which are illustrated in Figure 9.1 and discussed in the following.

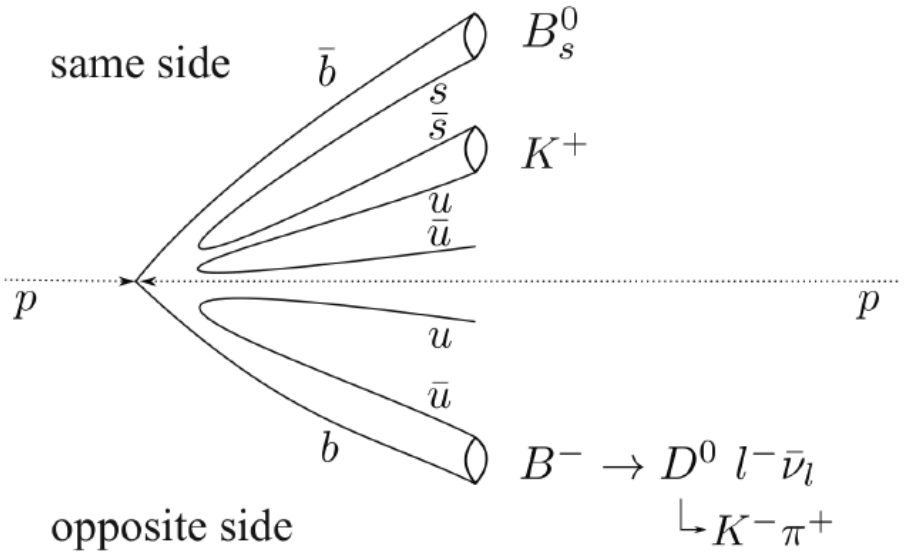

Figure 9.1.: Schematic overview of the flavor tagging algorithms used to determine the initial flavor state of the B_s^0 meson. The identification of a B_s^0 meson, produced via $b\bar{b}$ pair production, and the identification of its flavor using the same-side (upper half) and the opposite-side (lower half) algorithm is shown. Illustration taken from [25].

The opposite-side (OS) tagging algorithm exploits the fact that the b-quarks are pro-

duced as quark anti-quark pairs at the LHC. The OS algorithm uses the b-quark that is not a part of the signal meson and its decay into a final state with a flavor specific charge. Exemplary given in Figure 9.1, the opposite b-quark can hadronize into a B^- meson, which decays into a D^0 and a negatively charged lepton l^-. The charge of the lepton, as well as the charge of the kaon from the D^0 decay, K^-, can be used to determine the flavor of the signal b-quark. Those taggers are called OS electron or OS muon, depending on the flavor of the charged lepton l^-, and OS kaon in case the flavor of the signal b-hadron is determined using the K^-. The combination of them forms the combined OS tagging decision.
The same-side (SS) tagging algorithm benefits from the fact that also the strange quark, which hadronizes with the signal b-quark to from the B_s^0 meson, is produced dominantly as a quark anti-quark pair $s\bar{s}$. The s-quark that is not part of the signal B_s^0 hadronizes with an up quark to form a kaon in approximately half of the cases[81]. Therefore, the charge of this kaon defines the initial state flavor of the B_s^0. This specific same-side algorithm is called same-side kaon tagger (SSK).
Every tagging algorithm is prone to misidentify the signal B_s^0 candidate at a certain mistag rate $\omega = (N(wrong)/N(all))$. This might be caused by particle misidentification, flavor oscillation of the neutral opposite-site B-meson or by uninvolved hadrons from the underlying hadronic environment, which tracks are wrongly associated to the signal. An imperfect determination of the initial flavor of the B_s^0 dilutes the observed CP asymmetry, where a mistag probability of 50% corresponds to a random tagging decision that results in the complete loss of sensitivity. Therefore, the dilution by mis-tagging is defined as

$$D_{tag} = 1 - 2\omega. \tag{9.1}$$

The statistical precision, with which the CP asymmetry can be measured, scales as the inverse square root of the effective tagging efficiency:

$$\epsilon_{eff} = \epsilon_{tag}(1 - 2\omega)^2 = \epsilon_{tag} D_{tag}^2, \tag{9.2}$$

which corresponds to the fraction of events that can be used in the measurement assuming no mistag probability. In Equation 9.2, $\epsilon_{tag} = \frac{N(tagged)}{N(all)}$ is the fraction of tagged candidates. For every $B_s^0/\bar{B}_s^0$ candidate, the tagging algorithms provide the flavor tag $q = 1, -1, 0$ for an initial B_s^0, $\bar{B}_s^0$ or no tag. Along with the tagging decision, a prediction for the mistag probability η is given by the respective tagging algorithm. Details on the

procedure used to obtain the predicted mistag probability for the tagging algorithms can be found in [80]. Similarly to the estimated per-event decay time resolution, discussed in Chapter 8.1, the predicted mistag probability η of each tagger has to be calibrated to match the actual observed mistag rate ω. For the calibration, a linear model is used

$$\omega(\eta) = p_0 + p_1 \cdot (\eta - \langle\eta\rangle), \tag{9.3}$$

where $\langle\eta\rangle$ is the average estimated mistag probability. For a perfectly calibrated tagger, the predicted mistag probability would match the actual observed one, $\omega(\eta) = \eta$ and the calibration parameters would be $p_1 = 1$ and $p_0 = \langle\eta\rangle$. Due to small differences of the nuclear interaction cross-sections of oppositely charged kaons and pions, the tagging calibration parameters show a small dependency on the initial state flavor of the B_s^0 ($\bar{B}_s^0$). Therefore, the flavor asymmetry parameters Δp_0, Δp_1 and $\Delta\epsilon_{tag}$ are introduced, where Δ symbolizes that those parameters represent the charge-depended difference of p_i and ϵ_{tag}:

$$\omega(\eta) = (p_0 + \frac{\Delta p_0}{2}) + (p_1 + \frac{\Delta p_0}{2}) \cdot (\eta - \langle\eta\rangle). \tag{9.4}$$

For vanishing charge asymmetry, $\Delta p_i = \Delta\epsilon_{tag} = 0$ holds and Equation 9.3 is recovered.

9.1. Combination of the opposite-side taggers

For the presented analysis, various opposite-side tagging algorithms are used and combined to a single OS tagging response. In the first step, the OS electron, muon and kaon taggers, described in the previous section, are individually calibrated. Additionally the secondary vertex charge tagger, which uses the charge of the particles that form the decay vertex of the opposite-side b-hadron, is used. In the second step, the four tagging decisions and predictions for the mistag probabilities are combined into a single OS-Combo tagger using a dedicated LHCb software tool, the so-called EspressoPerformanceMonitor [82]. The flavor specific decay $B_s^0 \to D_s^-\pi^+\pi^-\pi^+$ is chosen as calibration mode due to the similarity to the signal decay $B_s^0 \to D_s^- K^+\pi^-\pi^+$. For each tagger, a time-dependent fit is performed, measuring the damping of the mixing induced asymmetry $A^{mix}(t)$ due to the mistag rate ω, $A^{mix}(t) = (1 - 2\omega)\cos(\Delta m_s \cdot t)$ [80]. In the time-dependent fits, the damping is determined, exploiting that the relation of the probability to observe a B_s^0 meson with a mixing frequency Δm_s that has not mixed oscillates with the decay time t:

$$p^{no-mix}(t) \propto \frac{1}{2}(1 + (1 - 2\omega)\cos(\Delta m_s \cdot t)) = \frac{1}{2}(1 + A^{mix}(t)). \tag{9.5}$$

Additionally, the dilution of this probability by the finite time resolution, determined in Chapter 8.1, is taken into account:

$$p^{no-mix}(t) \rightarrow \left(p^{no-mix}(t^{'}) \otimes \mathcal{R}(t - t^{'}, \delta t)\right), \tag{9.6}$$

where $\mathcal{R}(t - t^{'}, \delta t)$ is the resolution model. Due to slightly different performances of the tagging algorithms for the two runs, the tagging calibration is carried out separately for Run I and Run II data. Figures 9.2 and 9.3 show the fitted calibration curves for the four used opposite-side tagging algorithms and Tables 9.1 and 9.2 list the measured tagging performances.

Table 9.1.: The flavor tagging performances for the used OS taggers for Run I data, where the first uncertainty is statistical and the second arises from the calibration model.

Tagger	ϵ_{tag}	ω	$\epsilon\langle D^2\rangle = \epsilon_{\text{tag}}(1-2\omega)^2$
OS μ	$(8.713 \pm 0.206)\%$	$(28.893 \pm 0.180(\text{stat}) \pm 2.291(\text{cal}))\%$	$(1.553 \pm 0.045(\text{stat}) \pm 0.337(\text{cal}))\%$
OS e	$(3.201 \pm 0.129)\%$	$(28.792 \pm 0.363(\text{stat}) \pm 3.611(\text{cal}))\%$	$(0.576 \pm 0.030(\text{stat}) \pm 0.196(\text{cal}))\%$
OS K	$(32.230 \pm 0.342)\%$	$(38.451 \pm 0.093(\text{stat}) \pm 1.145(\text{cal}))\%$	$(1.719 \pm 0.033(\text{stat}) \pm 0.341(\text{cal}))\%$
Vertex Charge	$(21.855 \pm 0.302)\%$	$(35.712 \pm 0.091(\text{stat}) \pm 1.474(\text{cal}))\%$	$(1.785 \pm 0.033(\text{stat}) \pm 0.368(\text{cal}))\%$

Table 9.2.: The flavor tagging performances for the used OS taggers for Run II data, where the first uncertainty is statistical and the second arises from the calibration model.

Tagger	ϵ_{tag}	ω	$\epsilon\langle D^2\rangle = \epsilon_{\text{tag}}(1-2\omega)^2$
OS μ	$(9.664 \pm 0.151)\%$	$(30.911 \pm 0.115(\text{stat}) \pm 1.369(\text{cal}))\%$	$(1.409 \pm 0.028(\text{stat}) \pm 0.202(\text{cal}))\%$
OS e	$(4.590 \pm 0.107)\%$	$(33.577 \pm 0.140(\text{stat}) \pm 2.007(\text{cal}))\%$	$(0.495 \pm 0.014(\text{stat}) \pm 0.121(\text{cal}))\%$
OS K	$(20.185 \pm 0.205)\%$	$(36.918 \pm 0.071(\text{stat}) \pm 0.969(\text{cal}))\%$	$(1.382 \pm 0.021(\text{stat}) \pm 0.205(\text{cal}))\%$
Vertex Charge	$(20.597 \pm 0.207)\%$	$(34.751 \pm 0.075(\text{stat}) \pm 0.961(\text{cal}))\%$	$(1.916 \pm 0.027(\text{stat}) \pm 0.242(\text{cal}))\%$

In cases where more than one opposite-side tagging algorithm provides a tag of the B_s^0 flavor, $q = \pm 1$, the decisions are combined to give one final tag q_{OS} with predicted mistag η_{OS} that the tagged meson contains a b ($\bar{b}$) quark $P(b)$ ($P(\bar{b})$) [80]:

$$P(b) = \frac{p(b)}{p(b) + p(\bar{b})}, \; P(\bar{b}) = 1 - P(b), \tag{9.7}$$

where

$$p(b) = \prod_i \left(\frac{1 + q_i}{2} - q_i(1 - \eta_i)\right), \; p(\bar{b}) = \prod_i \left(\frac{1 - q_i}{2} + q_i(1 - \eta_i)\right). \tag{9.8}$$

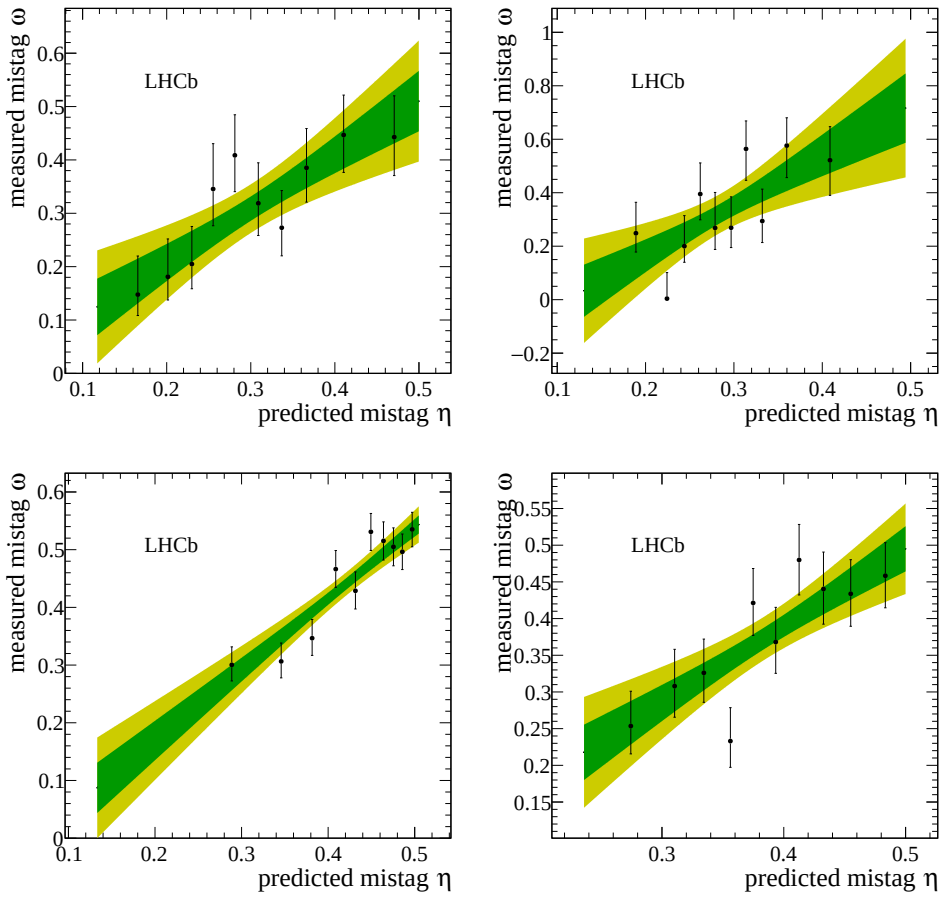

Figure 9.2.: Predicted mistag probability versus measured mistag rate for the (top left) OS muon, (top right) OS electron, (bottom left) OS kaon and (bottom right) OS vertex charge tagger for data collected in Run I. A linear fit, including the 1σ and 2σ error bands is overlaid for each tagger.

Here, q_i is the tagging decision given by OS tagging algorithm i and η_i is the corresponding predicted mistag probability. The combined tagging decision q_{OS} is given as $q_{OS} = -1$ ($q_{OS} = +1$) if $P(b) > P(\bar{b})$ ($P(\bar{b}) > P(b)$) and $\eta_{OS} = 1 - P(b)$ ($\eta_{OS} = 1 - P(\bar{b})$).

9.2. Performance of the combined opposite- and same-side tagger

The combined OS tagging algorithms and the SS kaon tagger are calibrated using a simultaneous fit to the decay-time distribution of $B_s^0 \to D_s^- \pi^+ \pi^- \pi^+$ signal candidates, fitting for the observed mistag rate ω, which is diluting the mixing asymmetry according

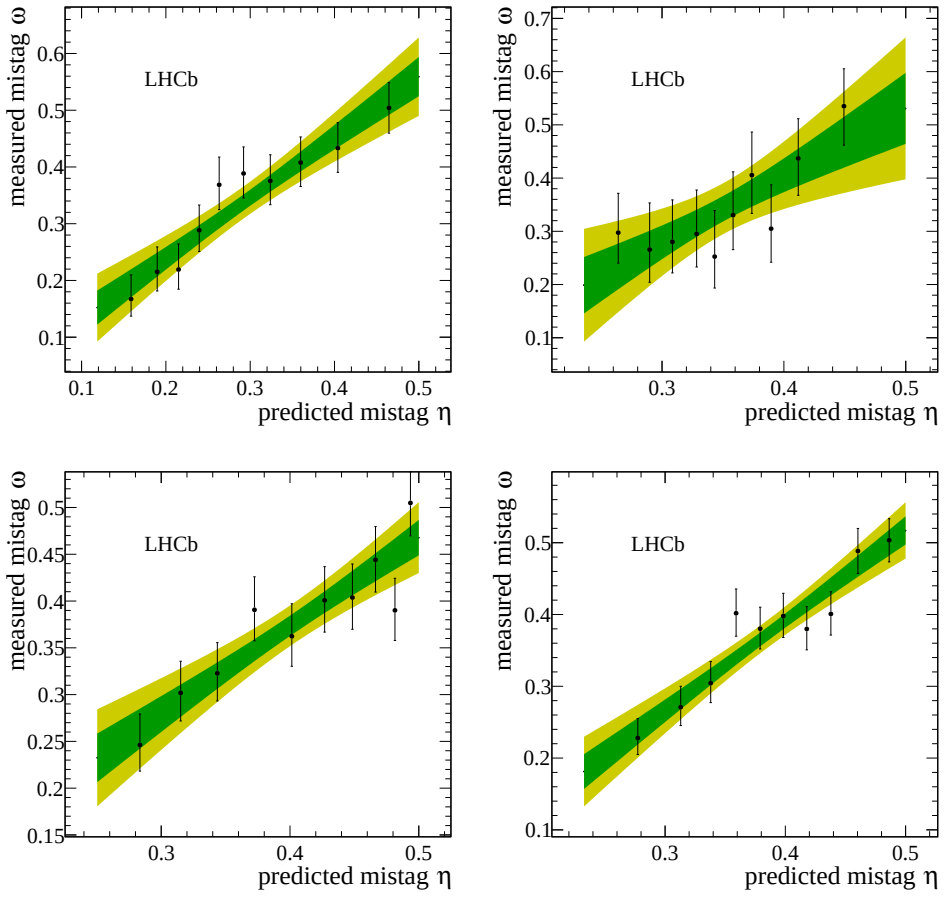

Figure 9.3.: Predicted mistag probability versus measured mistag rate for the (top left) OS muon, (top right) OS electron, (bottom left) OS kaon and (bottom right) OS vertex charge tagger for data collected in Run II. A linear fit, including the 1σ and 2σ error bands is overlaid for each tagger.

to Equation 9.5. This fit is discussed in detail in Chapter 10. The predicted mistag probabilities η_{OS} and η_{SS} are included as per-event observables, effectively giving a larger weight to those events that have a lower mistag probability. The calibrated mistag probabilities obtained by this fit are combined event-by-event, depending on whether the tagging decision ($q_{OS/SS} = \pm 1$) for the opposite-side and same-side algorithm is the same or different, $q_{OS} = q_{SS}$ or $q_{OS} \neq q_{SS}$. For events where one of the tagging decisions is $q_{OS/SS} = 0$, only the other is used. In cases where both algorithms give a tag and they are the same, the combined mistag probability ω_{com} is computed as [80]

$$\omega_{com} = 1 - \frac{1 - \omega_{SS} - \omega_{OS} + \omega_{SS}\omega_{OS}}{1 - \omega_{OS} - \omega_{SS} + 2\omega_{SS}\omega_{OS}}, \tag{9.9}$$

where ω_{SS} and ω_{OS} are the individual mistag probabilities of the OS and OS taggers. In an event where the two decision have different signs, the B-tag from the algorithm with the smaller mistag probability, $\omega_<$, is chosen and the combined mistag is determined as

$$\omega_{com} = 1 - \frac{1 - \omega_>(1 - \omega_<)}{\omega_>(1 - \omega_<) + \omega_<(1 - \omega_>)}, \tag{9.10}$$

where $\omega_>$ is the larger mistag probability. Tables 9.3 and 9.4 report the tagging performances for the OS and SS combination, considering the three mutually exclusive categories where events are OS tagged only, SS only or tagged by both algorithms. It is observed that the tagging efficiency ϵ_{eff} is improved for data taken during Run II, with respect to Run I.

9.3. Production and detection asymmetries

After the calibration of the same-side and opposite-side taging algorithms, two small asymmetries need to be considered. The first asymmetry is due to the fact that, in the pp collisions at LHCb, the production rates of b and $\bar{b}$ hadrons are not expected to be identical [83]. Therefore, the production asymmetry,

$$A_p(B_s^0) = \frac{\sigma(\bar{B}_s^0) - \sigma(B_s^0)}{\sigma(\bar{B}_s^0) + \sigma(B_s^0)}, \tag{9.11}$$

where σ are the corresponding production cross-sections, must be taken into consideration for any CP measurement. A non-zero value for $A_p(B_s^0)$ would distort the measurement of the CP-violating parameters in the fit to $B_s^0 \to D_s^- K^+ \pi^- \pi^+$ data, if

Table 9.3.: The flavor tagging performances for OS tagged only, SS tagged only and both OS and SS tagged events for Run I data.

$B_s \to D_s\pi\pi\pi$	$\epsilon_{tag}[\%]$	$\langle\omega\rangle[\%]$	$\epsilon_{eff}[\%]$
Only OS	14.74 ± 0.11	39.09 ± 0.80	1.25 ± 0.16
Only SS	35.38 ± 0.18	44.26 ± 0.62	1.05 ± 0.18
Both OS-SS	33.04 ± 0.30	37.33 ± 0.73	3.41 ± 0.33
Combined	83.16 ± 0.37	40.59 ± 0.70	5.71 ± 0.40

Table 9.4.: The flavor tagging performances for OS tagged only, SS tagged only and both OS and SS tagged events for Run II data.

$B_s \to D_s\pi\pi\pi$	$\epsilon_{tag}[\%]$	$\langle\omega\rangle[\%]$	$\epsilon_{eff}[\%]$
Only OS	11.78 ± 0.05	37.01 ± 0.51	1.15 ± 0.07
Only SS	41.28 ± 0.10	42.65 ± 0.35	1.79 ± 0.12
Both OS-SS	28.62 ± 0.15	35.35 ± 0.40	3.63 ± 0.16
Combined	81.68 ± 0.19	39.28 ± 0.40	6.57 ± 0.21

not accounted for. The asymmetry defined in Equation 9.11 was measured by LHCb for pp collisions at center of mass energies of $\sqrt{s} = 7\ TeV$ and $\sqrt{s} = 8\ TeV$ (Run I) using a time-dependent analysis of $B_s^0 \to D_s^-\pi^+$ decays [83], where they are found to be:

$$A_p(B_s^0)_{7\ TeV} = (-0.506 \pm 1.90)\% \tag{9.12}$$

$$A_p(B_s^0)_{8\ TeV} = (\ \ 0.164 \pm 1.30)\% \tag{9.13}$$

$$A_p(B_s^0)_{\text{Run I}} = (-0.045 \pm 1.04)\%. \tag{9.14}$$

The results given above are averaged over the transverse momentum p_t and pseudo-rapidity η of the B_s^0 meson. Since the value of $A_p(B_s^0)$ depends on the kinematics of the B_s^0 meson [83], it is additionally given in slices of p_t and η. A complete summary with all values for $A_p(B_s^0)$ in those slices can be found in Appendix D. For data taken during Run II, no measurement of $A_p(B_s^0)$ is available yet. Therefore, the production asymmetry for B_s^0 candidates recorded in Run II is determined in the time-dependent fit to $B_s^0 \to D_s^-\pi^+\pi^-\pi^+$ data and subsequently used as input for the fit to the $B_s^0 \to D_s^-K^+\pi^-\pi^+$ sample. The result is shown in Table 10.1.

The second effect originates from the charge-dependence of the nuclear cross-section of the kaon. Since the presented measurement of CP violation in $B_s^0 \to D_s^-K^+\pi^-\pi^+$ decays is sensitive to a possible detection asymmetry of the charged kaon, it is indispens-

able to determine this detector induced effect, as ignoring the kaon asymmetry would fake additional CP violation. It is found that the direct determination of the kaon detection asymmetry, $A^{det}(K)$, is experimentally challenging, while the combined two-particle asymmetry of a kaon-pion pair,

$$A^{det}(K^-\pi^+) = \frac{\epsilon^{det}(K^-\pi^+) - \epsilon^{det}(K^+\pi^-)}{\epsilon^{det}(K^-\pi^+) + \epsilon^{det}(K^+\pi^-)}, \tag{9.15}$$

is easier accessible [84]. Therefore, the asymmetry defined in Equation 9.15 is used for the presented analysis. It can be measured using the difference in asymmetries in two decays of charged D mesons, $D^+ \to K^-\pi^+\pi^+$ and $D^+ \to K_s^0\pi^+$ [85],

$$\begin{aligned} A^{det}(K^-\pi^+) =& \frac{N(D^+ \to K^-\pi^+\pi^+) - N(D^- \to K^+\pi^-\pi^-)}{N(D^+ \to K^-\pi^+\pi^+) + N(D^- \to K^+\pi^-\pi^-)} \\ &- \frac{N(D^+ \to K_s^0\pi^+) - N(D^- \to K_s^0\pi^-)}{N(D^+ \to K_s^0\pi^+) + N(D^- \to K_s^0\pi^-)} \\ &- A(K^0). \end{aligned} \tag{9.16}$$

A possible CP-violating effect in the $D^+ \to K_s^0\pi^+$ decay, which would distort the measurement of $A^{det}(K^-\pi^+)$, is predicted to be smaller than 10^{-4} in the Standard Model [86]. The asymmetry in the neutral kaon system, $A(K^0)$, needs to be taken into acount as a small correction. For the determination of the $K^-\pi^+$ detection asymmetry, a dedicated LHCb software tool [85] is used. To extract $A^{det}(K^-\pi^+)$ for data taken during Run I and Run II of LHCb, large calibration samples of $D^\pm \to K^\pm\pi^\pm\pi^\pm$ and $D^\pm \to K_s^0\pi^\pm$ decays are exploited. First, weights according to the momentum and pseudo-rapidity of the kaon and the pion are applied to match the kinematic distributions of the $D^\pm$ decays to the $B_s^0 \to D_s^- K^+\pi^-\pi^+$ signal decay. Then, fits to the invariant $m(K^-\pi^+\pi^+)/m(K^+\pi^-\pi^-)$ and $m(K_s^0\pi^+)/m(K_s^0\pi^-)$ distributions are performed to extract the respective yields and calculate the detection asymmetry defined in Equation 9.16. The PDFs used to determine the yields consist of a Gaussian-function for the signal component and an exponential-function for the residual background. Since the asymmetry depends on the pp collision energy, as well as the polarity of the bending magnet, $A^{det}(K^-\pi^+)$ is determined per year of data taking and magnet polarity. Figure 9.4 shows the invariant mass distributions and fit projections for data taken in 2015 with negative magnet polarity, representatively. The obtained asymmetries are summarized in Table 9.5 and used as input for the time-dependent fit to the $B_s^0 \to D_s^- K^+\pi^-\pi^+$ data sample.

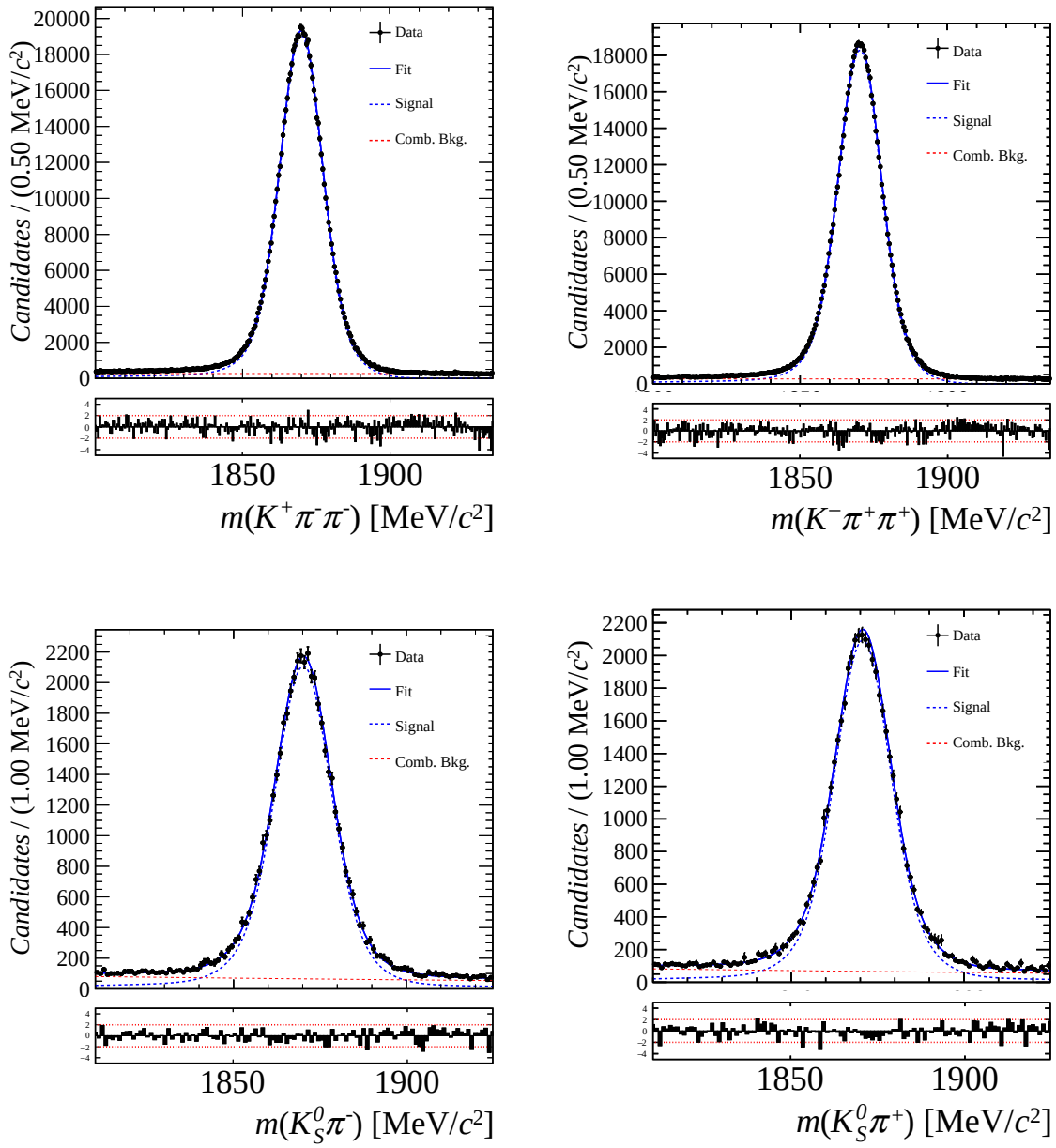

Figure 9.4.: Distributions of the invariant mass of (top) $D^{\pm} \to K^{\pm}\pi^{\pm}\pi^{\pm}$ and (bottom) $D^{\pm} \to K_s^0\pi^{\pm}$ candidates for data taken in 2015 with negative magnet polarity from the calibration samples. A fit described in the text is overlaid.

Data sample	$A^{det}(K^-\pi^+)$
Run I	
2011, mag. up	-2.01 ± 0.32
2011, mag. down	-0.16 ± 0.28
2011, average	-1.09 ± 0.21
2012, mag. up	-0.90 ± 0.20
2012, mag. down	-1.01 ± 0.22
2012, average	-0.96 ± 0.15
Run II	
mag. up	-1.16 ± 0.34
mag. down	-0.65 ± 0.27
average	-0.91 ± 0.22

Table 9.5.: Summary of the $K^-\pi^+$ detection asymmetries obtained from the fits to the Run I and Run II calibration samples.

Chapter 10

Model-independent determination of the CKM angle γ

This Chapter describes the phase-space integrated decay-time fits to $B_s^0 \to D_s^- \pi^+ \pi^- \pi^+$ and $B_s^0 \to D_s^- K^+ \pi^- \pi^+$ data. For both samples, the sFit technique [71] is implemented to statistically subtract the background, leaving only the signal B_s^0 candidates in the final sample. Consequently, a PDF based purely on the signal model is used to describe the respective decay-time distribution. The signal weights are calculated based on the fit to the reconstructed B_s^0 mass distribution described in Chapter 7. Several event-dependent observables, such as the tagging decisions q_i, the mistag probability estimates η_i (i =OS,SS) and the decay-time error δt_i, are used in the fits to data. The signal PDF is therefore conditional on those observables:

$$\mathcal{P}(t_i|\delta t_i, q^i_{OS}, \eta^i_{OS}, q^i_{SS}, \eta^i_{SS}) \propto \left[\prod_i p(t'_i|q^i_{OS}, \eta^i_{OS}, q^i_{SS}, \eta^i_{SS}) \otimes \mathcal{R}(t_i - t'_i, \delta t_i) \cdot \epsilon(t)\right], \tag{10.1}$$

where $p(t|q^i_{OS}, \eta^i_{OS}, q^i_{SS}, \eta^i_{SS})$ is given by Equation 3.60. The shape and parameters of the event-dependent decay-time resolution $\mathcal{R}(t_i - t'_i, \delta t_i)$ and the acceptance $\epsilon(t)$ are fixed to the values obtained by the dedicated studies described in Chapter 8. The values for the decay width Γ_s and the decay width difference $\Delta\Gamma_s$ are fixed to the most recent results from the Heavy Flavor Averaging Group [77].

In principal, the mixing frequency of B_s^0 mesons, Δm_s, can be measured in the time-dependent fit to the $B_s^0 \to D_s^- \pi^+ \pi^- \pi^+$ sample. Since the measurement of Δm_s in this channel will be the world's most precise determination of this quantity, all contributing systematic uncertainties have to be evaluated carefully and therefore the central value of Δm_s is not yet unblinded at the time of writing. It will be published in the paper

describing the presented analysis [6]. For the calibration of the tagging parameters from the fit to $B_s^0 \to D_s^- \pi^+ \pi^- \pi^+$ data, the exact value of Δm_s is not needed, since only the damping of the mixing amplitude A_{mix} determines the observed mistag rate ω. For the measurement of the CP-violating parameters from $B_s^0 \to D_s^- K^+ \pi^- \pi^+$ decays, the value of Δm_s is taken as an input from [77].
The logarithm of the likelihood $\mathcal{L}$ is built from the signal PDF shown in Equation 10.1,

$$\begin{aligned} \ln(\mathcal{L}) &= \ln(\mathcal{P}(t_i|\delta t_i, q^i_{OS}, \eta^i_{OS}, q^i_{SS}, \eta^i_{SS})) \\ &= \sum_i^N \Big(p(t_i^{'}|q^i_{OS}, \eta^i_{OS}, q^i_{SS}, \eta^i_{SS}) \otimes \mathcal{R}(t_i - t_i^{'}, \delta t_i) \cdot \epsilon(t) \Big) , \end{aligned} \tag{10.2}$$

where N is the number of signal events observed in the respective data sample. The likelihood function given in Equation 10.2 is maximized to extract the set of most likely physics parameters. All maximum unbinnned likelihood fits are performed simultaneously in the four disjoint data categories introduced in Chapter 6.1, using the respective input for the decay-time resolution, acceptance and tagging parameters.

10.1. Fit to $B_s^0 \to D_s^- \pi^+ \pi^- \pi^+$ signal data

The calibration parameters for the combined OS tagger and the SS kaon tagger, as well as the B_s^0 production asymmetry A_P for Run II, are determined using a fit to the decay-time distribution of $B_s^0 \to D_s^- \pi^+ \pi^- \pi^+$ signal candidates.
Since the decay $B_s^0 \to D_s^- \pi^+ \pi^- \pi^+$ is flavor specific, e.q. the $B_s^0 \to D_s^- \pi^+ \pi^- \pi^+$ transition is allowed but the $B_s^0 \to D_s^+ \pi^- \pi^+ \pi^-$ is not, the interference between B_s^0 and $\bar{B}_s^0$ decays with the same charge final state vanishes. Therefore, no CP violation is expected to manifest in this decay and the CP coefficients from Equations 3.61, 3.62 and 3.63 can be fixed to $C = 1$ and $D_f = D_{\bar{f}} = S_f = S_{\bar{f}} = 0$,

$$\int P(x, t, q_t, q_f) \mathrm{d}x \propto [\cosh\left(\frac{\Delta\Gamma\, t}{2}\right) + q_t q_f \cos\left(m_s\, t\right)] e^{-\Gamma_s t}, \tag{10.3}$$

leaving only two terms which are sensitive to $\Delta\Gamma_s$ and Δm_s.
The background-subtracted decay-time distribution and the time-dependent asymmetry A_{mix} between mixed and unmixed B_s^0 candidates are shown in Figure 10.1 along with the fit projections. The periodical time-dependence of the decay rate for mixed and unmixed B_s^0 ($\bar{B}_s^0$) candidates (top-right) is clearly visible, while the dilution of the mixing

asymmetry A_{mix} (bottom) allows to quantify the observed mistag rate ω.
Table 10.1 summarizes the obtained fit parameters. The fitted values for the tagging parameters and the B_s^0 production asymmetry are taken as input for the fit to $B_s^0 \to D_s^- K^+\pi^-\pi^+$ signal. The value obtained for A_P for data taken during Run I, given in Equation 9.14, as well as the value obtained for Run II, given in Table 10.1, are compatible with zero within their uncertainties, showing no significant averaged production asymmetry between B_s^0 and $\bar{B}_s^0$ candidates.

Table 10.1.: Parameters determined from the fit to the background-subtracted $B_s^0 \to D_s^-\pi^+\pi^-\pi^+$ decay-time distribution. The uncertainties are statistical and systematic, respectively.

Fit Parameter	Run-I	Run-II
p_0^{OS}	0.398 ± 0.010 ± 0.010	0.372 ± 0.005 ± 0.005
p_1^{OS}	0.895 ± 0.085 ± 0.090	0.788 ± 0.043 ± 0.030
Δp_0^{OS}	0.030 ± 0.011 ± 0.002	0.008 ± 0.006 ± 0.001
Δp_1^{OS}	0.011 ± 0.095 ± 0.017	0.067 ± 0.052 ± 0.002
$\epsilon_{\text{tag}}^{OS}$ [%]	47.775 ± 0.365 ± 0.067	40.399 ± 0.182 ± 0.029
$\Delta\epsilon_{\text{tag}}^{OS}$ [%]	0.016 ± 1.353 ± 0.097	0.316 ± 0.618 ± 0.046
p_0^{SS}	0.444 ± 0.008 ± 0.005	0.428 ± 0.004 ± 0.002
p_1^{SS}	0.949 ± 0.111 ± 0.067	0.787 ± 0.039 ± 0.025
Δp_0^{SS}	-0.019 ± 0.009 ± 0.001	-0.017 ± 0.004 ± 0.000
Δp_1^{SS}	0.064 ± 0.124 ± 0.017	0.028 ± 0.048 ± 0.006
$\epsilon_{\text{tag}}^{SS}$ [%]	68.426 ± 0.340 ± 0.013	69.903 ± 0.170 ± 0.007
$\Delta\epsilon_{\text{tag}}^{SS}$ [%]	-0.046 ± 1.242 ± 0.082	-0.319 ± 0.575 ± 0.062
A_P [%]	-0.045 (fixed)	-0.183 ± 0.642 ± 0.048

10.2. Fit to $B_s^0 \to D_s^- K^+\pi^-\pi^+$ signal data

For the fit to the background-subtracted $B_s^0 \to D_s^- K^+\pi^-\pi^+$ data, the full time-dependent, phase-space integrated PDF introduced in Chapter 3 is used:

$$\mathcal{P}(t;\vec{\lambda}) = \int \frac{\mathrm{d}\Gamma(x,t,q,f)}{\mathrm{d}t\,\mathrm{d}\Phi_4}\,\mathrm{d}\Phi_4 \propto [\cosh\left(\frac{\Delta\Gamma_s\, t}{2}\right) + q\, f\, C\cos\left(\Delta m_s\, t\right) + D_f \sinh\left(\frac{\Delta\Gamma_s\, t}{2}\right) - q\, S_f \sin\left(\Delta m_s\, t\right)] e^{-\Gamma_s t}, \qquad (10.4)$$

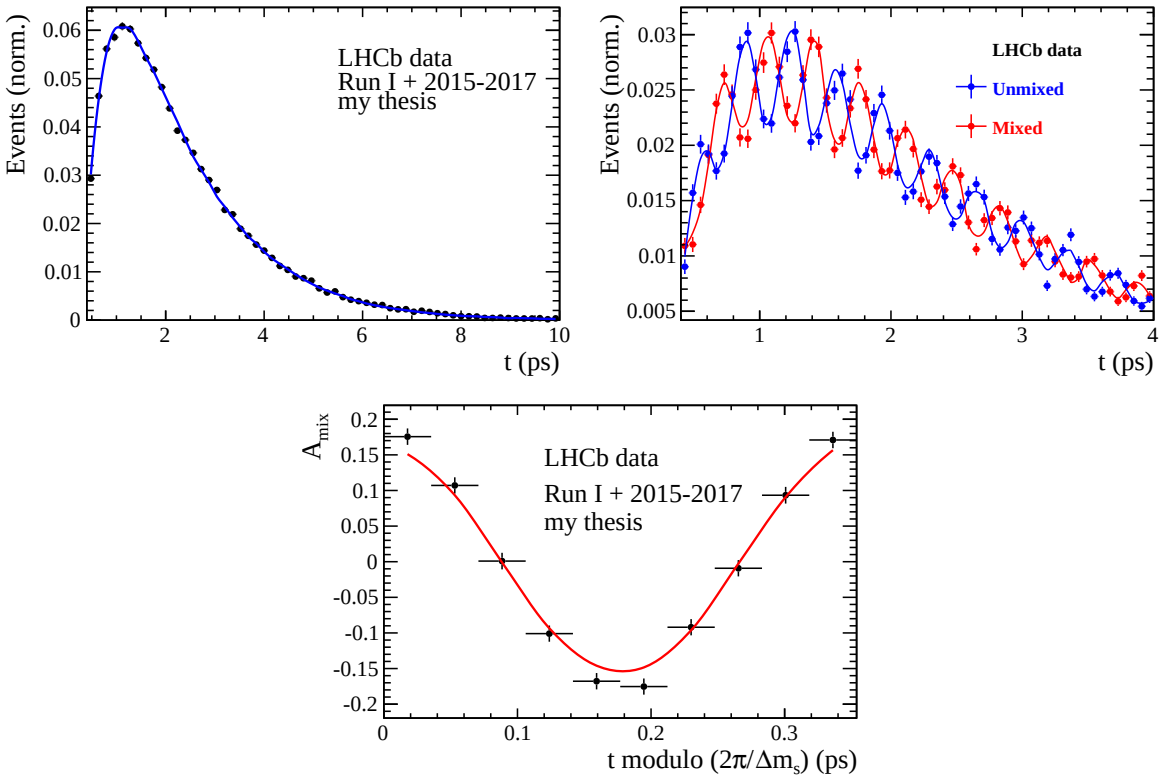

Figure 10.1.: Top-left: Flavor averaged decay time distribution of $B_s^0 \to D_s^- \pi^+ \pi^- \pi^+$ candidates. Top-right: Flavor tagged decay time distribution of mixed (red) and unmixed (blue) B_s^0 signal candidates. Bottom: Time-dependent asymmetry A_{mix} between mixed and unmixed B_s^0 candidates folded into one oscillation period. A fit discussed in the text is overlaid for every distribution.

where C, D_f ($D_{\bar{f}}$) and S ($S_{\bar{f}}$) are the CP-violating parameters and $\vec{\lambda}$ is the vector of fit parameters used as input. The fit is performed simultaneously, using the same physics parameters for all fit functions in the four disjoint data categories, while each fit function is convoluted with the respective resolution model determined in Chapter 8.1 and multiplied by the respective time-dependent efficiency found in Chapter 8.2. The calibration parameters for the flavor tagging, determined from the fit to $B_s^0 \to D_s^- \pi^+ \pi^- \pi^+$ data described above, are included in the fit using so-called Gaussian constraints, where for each parameter, a term is added to the likelihood function:

$$\ln(\mathcal{L}) \to \ln(\mathcal{L}) - \sum_{j=1}^{M} \frac{(\lambda_j - \lambda_{j,meas})^2}{2\sigma_{j,meas}^2}. \tag{10.5}$$

In Equation 10.5, M is the number of tagging parameters used for the fit, λ_j is the floated value of the tagging parameter j, $\lambda_{j,meas}$ is its measured central value and $\sigma_{j,meas}$

is its measured uncertainty, both determined from the fit to $B_s^0 \to D_s^- \pi^+ \pi^- \pi^+$ and shown in Table 10.1. This method ensures that the tagging parameters can vary within their uncertainty, accounting for small differences between the two decay modes and that the systematic uncertainty from the pre-determined tagging parameters is included in the statistical uncertainty of the fit to $B_s^0 \to D_s^- K^+ \pi^- \pi^+$ data.
The measured CP coefficients $C, D_f, D_{\bar{f}}, S_f$ and $S_{\bar{f}}$ extracted from the fit to the $B_s^0 \to D_s^- K^+ \pi^- \pi^+$ decay-time distribution are reported in Table 10.2 and the fit projection is shown in Figure 10.2.

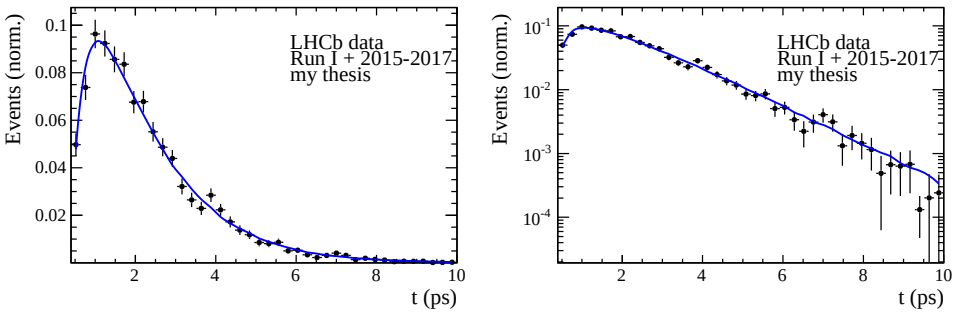

Figure 10.2.: Normalized decay-time distribution of $B_s^0 \to D_s^- K^+ \pi^- \pi^+$ signal candidates in (left) normal and (right) logarithmic scale, with the fit projection overlaid.

Table 10.2.: CP coefficients determined from a fit to the $B_s^0 \to D_s^- K^+ \pi^- \pi^+$ decay-time distribution. The uncertainties are statistical only.

Fit Parameter	Value
C	0.68 ± 0.12
D_f	0.01 ± 0.32
$D_{\bar{f}}$	0.38 ± 0.30
S_f	-0.14 ± 0.17
$S_{\bar{f}}$	-0.54 ± 0.17

10.3. Systematic Uncertainties

In this Section, possible sources of systematic uncertainties for the decay-time fit to the $B_s^0 \to D_s^- K^+ \pi^- \pi^+$ candidates are discussed. Each section covers one possible source and

the method used to estimate the arising uncertainty, while all uncertainties are shown in the respective sections and summarized in Table 10.3.

10.3.1. Validation of the fit procedure

The fit procedure is validated using pseudo-experiments. Each pseudo-experiment is generated with the same amount of signal events found in the full $B_s^0 \to D_s^- K^+\pi^-\pi^+$ data sample, using the model described in the previous section. Every pseudo-experiment is then fit with the model and pull distributions are formed for all CP coefficients, where every pull P of a parameter x is given as

$$P = \frac{x_{gen} - x_{fit}}{\Delta x}. \tag{10.6}$$

The pull distributions are shown in Figure 10.3, where a fit with a Gaussian function is overlaid for every distribution. Only small deviations from the expected mean, 0, and width, 1, are observed. Every width except the one for the distribution of $D_{\bar{f}}$ agrees with 1 within the statistical uncertainty of the respective Gaussian fit, while the width for the pull distribution of $D_{\bar{f}}$ still agrees on the 3σ level. All means except the one for S_f agree with 0 within the fit uncertainties, while the mean for the pull distribution of S_f still agrees on the 2σ level.

The mean of the respective distribution is taken as a systematic uncertainty of the fit parameter:

$$\begin{aligned}
\Delta(C)_{\text{fit-bias}} &= 0.06\sigma_{\text{stat}}, \\
\Delta(D_f)_{\text{fit-bias}} &= 0.02\sigma_{\text{stat}}, \\
\Delta(D_{\bar{f}})_{\text{fit-bias}} &= 0.04\sigma_{\text{stat}}, \\
\Delta(S_f)_{\text{fit-bias}} &= 0.01\sigma_{\text{stat}}, \\
\Delta(S_{\bar{f}})_{\text{fit-bias}} &= 0.07\sigma_{\text{stat}},
\end{aligned}$$

where the arising uncertainties are very small ($\mathcal{O}(1\%)$) compared to the statistical precision σ_{stat}.

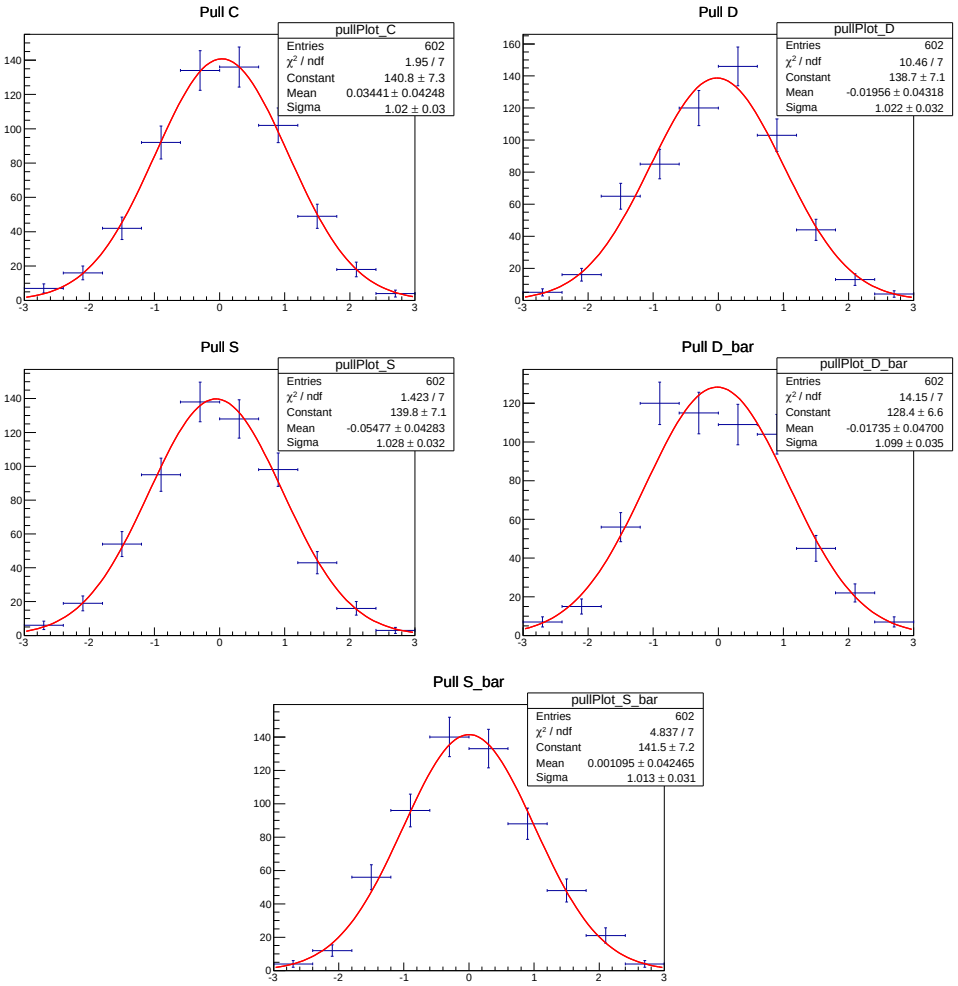

Figure 10.3.: Pull distributions from systematic studies for the time-dependent fit, done with 600 pseudo-experiments.

10.3.2. Subtraction of the residual background

The subtraction of the background left in the $B_s^0 \to D_s^- K^+ \pi^- \pi^+$ data sample after the full selection, using the sPlot method [71], relies on the correct description of the invariant B_s^0 mass distribution for signal and background. Since the choice of the models used to describe the signal and the various background components is not unique, alternative parametrizations are tested. Considering that the shapes used in the nominal fit model to describe the different signal and background contributions fit the $m(D_s^- h^+ \pi^- \pi^+)$ distributions well, as shown in Chapter 7, models that describe similar shapes while using a different parametrization are chosen to study the systematic uncertainty:

- For signal events: The Johnson's SU function [73] is replaced by the sum of two

Crystal Ball functions [75]. Opposite sides of the Crystal Ball functions are chosen to have exponential tails, making the sum of both be an asymmetric Gaussian function, similar to the Johnson's SU function.

- For the combinatorial background: The nominal second order polynomial is replaced by an exponential function. As additional model, the sum of a second order polynomial and an exponential function is tested.

- For the partially reconstructed background: A combination of the RooHILLdini and RooHORNsdini model [87] is used instead of the nominal model of three bifurcated Gaussian functions.
  The HORNSdini model is used to describe the $B_s^0 \to D_s^{-*}[\to D_s^-(\pi^0)]X_{s/d}$ decay, where the brackets around the π^0 indicate that it is missed in the reconstruction. The $D_s^{-*} \to D_s^-\pi^0$ decay is a Vector $\to$ Scalar-Scalar ($1^- \to 0^-0^-$) transition. Using the helicity of the D_s^-, one can demonstrate that this results in a double-peak structure in the reconstructed B_s^0 mass [88]. Therefore, the HORNSdini shape consists of a Gaussian-like double-peak structure:

$$HORNS(m_{B_s^0}) = \int_a^b dm_{B_s^0} \left(m_{B_s^0} - \frac{a+b}{2}\right)^2 \mathcal{DG}(m_{B_s^0}|\mu,\sigma,f_G) \left(\frac{1-\zeta}{b-a} m_{B_s^0} + \frac{b\zeta - a}{b-a}\right), \tag{10.7}$$

  where a and b are the kinematic endpoint of the distribution and ζ is the positive, real fraction of the two peak heights. Additionally, the shape is convoluted with a Gaussian-function to account for resolution effects. The HILLdini model parametrizes the invariant mass shape of $B_s^0 \to D_s^{-*}[\to D_s^-(\gamma)]X_{s/d}$ candidates, where the γ is not reconstructed. Contrary to the previously discussed process, the $D_s^{-*} \to D_s^-\gamma$ is a Vector $\to$ Scalar-Vector ($1^- \to 0^-1^-$) transition. From helicity conservation arguments, the expected shape in the mass distribution of B_s^0 candidates follows a parabolic curve without any peaking structure [88]. To accommodate for this shape, the HILLdini model consists of a parabolic curve between the kinematic endpoints a & b:

$$HILL(m_{B_s^0}) = \begin{cases} -(m_{B_s^0} - a)(m_{B_s^0} - b), & \text{for } a < m_{B_s^0} < b \\ 0, & otherwise. \end{cases} \tag{10.8}$$

  This shape is convoluted with the same Gaussian resolution function used for the

HORNSdini model.

- Mis-ID background: For this background, the nominal approach is to obtain the shape from a fit to a sample of $B_s^0 \to D_s^- \pi^+ \pi^- \pi^+$ or $B_s^0 \to D_s^{-*} \pi^+ \pi^- \pi^+$ decays, where the mass hypothesis of the π^+ with the higher misidentification probability is flipped to a kaon (see Chapter 7.2). Two alternative approaches are considered: flip the mass hypothesis of the π^+ candidate with the lower probability of being misidentified or randomly flip the mass hypothesis of a π^+ candidate. In both cases, the shape is taken from a fit of the nominal model to the respective alternative distribution.
  To evaluate the possible source of systematic uncertainty arising from the fixed yields of the mis-ID backgrounds, the yields are fixed to zero or doubled with respect to the estimated value used in the nominal fit.

In total 15 different combinations of the modifications discussed above are tested for the fit to the $B_s^0 \to D_s^- K^+ \pi^- \pi^+$ mass distribution. For each case, new signal sWeights are calculated and the sFit to data is repeated. The sample variance of the obtained differences to the nominal fit value is used as systematic uncertainty due to the background subtraction:

$$\begin{aligned}
\Delta(C)_{\text{background}} &= 0.06\sigma_{\text{stat}}, \\
\Delta(D_f)_{\text{background}} &= 0.10\sigma_{\text{stat}}, \\
\Delta(D_{\bar{f}})_{\text{background}} &= 0.13\sigma_{\text{stat}}, \\
\Delta(S_f)_{\text{background}} &= 0.06\sigma_{\text{stat}}, \\
\Delta(S_{\bar{f}})_{\text{background}} &= 0.03\sigma_{\text{stat}}.
\end{aligned}$$

The systematic uncertainties arising from the subtraction of the residual background are found to be small ($\mathcal{O}(10\%)$) relative to the statistical precision σ_{stat}.

10.3.3. Decay-time acceptance

The description of the decay-time efficiency $\epsilon(t)$ is a possible sources of systematic uncertainty. To evaluate this uncertainty, pseudo-experiments are used.
For every pseudo-experiment, a decay-time distribution of B_s^0 candidates is generated with the same amount of signal events found in the full $B_s^0 \to D_s^- K^+ \pi^- \pi^+$ sample, using

the nominal fit PDF shown in Equation 10.1, with the knot positions and spline coefficients describing the decay-time acceptance, determined in Chapter 8.2. Each generated B_s^0 decay-time distribution of the pseudo-experiments is fitted twice, once with the same PDF used to generate the distribution, and once with a PDF where the value of one of the spline coefficients is randomized. To simplify the randomization of the second fit model, a Cholesky decomposition [89] is used to decorrelate the (a priori) correlated spline coefficients v_i. For this technique, the covariance matrix of the spline coefficients $\mathrm{cov}(v_i, v_j)$, obtained from the decay-time fits discussed in Chapter 8.2, is used.
A pull distribution is calculated for every CP parameter from the difference between the obtained value of the respective CP parameter from the fit, performed using the generated time-acceptance $\epsilon(t)$, and the fit using the shifted configuration $\epsilon^{'}(t)$, in which one spline coefficient is randomized. The pull is obtained by dividing this difference by the statistical uncertainty of the nominal fit. The shift of the mean of each pull distribution with respect to zero, as well as the width of this distribution, are added in quadrature to evaluate the systematic uncertainty on a given CP parameter, arising from the variation of the respective spline coefficient. Here, the width is added to the systematic uncertainty because the pull distributions are obtained from two fits to the same data sample, therefore the width should vanish for identically performing fits.
Since the spline coefficients are decorrelated, the systematic uncertainties on the CP parameters, arising from the variation of different spline coefficients, can be added in quadrature to obtain the overall uncertainty on the respective parameter:

$$\begin{aligned}
\Delta(C)_{\text{acceptance}} &= 0.04\sigma_{\text{stat}}, \\
\Delta(D_f)_{\text{acceptance}} &= 0.22\sigma_{\text{stat}}, \\
\Delta(D_{\bar{f}})_{\text{acceptance}} &= 0.22\sigma_{\text{stat}}, \\
\Delta(S_f)_{\text{acceptance}} &= 0.02\sigma_{\text{stat}}, \\
\Delta(S_{\bar{f}})_{\text{acceptance}} &= 0.02\sigma_{\text{stat}}.
\end{aligned}$$

The systematic uncertainty on C, S_f and $S_{\bar{f}}$, arising from the time-acceptance correction, is almost negligible with respect to the statistical uncertainty σ_{stat}. For the CP parameters D_f and $D_{\bar{f}}$, which are sensitive to small decay times, the systematic uncertainty is sizable, although the statistical error still dominates. This is caused by the strong variation of $\epsilon(t)$ for small decay times, where a precise description of the rising time-dependent efficiency is needed to determine D_f and $D_{\bar{f}}$ correctly.

10.3.4. Decay-time resolution and flavor tagging

Systematic uncertainties can arise from the model-dependent scaling of the decay-time error σ_t and the closely related determination of the parameters for the tagging calibration. Due to the high correlation between them, both systematic uncertainties need to be estimated simultaneously. First, an alternative scaling relation for the decay-time error is determined. Then, the relation is used in the fit to $B_s^0 \to D_s^-\pi^+\pi^-\pi^+$ data to determine new tagging calibration parameters.
To study systematic effects originating from the scaling, the determination of the effective resolution described in Chapter 8.1 is repeated using two different approaches which either slightly overestimate or underestimate the decay-time resolution:

- The nominal double Gaussian fit model is used for the decay-time distributions of fake B_s^0 candidates, but only the width of the core Gaussian-function, containing roughly 75% of events, is considered to represent the time resolution in the respective bin. Therefore, the resolution is slightly underestimated in this case.
- A single Gaussian fit model is used for the decay-time distributions of fake B_s^0 candidates in a wide range of $[-3\sigma_t : 1.5\sigma_t]$. Due to the tails of the distribution, which broaden the width of the Gaussian function, this method slightly overestimates the decay-time resolution.

For both cases, a new scaling function is derived using the same procedure described in Chapter 8.1. The alternative scaling relations are:

$$\sigma_{eff}^{core-Gauss}(\sigma_t) = (4.9 \pm 2.0)\,\text{fs} + (0.821 \pm 0.050)\,\sigma_t, \tag{10.9}$$

$$\sigma_{eff}^{single-Gauss}(\sigma_t) = (8.3 \pm 1.5)\,\text{fs} + (0.997 \pm 0.037)\,\sigma_t. \tag{10.10}$$

Figure 10.4 shows the comparison between the two alternative and the nominal scaling functions.

Two new sets of tagging parameters are obtained using each new scaling relation as input to the time-dependent fit to $B_s^0 \to D_s^-\pi^+\pi^-\pi^+$ signal candidates, described in Chapter 10.1. The new set of parameters is then used, together with the respective scaling function, in the fit to $B_s^0 \to D_s^-K^+\pi^-\pi^+$ signal data. The biggest change in the fitted central value for each CP observable is chosen as the respective systematic uncertainty, which is found to be:

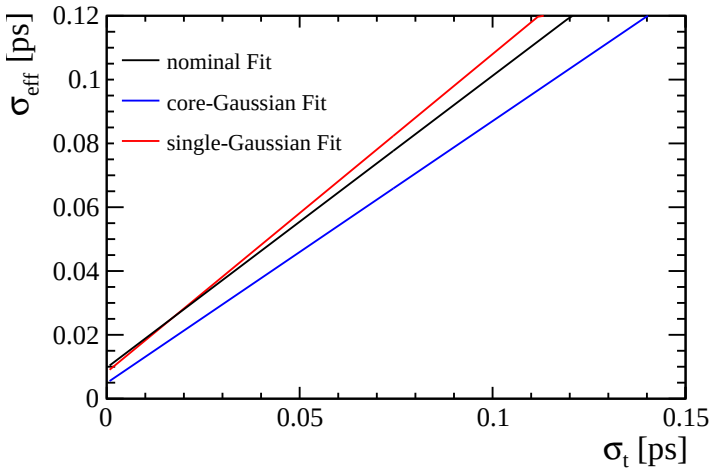

Figure 10.4.: The measured resolution scaling function of the per-event decay-time error estimate σ_t for fake B_s candidates (Run II data) for (black line) the nominal scaling, (blue line) only using the width of the narrow Gaussian-function of the double Gaussian fit model or (red line) when determining the resolution using a single Gaussian model.

$$
\begin{aligned}
\Delta(C)_{\text{resolution}} &= 0.15\sigma_{\text{stat}}, \\
\Delta(D_f)_{\text{resolution}} &= 0.01, \\
\Delta(D_{\bar{f}})_{\text{resolution}} &= 0.02\sigma_{\text{stat}}, \\
\Delta(S_f)_{\text{resolution}} &= 0.07\sigma_{\text{stat}}, \\
\Delta(S_{\bar{f}})_{\text{resolution}} &= 0.05\sigma_{\text{stat}}.
\end{aligned}
$$

The systematic uncertainties arising from the flavor tagging and the parametrization of the decay-time resolution are small ($\mathcal{O}(1\%)$ - $\mathcal{O}(10\%)$) compared to the statistical precision σ_{stat}.

10.3.5. Asymmetries and mixing frequency

The B_s^0 production and kaon detection asymmetry, discussed in Chapter 9.3, as well as the mixing frequency Δm_s, are used as input for the time-dependent fit to $B_s^0 \to D_s^- K^+\pi^-\pi^+$ signal candidates. Due to the fact that they are only known to a finite precision, a systematic uncertainty arising from the limited knowledge of these inputs needs to be considered. These uncertainties are estimated by means of a study of pseudo-experiments, similar to the procedure performed for the decay-time acceptance studies

described above. The respective means and widths of the pull distributions for the CP observables are a measure of the shift of these observables due to the systematic uncertainty arising from the asymmetries and the mixing frequency. Therefore, they are summed in quadrature to arrive at the quoted systematic uncertainty assigned for this source. The uncertainties arising from the production and detection asymmetries are found to be very small,

$$\begin{aligned}
\Delta(C)_{\text{asymmetries}} &= 0.02\sigma_{\text{stat}}, \\
\Delta(D_f)_{\text{asymmetries}} &= 0.04, \\
\Delta(D_{\bar{f}})_{\text{asymmetries}} &= 0.04\sigma_{\text{stat}}, \\
\Delta(S_f)_{\text{asymmetries}} &= 0.03\sigma_{\text{stat}}, \\
\Delta(S_{\bar{f}})_{\text{asymmetries}} &= 0.02\sigma_{\text{stat}},
\end{aligned}$$

where no uncertainty is larger than 4% of the statistical error. The uncertainties from the limited knowledge of the mixing frequency Δm_s are:

$$\begin{aligned}
\Delta(C)_{\Delta m_s} &= 0.06\sigma_{\text{stat}}, \\
\Delta(D_f)_{\Delta m_s} &= 0.02, \\
\Delta(D_{\bar{f}})_{\Delta m_s} &= 0.02\sigma_{\text{stat}}, \\
\Delta(S_f)_{\Delta m_s} &= 0.21\sigma_{\text{stat}}, \\
\Delta(S_{\bar{f}})_{\Delta m_s} &= 0.22\sigma_{\text{stat}}.
\end{aligned}$$

A significant systematic uncertainty on the S_f and $S_{\bar{f}}$ is found, originating from the fact that those parameters are appearing in the term sensitive to $\sin(\Delta m_s t)$ in the decay rate, used to describe the $B_s^0 \to D_s^- K^+\pi^-\pi^+$ decay. However, the size of the systematic uncertainty on S_f and $S_{\bar{f}}$ from the limited knowledge of Δm_s is still only 22% of the statistical error.

10.3.6. Multiple candidates

A small fraction of 1.5% for $B_s^0 \to D_s^-\pi^+\pi^-\pi^+$ and 1.6% for $B_s^0 \to D_s^- K^+\pi^-\pi^+$ events have multiple signal candidates, where more than one PV that is associated with a B_s^0 candidate is found. The nominal fit result is obtained keeping all candidates, while

a systematic uncertainty is evaluated by repeating the time-dependent fit, randomly keeping only one candidate for events where multiple ones are found. No shift in the central values of the CP observables is found, therefore no additional uncertainty arising from the contribution of multiple candidates is assumed.

10.3.7. Uncertainty on LHCb length scale

An uncertainty on the measured flight length of B_s^0 mesons arises from the precision with which the position of the VELO modules, as well as the overall length of the VELO itself is known [90]. This uncertainty on the LHCb length scale translates directly to a systematic uncertainty on Δm_s. The upper bound for this uncertainty is 0.02% [91], which is taken as systematic uncertainty on the mixing frequency due to the knowledge of the LHCb length scale.

10.3.8. Summary of systematic uncertainties

All systematic uncertainties on the physics parameters of the $B_s^0 \to D_s^- K^+\pi^-\pi^+$ decay are summarized in Table 10.3. The total uncertainty is formed by summing all uncertainties in quadrature.
The systematic uncertainty on the CP observable D_f and $D_{\bar{f}}$ is dominated by the knowledge of the decay-time acceptance due to their correlation with small decay times. For this region of the data sample, the correct description of the rising time-dependent efficiency $\epsilon(t)$ is paramount. The systematic uncertainties on S_f and $S_{\bar{f}}$ are dominated by the uncertainty on Δm_s, as they are sensitive to the term proportional to $\sin(\Delta m_s t)$. The parameter C is most robust against systematic uncertainties.

Table 10.3.: Systematic uncertainties on the fit parameters of the time-dependent fit to $B_s^0 \to D_s^- K^+\pi^-\pi^+$ signal data in units of statistical standard deviations.

Fit Parameter	Fit bias	Acceptance	Resolution	Δm_s	Asymmetries	Background	Total
C	0.06	0.04	0.15	0.06	0.02	0.06	0.19
D_f	0.02	0.22	0.01	0.02	0.04	0.10	0.25
$D_{\bar{f}}$	0.04	0.22	0.02	0.02	0.04	0.13	0.26
S_f	0.01	0.02	0.07	0.21	0.03	0.06	0.23
$S_{\bar{f}}$	0.07	0.02	0.05	0.22	0.02	0.03	0.24

The central values of the CP-violating parameter, as well as the statistical and system-

atical uncertainties, are summarized in Table 10.4. Considering that no CP violation would occur if $D_f = D_{\bar{f}} = S_f = S_{\bar{f}} = 0$, the combined significance with which CP violation is measured in the presented analysis is 3.4σ.

Table 10.4.: CP parameters determined from the fit to the $B_s^0 \to D_s^- K^+\pi^-\pi^+$ decay-time distribution. The uncertainties are statistical and systematic, respectively.

Fit Parameter	Value
C	0.68 ± 0.12 ± 0.02
D_f	0.01 ± 0.32 ± 0.08
$D_{\bar{f}}$	0.38 ± 0.30 ± 0.08
S_f	-0.14 ± 0.17 ± 0.04
$S_{\bar{f}}$	-0.54 ± 0.17 ± 0.04

10.4. Determination of γ, δ, r and κ

The CP parameters obtained from the phase-space integrated, time-dependent fit to $B_s^0 \to D_s^- K^+\pi^-\pi^+$ data, shown in Table 10.4, are used to determine the CKM angle γ, as well as the strong phase difference δ, the ratio of contributing $b \to c$ and $b \to u$ amplitudes r and the hadronic coherence factor κ from Equations 3.61, 3.62 and 3.63. A dedicated software tool described in [92] is used to determine γ by maximizing the likelihood

$$\mathcal{L}(\vec{\alpha}) = \exp\left(-\frac{1}{2}[\vec{A}(\vec{\alpha}) - \vec{A}_{obs}]^T \sigma^{-1} [\vec{A}(\vec{\alpha}) - \vec{A}_{obs}]\right), \tag{10.11}$$

where $\vec{\alpha} = (\gamma, \beta_s, r, \delta, \kappa)^T$ is the vector of the physics parameters, $\vec{A}$ is the vector of observables expressed through Equation 3.61-3.63, $\vec{A}_{obs}$ is the vector of the measured CP observables and σ is the full covariance matrix of the time-dependent fit, including statistical and systematic uncertainties. The contributing sources of systematic uncertainties are discussed in Chapter 10.3. Confidence intervals are computed using a frequentest approach following [93]. The CP observables are explicitly dependent on $\gamma - 2\beta_s$, therefore the B_s^0 mixing phase β_s is needed as input to measure γ in the presented analysis. This input is taken from LHCb measurements using $B_s^0 \to J\Psi\pi^+\pi^-$ and $B_s^0 \to J\Psi K^+K^-$ decays [94], where the weak phase is determined as $\phi_s = -0.010 \pm 0.039\ rad$ and $\phi_s = -2\beta_s$

is assumed.

The obtained central values for γ, δ, κ and r are given in Table 10.5.

Table 10.5.: Physics parameters determined from the CP observables that are measured in the phase-space integrated, time-dependent fit. For the quoted uncertainties, statistical and systematic contributions are combined.

parameter	value
r	$0.415^{+0.096}_{-0.107}$
κ	$0.63^{+0.26}_{-0.20}$
$\delta\,[^\circ]$	39^{+18}_{-20}
$\gamma\,[^\circ]$	65^{+27}_{-20}

The likelihood profiles for all parameters are shown in Figure 10.5, where for convenience each profile is given as the difference between unity and the confidence-level $(1 - CL)$, such that the distributions peak at 1 for the most likely value. Figure 10.6 presents the two-dimensional profile likelihood contours of γ against r and δ.

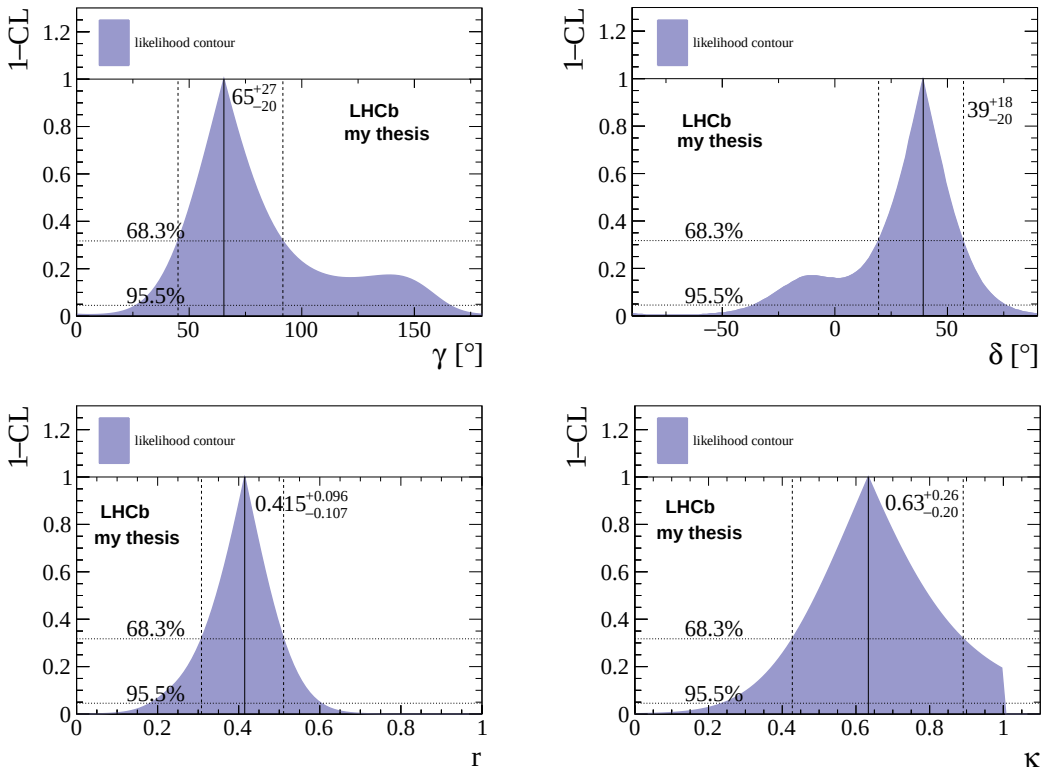

Figure 10.5.: Likelihood profiles of (top-left) γ, (top-right) δ, (bottom-left) r and (bottom-right) κ, in units of $1 - CL$, determined from the CP observables that are measured in the phase-space integrated, time-dependent fit. The 1σ (68.3%) and 2σ (95.5%) confidence-level intervals are indicated by vertical, dotted lines.

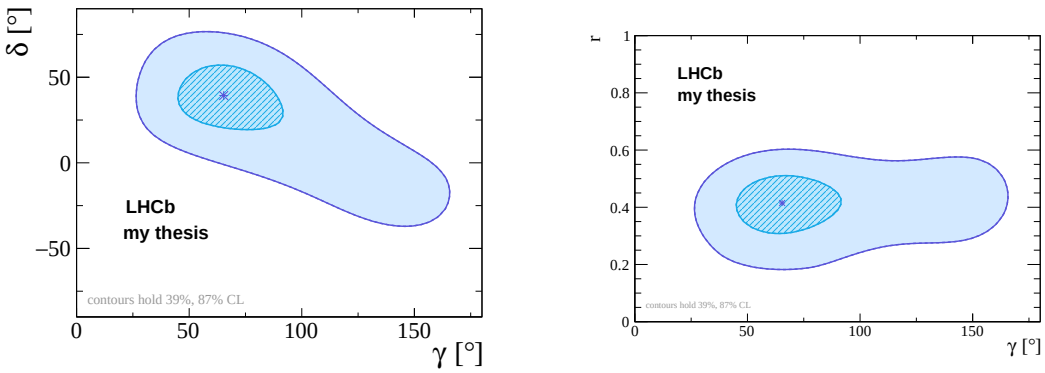

Figure 10.6.: Two-dimensional likelihood contours of (left) γ versus δ and (right) γ versus r, determined from the CP observables that are measured in the phase-space integrated, time-dependent fit. The central value for the respective parameters is marked by a star, while the 39% and 87% confidence-level contours are indicated by the (39%) inner and (87%) outer, filled areas.

Chapter 11

Study of a model-dependent determination of the CKM angle γ

In this Chapter, the precision of a model-dependent determination of the CKM angle γ, using a time-dependent amplitude fit to the $B_s^0 \to D_s^- K^+ \pi^- \pi^+$ signal candidates, is discussed. Major contributions to this fit were made by the second doctoral student of the analysis group, with additional contributions from the author. Therefore, the full procedure is briefly summarized in this Chapter and references are given to the internal note [5] and the peer-reviewed paper [6], where the time-dependent amplitude fit is presented in detail.
The PDF used for the full fit is defined similarly to the one shown in Equation 10.1, with an additional dependence on the phase-space $\vec{x}$ of $B_s^0 \to D_s^- K^+ \pi^- \pi^+$ decays, $\mathcal{P}(\vec{x}, t_i | \delta t_i, q_{OS}^i, \eta_{OS}^i, q_{SS}^i, \eta_{SS}^i)$. It is parametrized by the time and phase-space dependent differential decay rate introduced in Equation 3.56, including the dilution effects caused by the limited knowledge of the initial flavor of the beauty meson and taking the correction functions $\epsilon(t)$, $\mathcal{R}(t_i - t_i^{'}, \delta t_i)$ for the decay-time acceptance and resolution, determined in Chapter 8, into account. In the following, the selection of the signal model, consisting of the amplitudes

$$\mathcal{A}_f^{b\to c}(\vec{x}) = \mathcal{A}_f^c(\vec{x}) = \sum_j a_j^c \, \mathcal{A}_j(\vec{x}),$$
$$\mathcal{A}_f^{b\to u}(\vec{x}) = \mathcal{A}_f^u(\vec{x}) = \sum_j a_j^u \, \mathcal{A}_j(\vec{x}),$$

that describe the different intermediate hadronic states, is summarized and the results of the sensitivity studies for a time-dependent amplitude fit are presented.

11.1. Construction of the signal amplitude model

A multitude of light meson resonances is expected to contribute as intermediate states to the $B_s^0 \to D_s^- K^+\pi^-\pi^+$ decay, e.g. the process

$$B_s^0 \to D_s^-[K_1^+(1270) \to \pi^+(K^{*0}(892) \to K^+\pi^-)], \tag{11.1}$$

with intermediate $K_1^+(1270)$ and $K^{*0}(892)$ mesons. Apart from states like the one shown in Equation 11.1, several broad and overlapping interfering resonances contribute to the decay channel. In total, there are roughly 30 possible intermediate contributions [5] from which the amplitude model can be built. Adding all intermediate states, which are listed in Appendix E, to the fit model would result in a very complex fit that could not converge. To construct a suitable amplitude model with limited complexity, a fit to the time-integrated, flavor averaged phase-space distribution of the background subtracted $B_s^0 \to D_s^- K^+\pi^-\pi^+$ candidates is performed. In this case, the sum of amplitudes can be formed to give a single, effective total amplitude:

$$\int \mathcal{P}(\vec{x}, t|\delta t, q_{OS}, \eta_{OS}, q_{SS}, \eta_{SS}) dt\ dq_t\ dq_f \propto \mathcal{A}_f^{eff}(\vec{x}) = \sum_i a_i^{eff} A_i(\vec{x}). \tag{11.2}$$

Here, the index i numerates the different contributing amplitudes, while $\mathcal{A}_f^{eff}(\vec{x})$ describes the incoherent superposition of the $b \to u$ and $b \to c$ amplitudes,

$$|\mathcal{A}_f^{eff}(\vec{x})|^2 = |\mathcal{A}_f^c(\vec{x})|^2 + |\mathcal{A}_f^u(\vec{x})|^2. \tag{11.3}$$

To select the final amplitude model, the LASSO method [95, 96] is chosen. This approach starts by including the complete set of possible amplitudes (shown in Appendix E) contributing to the $B_s^0 \to D_s^- K^+\pi^-\pi^+$ decay, while adding a penalty term to the likelihood function for each amplitude,

$$\ln(\mathcal{L}) \to \ln(\mathcal{L}) - \sum_i \sqrt{\int |a_i^{eff} A_i(\vec{x})|^2 \, \mathrm{d}\Phi_4}. \tag{11.4}$$

Each penalty term shrinks the coefficient a_i^{eff} of amplitude i towards zero. Following this approach, a balance is struck between the complexity of the fit model and the relative significance of any additional amplitude, leaving the final model with a few, dominating contributions to the phase-space spectrum of $B_s^0 \to D_s^- K^+\pi^-\pi^+$ decays. The selected

amplitudes, as well as their fit fractions defined as

$$F_i \equiv \frac{\int \left| a_i^{eff}\, A_i(\vec{x}) \right|^2 \mathrm{d}\Phi_4}{\int \left| \mathcal{A}_f^{eff}(\vec{x}) \right|^2 \mathrm{d}\Phi_4}, \tag{11.5}$$

are shown in Table 11.1. Although all fit fractions of the different contributions add up to 100% within the statistical uncertainty, it should be noted that this is not an intrinsic requirement on the measurement, since constructive or destructive interference between the different hadronic resonances could occur and lead to combined fit fractions that are larger or smaller than 1. Figure 11.1 shows the projections of the time-integrated, flavour averaged amplitude fit onto the five invariant mass combination chosen to represent the phase-space of $B_s^0 \to D_s^- K^+\pi^-\pi^+$ decays.

Table 11.1.: Fit fractions of the amplitudes selected by the LASSO approach in the fit to the decay-time integrated, flavor-averaged phase space distribution of $B_s^0 \to D_s^- K^+\pi^-\pi^+$ candidates. Taken from [5].

Process	Fraction [%]
$B_s \to K(1)(1270)^+(\to K^*(892)^0(\to K^+\,\pi^-)\,\pi^+)\,D_s^-$	8.56 ± 1.43
$B_s \to K(1)(1400)^+(\to K^*(892)^0(\to K^+\,\pi^-)\,\pi^+)\,D_s^-$	43.72 ± 2.80
$B_s \to K(1460)^+(\to K^*(892)^0(\to K^+\,\pi^-)\,\pi^+)\,D_s^-$	3.25 ± 0.69
$B_s \to K^*(1410)^+(\to K^*(892)^0(\to K^+\,\pi^-)\,\pi^+)\,D_s^-$	15.33 ± 1.13
$B_s \to (D_s^-\,\pi^+)_P\,K^*(892)^0(\to K^+\,\pi^-)$	4.63 ± 0.69
$B_s \to K^*(1410)^+(\to \rho(770)^0(\to \pi^+\,\pi^-)\,K^+)\,D_s^-$	5.58 ± 0.62
$B_s \to (D_s^-\,K^+)_P\,\rho(770)^0(\to \pi^+\,\pi^-)$	1.49 ± 0.40
$B_s \to K(1)(1270)^+(\to K(0)^*(1430)^0(\to K^+\,\pi^-)\,\pi^+)\,D_s^-$	4.72 ± 0.54
$B_s \to K(1)(1270)^+(\to \rho(770)^0(\to \pi^+\,\pi^-)\,K^+)\,D_s^-$	14.20 ± 1.56
Sum	101.47 ± 3.86

11.2. Results of the sensitivity study

After the construction of the amplitude model, the full time-dependent amplitude PDF built from the decay rate given in Equation 3.56, with the amplitudes listed in Table 11.1, is fit to the spectrum of background subtracted and flavor tagged $B_s^0 \to D_s^- K^+\pi^-\pi^+$ candidates to study the achievable sensitivity to the CKM angle γ, as well as the ratio of $b \to c$ and $b \to u$ amplitudes r and the strong phase difference δ. The fit fractions for $b \to u$ and $b \to c$ quark transitions are separately normalized,

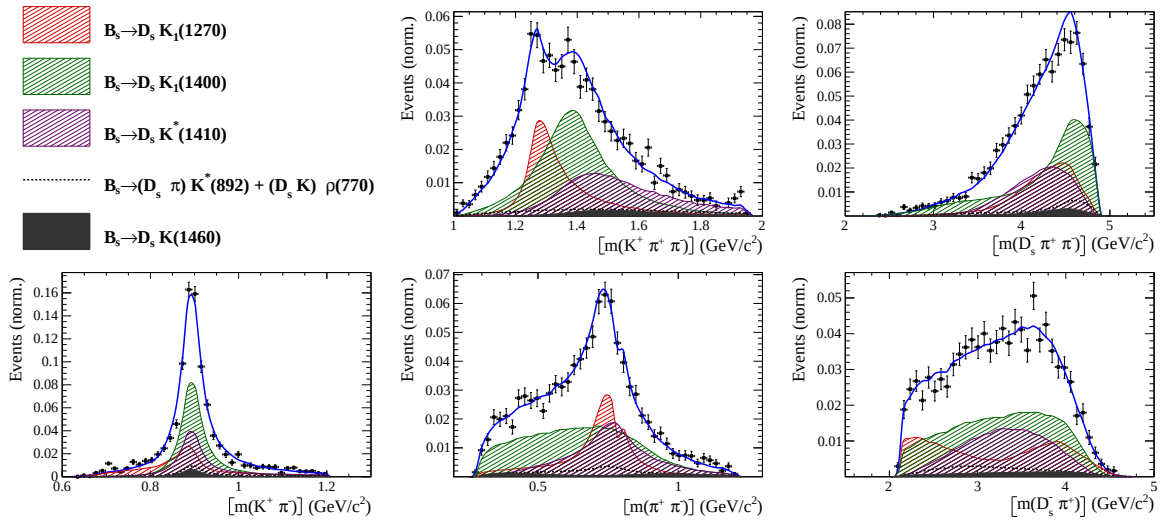

Figure 11.1.: Projections of the amplitude fit result to the time-integrated and flavor-averaged phase-space distribution of $B_s^0 \to D_s^- K^+\pi^-\pi^+$ decays. Taken from [5].

$$F_i^{c,u} \equiv \frac{\int \left|a_i^{c,u}\, A_i(\vec{x})\right|^2 \mathrm{d}\Phi_4}{\int \left|\mathcal{A}_f^{c,u}(\vec{x})\right|^2 \mathrm{d}\Phi_4}, \tag{11.6}$$

with the phase space element $\mathrm{d}\Phi_4$ which is introduced in Chapter 3.3. The purely time-dependent part of the fit model is handled in the same way as for the phase-space integrated fit, described in Chapter 10.

Table 11.2 summarizes the estimated sensitivities to $(\gamma - 2\beta_s)$, δ and r, together with the uncertainties that arise from the statistical precision of the fit, as well as systematic uncertainties from the time-dependent part of the fit model (discussed in Chapter 10.3) and uncertainties that arise from the explicit choice of the amplitude model (discussed in [5, 6]).

Table 11.2.: Estimated sensitivity on the observables of the time-dependent amplitude fit to $B_s^0 \to D_s^- K^+\pi^-\pi^+$ data. First quoted uncertainties are statistical, while the second arise from systematic sources. The third uncertainty arises from systematic studies with alternative models, extensively discussed in [5].

Fit parameter	sensitivity
r	xx.xx $\pm$ 0.04 $\pm$ 0.02 $\pm$ 0.04
δ [°]	xx.xx $\pm$ 16.1 $\pm$ 6.6 $\pm$ 4.9
$\gamma - 2\beta_s$ [°]	xx.xx $\pm$ 16.1 $\pm$ 9.6 $\pm$ 5.0

Adding all uncertainties in quadrature and including the uncertainty on the B_s^0 mixing phase, $\Delta(\beta_s) = 2.0°$ [94], the estimated overall precision on the CKM angle γ from this

fit is $\Delta(\gamma) = 19.8°$. At the time of writing, further studies are performed to ensure the consistency and stability of this fit, in order to publish the fit results for γ, δ and r in a dedicated paper [6].

Chapter 12

Summary

This thesis presents the first time-dependent measurement of CP violation and the determination of the CKM angle γ using $B_s^0 \to D_s^- K^+\pi^-\pi^+$ decays. A dataset corresponding to 6.7 fb^{-1}, collected by the LHCb experiment during the first two runs of the LHC, is used to perform a time-dependent analysis of the $B_s^0 \to D_s^-\pi^+\pi^-\pi^+$ and $B_s^0 \to D_s^- K^+\pi^-\pi^+$ decay channels. An unbinned maximum likelihood fit to the decay-time distribution of B_s^0 signal candidates is used to extract the CP parameters C, D_f and S_f from $B_s^0 \to D_s^- K^+\pi^-\pi^+$ decays. They are measured to be:

$$\begin{aligned} C &= 0.68 \pm 0.12 \ \pm \ 0.02, \\ D_f &= 0.01 \pm 0.32 \ \pm \ 0.08, \\ D_{\bar{f}} &= 0.38 \pm 0.30 \ \pm \ 0.08, \\ S_f &= -0.14 \pm 0.17 \ \pm \ 0.04, \\ S_{\bar{f}} &= -0.54 \pm 0.17 \ \pm \ 0.04, \end{aligned}$$

where the uncertainties are statistical and systematic, respectively. This result corresponds to 3.4σ evidence of CP violation in the interference between decay and decay after mixing in this channel. The obtained CP-violating parameters are used to determine the CKM angle γ, which is found to be:

$$\gamma = (65^{+27}_{-20})^\circ,$$

where the uncertainty contains both statistical and systematic contributions. The obtained value of γ agrees with the world average, $\gamma_{\text{avg}} = (73.5^{+4.2}_{-5.1})^\circ$ [77], within its uncertainties. Possible sources of systematic uncertainties contributing to the determination of the CP parameters and γ are evaluated, however, statistical uncertainties due

to the rare occurrence of the $B_s^0 \to D_s^- K^+\pi^-\pi^+$ decay are dominating the result.
The rich spectrum of intermediate states and resonances contributing to the $B_s^0 \to D_s^-(\to h^-h^+h^-)X_s^+(\to K^+\pi^-\pi^+)$ decay is explored by means of an amplitude analysis, which finds the excited $K_1(1270)$, $K_1(1400)$ and $K^*(1410)$ kaon states to dominantly contribute to the phase-space of this decay. A sensitivity study is presented, which demonstrates the first prospect of measuring γ by means of a time-dependent amplitude analysis, making use of the full information of the phase-space and avoiding a dilution of the γ measurement by explicitly describing the contributing intermediate hadronic resonances of the $B_s^0 \to D_s^- K^+\pi^-\pi^+$ decay.
In order to accomplish a combination of γ measurements with an uncertainty on the 1°-level, as well as to further the spectrum of γ analysis from different B mesons and with different techniques, more time-dependent measurements of this CKM angle are paramount. So far, the presented measurement represents the second time-dependent determination of γ, where an analysis of the $B_s^0 \to D_s^- K^+$ decay [4] provides the only other measurement. The next Run of the LHC, as well as the start of the BELLE 2 experiment, will provide more data of neutral B decays, which will further improve the still statistically limited measurement of CP violation and γ in $B_s^0 \to D_s^- K^+\pi^-\pi^+$ decays. Utilizing the time-dependent amplitude formalism, briefly discussed in this thesis, will enable analysts to extract γ with high precision from more and more challenging final states, with rich intermediate hadronic structure.
With further improvements on the precision of γ measurements, a powerful benchmark for consistency tests of the flavor sector of the Standard Model can be reached.

Appendix A

Selection requirements

A.1. Trigger requirements

Table A.1 summarizes the trigger requirements imposed by the HLT1 line used in this analysis for data taken during Run I. At least one of the six decay particles must pass the listed requirements in order for the event to be stored for further analysis. For Run II, this trigger line was updated and uses a multivariate classifier which takes the variables listed in Table A.1 as input, rather than directly cutting on them.

The HLT2 2, 3 and 4-body topological lines use a Boosted Decision Tree based on the b-hadron p_t, its flight distance χ^2 from the nearest PV and the sum of the B_s^0 and D_s^- vertex χ^2 divided by the sum of their number of degrees of freedom. Table A.2 summarizes the cuts applied by the inclusive ϕ trigger, which requires that a $\phi \to K^+K^-$ candidate can be formed out of two tracks present in the event.

A.2. Distributions after physical background vetoes

The distributions in Figure A.1, A.2, A.3 and A.4 illustrate the effects of the physical background vetoes, discussed in Chapter 6.2.2. For the shown distribution of the invariant mass of either the D_s^- or the B_s^0 candidate, the respective particle hypothesis is changed to the background hypothesis and the mass is recalculated using the four dimensional momentum vectors of each particle. The distributions are shown before and after the veto requirement is applied to visualize its effect.

Table A.1.: Summary of the cuts applied by the Hlt1TrackAllL0 trigger for Run I. At least one of the six decay particles must pass this requirements, in order for the event to be accepted.

Quantity	Hlt1TrackAllL0 requirement
Track IP [mm]	> 0.1
Track IP χ^2	> 16
Track χ^2/nDoF	< 2.5
Track p_t	$> 1.7\ GeV$
Track **p**	$> 10\ GeV$
Number VELO hits/track	> 9
Number missed VELO hits/track	< 3
Number OT+IT $\times$ 2 hits/track	> 16

Table A.2.: Summary of the cuts applied by the Hlt2 inclusive ϕ trigger. A $\phi \to K^+K^-$ candidate, formed by two tracks in the event, must pass this requirements in order for the event to be accepted.

Quantity	Hlt2IncPhi requirement
ϕ mass	$m_\phi \pm 12\ MeV$ of PDG value
ϕ p_t	$> 2.5\ GeV$
ϕ vertex χ^2/nDoF	< 20
ϕ IP χ^2 to any PV	> 5

A.3. Distributions of the input variables for the multivariate analysis

Figures A.5-A.8 show the distributions of all signal and background input variables for the Run I and Run II data-taking period. The signal distributions, obtained from pre-selected $B_s^0 \to D_s^-\pi^+\pi^-\pi^+$ candidates, are shown in blue while the background distributions, obtained from the upper mass sideband of $B_s^0 \to D_s^-K^+\pi^-\pi^+$ and $B_s^0 \to D_s^-\pi^+\pi^-\pi^+$ data, are depicted in red.

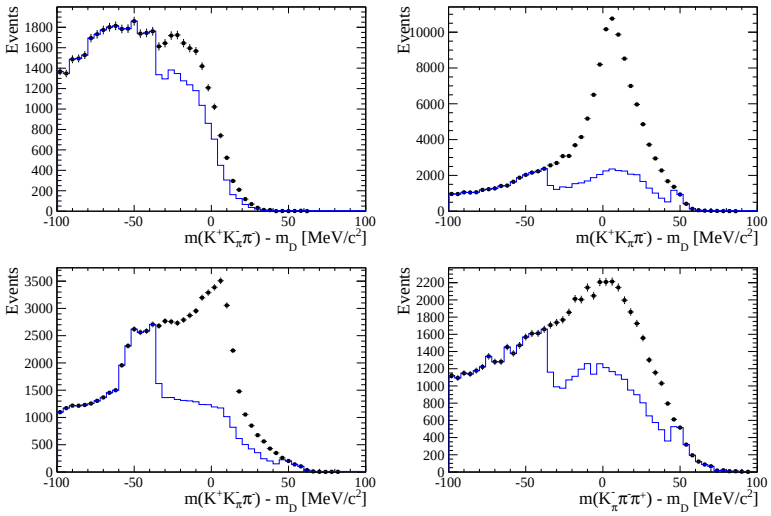

Figure A.1.: Background contributions from D^- decays where the π^- is misidentified as K^-. The D_s invariant mass is recomputed applying the pion mass hypothesis to the kaon and shown for the $D_s \to \phi\pi$, $D_s \to K^*(892)K$, $D_s \to KK\pi$ (non-resonant) and $D_s \to K\pi\pi$ final state categories from top-left to bottom-right. The distributions are shown without (black) and with (blue) the D^--veto applied.

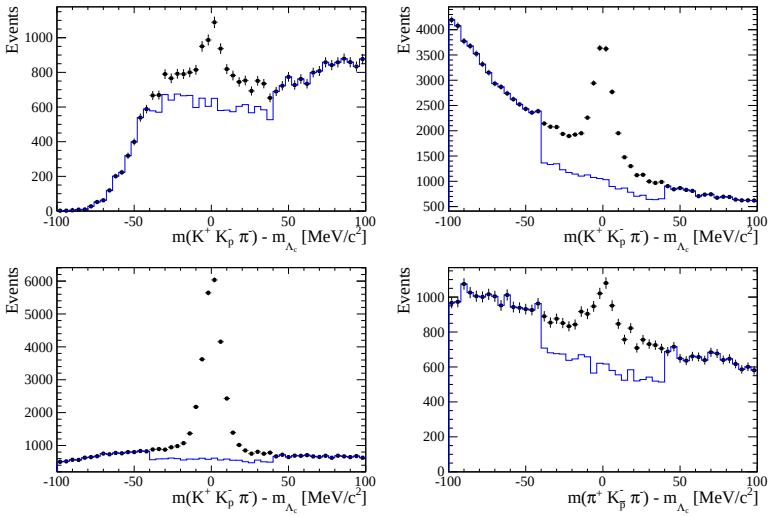

Figure A.2.: Background contributions from Λ_c decays where the $\bar{p}$ is misidentified as K^-. The D_s invariant mass is recomputed applying the proton mass hypothesis to the kaon and shown for the $D_s \to \phi\pi$, $D_s \to K^*(892)K$, $D_s \to KK\pi$ (non-resonant) and $D_s \to K\pi\pi$ final state categories from top-left to bottom-right. The distributions are shown without (black) and with (blue) the Λ_c-veto applied.

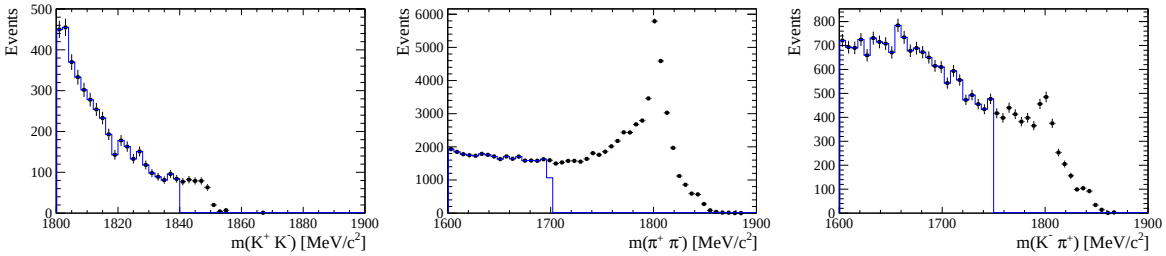

Figure A.3.: Background contributions to invariant mass distribution of $D_s \to KK\pi$ (left), $D_s \to \pi\pi\pi$ (middle) and $D_s \to K\pi\pi$ (right) from $D^0 \to hh$ decays combined with a random pion.

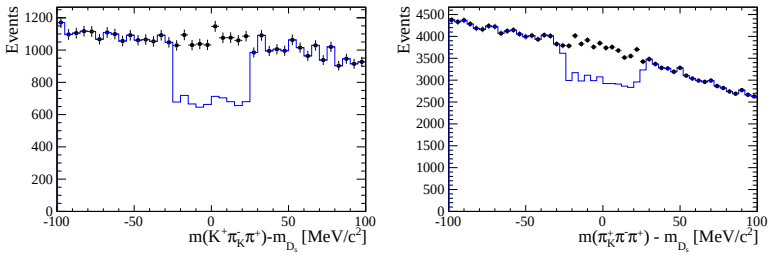

Figure A.4.: Background contributions to invariant mass distribution of $B_s \to D_s K\pi\pi$ (left) and $B_s \to D_s\pi\pi\pi$ (right) from $B_s \to D_s D_s$ decays where the kaon is misidentified as pion. The $X_{s,d}$ invariant mass is recomputed applying the kaon mass hypothesis to the pion and shown without (black) and with (blue) the D_s-veto applied.

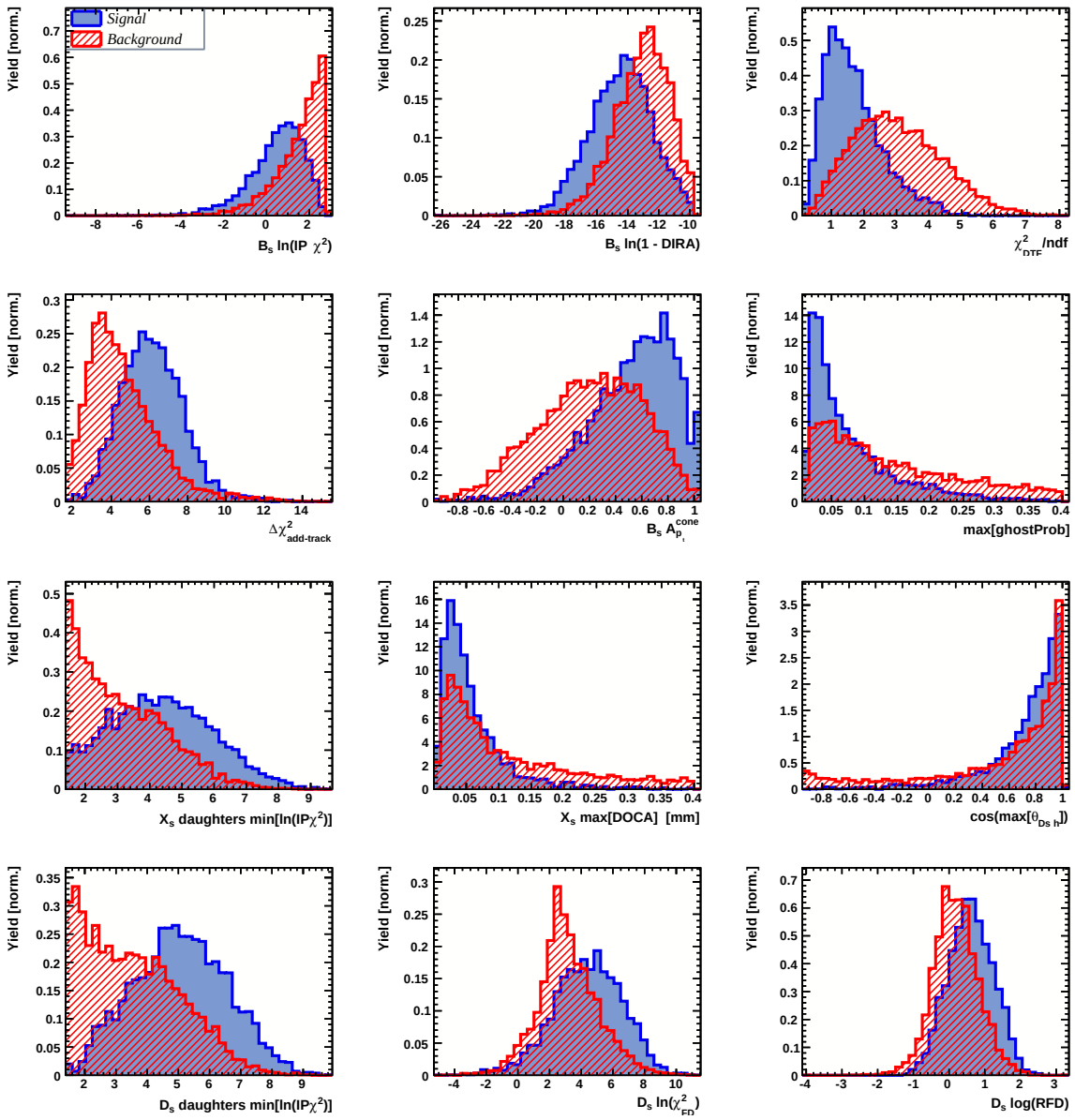

Figure A.5.: Variables used to train the multivariate classifier for category [Run I,L0-TOS].

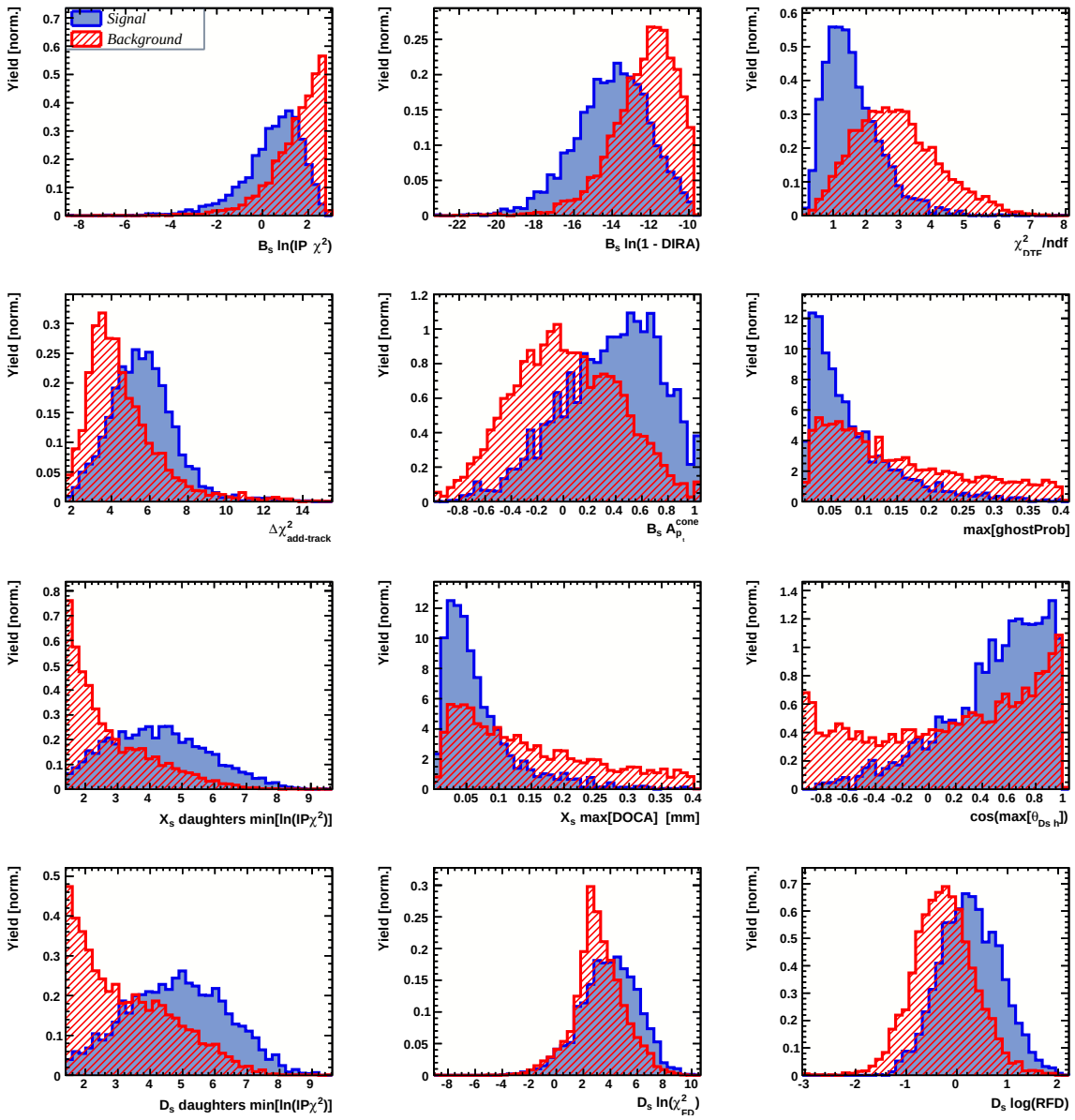

Figure A.6.: Variables used to train the multivariate classifier for category [Run I,L0-TIS].

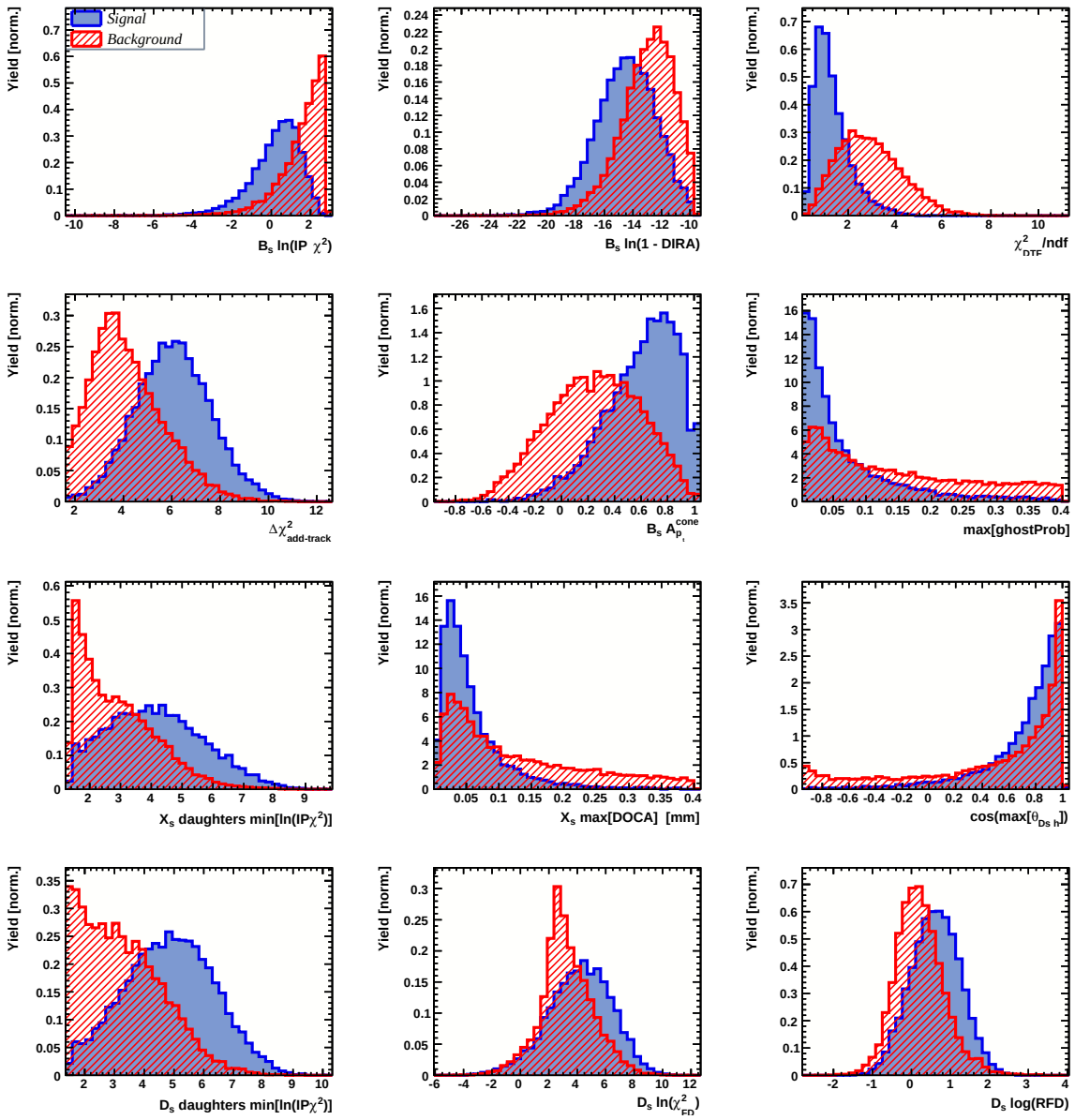

Figure A.7.: Variables used to train the multivariate classifier for category [Run II,L0-TOS].

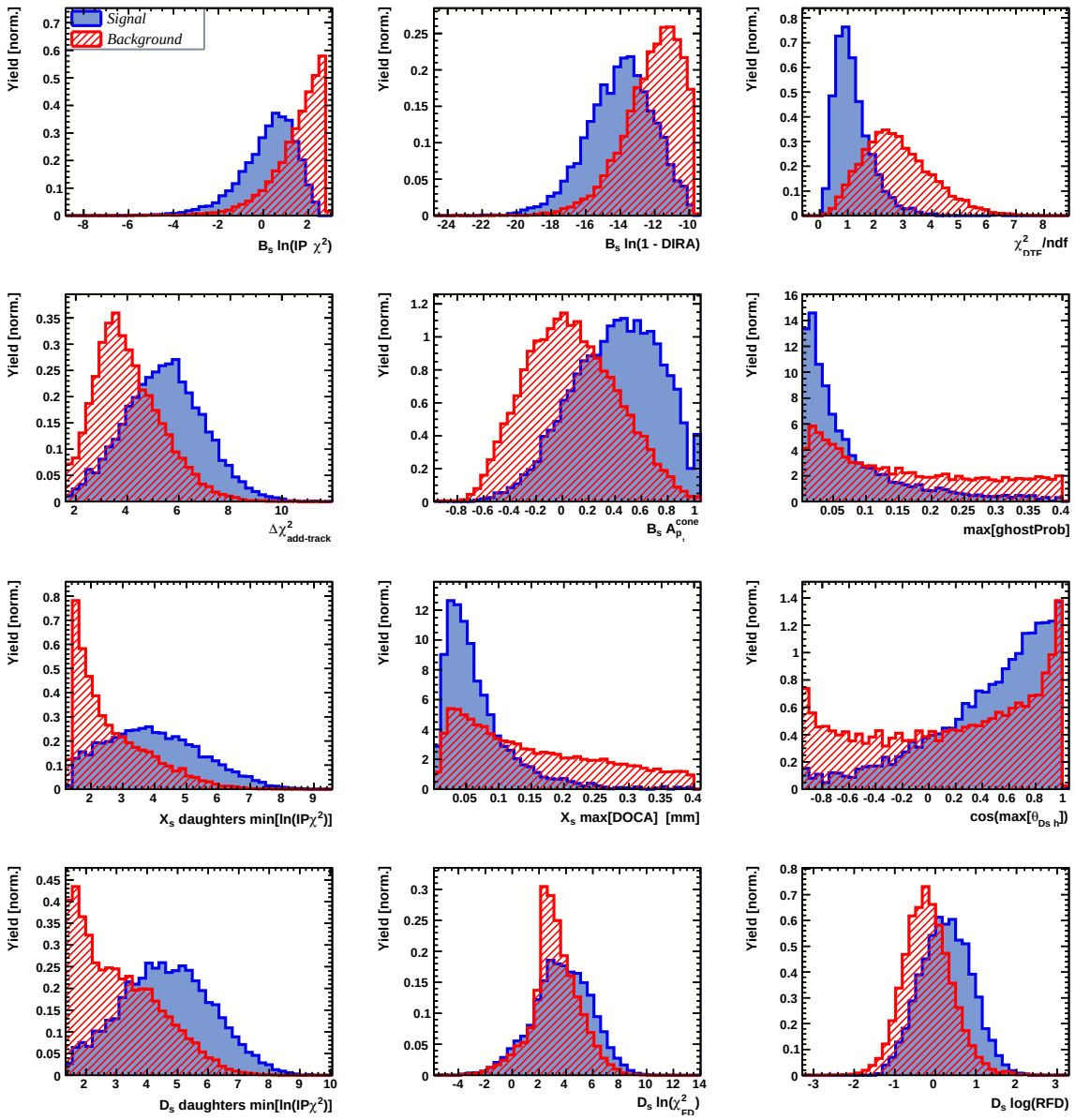

Figure A.8.: Variables used to train the multivariate classifier for category [Run II,L0-TIS].

Appendix B

Detailed fit results for time resolution studies

The first Figure in this section, B.1, contains all fits to the distributions of the decay time difference Δt between the true and the reconstructed decay time of the simulated B_s^0 signal candidates, used to determine the resolution scaling relation for Run I data. The second Figure, B.2, shows the comparison between the unscaled decay-time errors estimated by the decay tree fitter for data taken in 2016 and 2017, while the third and fourth Figures, B.3 and B.4, show the fits to the decay-time distribution of fake B_s^0 candidates, reconstructed using D_s^- mesons that originate from the PV and used for the determination of the resolution scaling relation for Run II data.
All fits are performed in bins of the decay-time error σ_t, where an adaptive binning scheme is used to ensure that approximately the same number of events are found in each bin. The fit results are summarized in Table B.1, B.2 and B.3.

Table B.1.: Measured time resolution for $B_s \to D_s K\pi\pi$ simulation in bins of the per-event decay time error estimate.

σ_t Bin [fs]	σ_1 [fs]	σ_2 [fs]	f_1	D	σ_{eff} [fs]
0.0 - 20.1	19 ± 0.675	33.8 ± 1.77	0.75 ± 0	0.917 ± 0.00406	23.4 ± 0.599
20.1 - 23.2	23.4 ± 0.86	37.4 ± 1.95	0.75 ± 0	0.888 ± 0.00477	27.4 ± 0.621
23.2 - 25.7	28.1 ± 1.02	38.7 ± 2.32	0.75 ± 0	0.86 ± 0.00563	31 ± 0.671
25.7 - 28.0	30.1 ± 1.12	43.2 ± 2.56	0.75 ± 0	0.837 ± 0.00651	33.6 ± 0.734
28.0 - 30.2	32.4 ± 1.12	44.2 ± 2.59	0.75 ± 0	0.819 ± 0.00694	35.5 ± 0.756
30.2 - 32.5	32.6 ± 1.38	49.2 ± 3.04	0.75 ± 0	0.805 ± 0.00792	37.1 ± 0.841
32.5 - 35.4	34.4 ± 1.19	54.7 ± 2.85	0.75 ± 0	0.778 ± 0.0086	39.9 ± 0.879
35.4 - 39.2	41.9 ± 1.8	56.9 ± 4.18	0.75 ± 0	0.719 ± 0.00997	45.7 ± 0.962
39.2 - 44.7	42.2 ± 1.56	68.1 ± 4.01	0.75 ± 0	0.687 ± 0.0114	48.8 ± 1.08
44.7 - 120.0	55.5 ± 2.59	83 ± 14.7	0.75 ± 0	0.546 ± 0.0521	62 ± 4.89

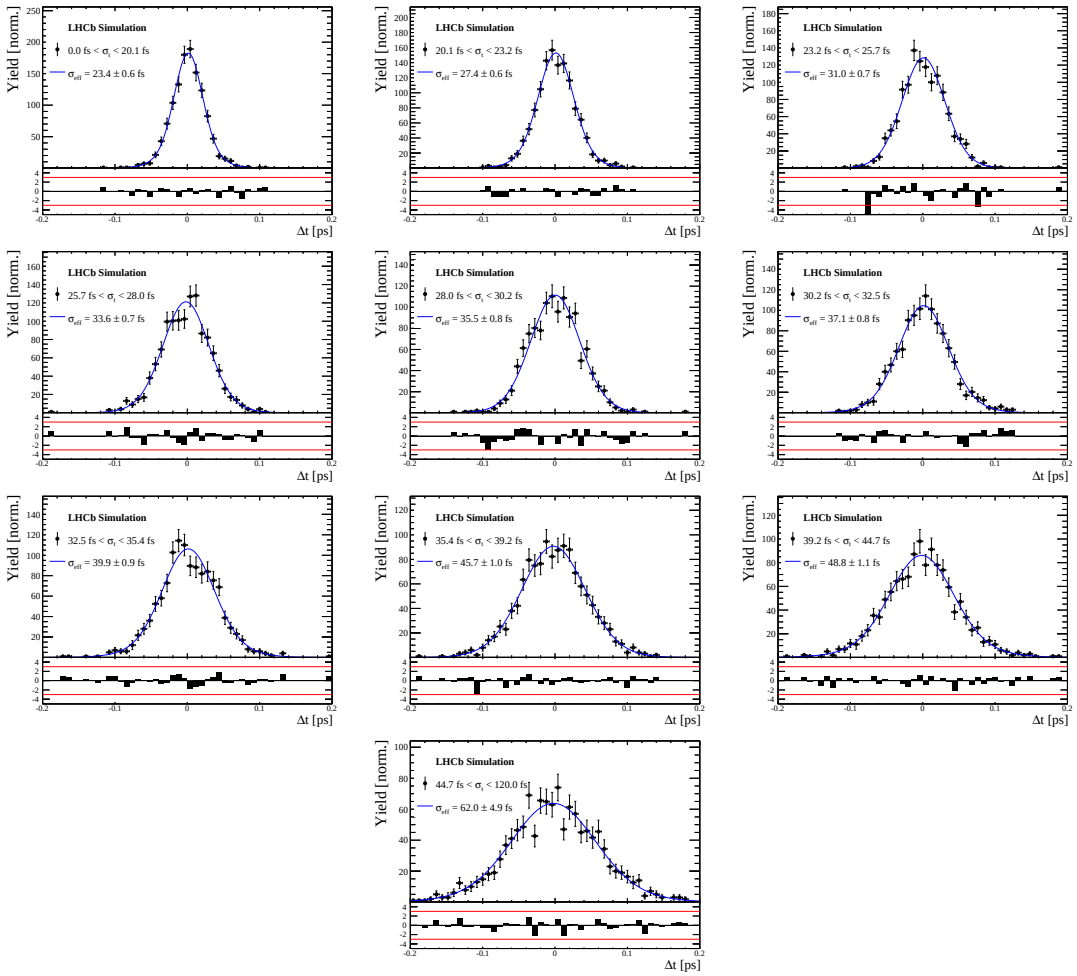

Figure B.1.: Difference of the true and measured decay time of simulated $B_s^0 \to D_s^- K^+ \pi^- \pi^+$ candidates in bins of the per-event decay.time error estimate. The fits described in Chapter 8.1.1 are overlaid.

Table B.2.: Measured time resolution for prompt D_s data in bins of the per-event decay-time error estimate. Data taken in 2016.

σ_t Bin [fs]	σ_1 [fs]	σ_2 [fs]	f_1	D	σ_{eff} [fs]
0.0 - 28.8	25.3 ± 1.05	47.8 ± 2.82	0.75 ± 0	0.853 ± 0.00827	31.8 ± 0.967
28.8 - 34.0	34.4 ± 1.38	60.4 ± 3.66	0.75 ± 0	0.763 ± 0.0114	41.4 ± 1.14
34.0 - 37.7	35.9 ± 1.7	63.1 ± 4.05	0.75 ± 0	0.745 ± 0.0122	43.2 ± 1.2
37.7 - 41.1	38.3 ± 1.63	65.3 ± 4.28	0.75 ± 0	0.723 ± 0.013	45.3 ± 1.26
41.1 - 44.3	43.6 ± 2.04	67.2 ± 4.78	0.75 ± 0	0.679 ± 0.0137	49.6 ± 1.3
44.3 - 47.5	40.4 ± 1.64	85.4 ± 5.28	0.75 ± 0	0.659 ± 0.0151	51.4 ± 1.41
47.5 - 51.1	46.1 ± 2.02	82.5 ± 5.61	0.75 ± 0	0.622 ± 0.0161	54.9 ± 1.5
51.1 - 55.2	49.2 ± 2.1	92.3 ± 6.57	0.75 ± 0	0.577 ± 0.0174	59 ± 1.62
55.2 - 61.2	56.6 ± 2.53	88.8 ± 7.84	0.75 ± 0	0.525 ± 0.0192	64 ± 1.82
61.2 - 100.0	57.6 ± 3.09	112 ± 14.5	0.75 ± 0	0.478 ± 0.0232	68.4 ± 2.25

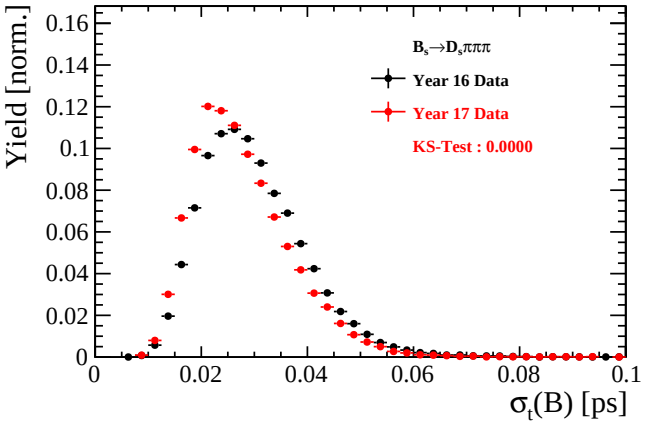

Figure B.2.: Comparison of the unscaled decay-time uncertainty σ_t for background-subtracted $B_s^0 \to D_s^- \pi^+ \pi^- \pi^+$ candidates from data taken in 2016 and 2017.

Table B.3.: Measured time resolution for prompt D_s data in bins of the per-event decay-time error estimate. Data taken in 2017.

σ_t Bin [fs]	σ_1 [fs]	σ_2 [fs]	f_1	D	σ_{eff} [fs]
0.0 - 27.0	22.1 ± 0.942	44.7 ± 2.65	0.75 ± 0	0.877 ± 0.00729	28.8 ± 0.914
27.0 - 31.3	28.3 ± 1.12	48.2 ± 2.98	0.75 ± 0	0.835 ± 0.00854	33.8 ± 0.959
31.3 - 34.7	32.8 ± 1.29	55.8 ± 3.39	0.75 ± 0	0.786 ± 0.0105	39.1 ± 1.08
34.7 - 38.9	33.4 ± 1.2	62.5 ± 3.04	0.75 ± 0	0.764 ± 0.00951	41.3 ± 0.956
38.9 - 42.8	40.3 ± 1.39	63 ± 3.58	0.75 ± 0	0.715 ± 0.0104	46.2 ± 1
42.8 - 45.5	42.2 ± 1.63	70.7 ± 4.35	0.75 ± 0	0.68 ± 0.0138	49.5 ± 1.3
45.5 - 48.4	44.7 ± 1.85	75.7 ± 4.91	0.75 ± 0	0.649 ± 0.0152	52.4 ± 1.42
48.4 - 51.6	46.3 ± 2.05	80.3 ± 5.66	0.75 ± 0	0.626 ± 0.0161	54.6 ± 1.5
51.6 - 55.3	53.2 ± 1.2	69.1 ± 3.03	0.75 ± 0	0.597 ± 0.0167	57.2 ± 1.55
55.3 - 61.0	54.8 ± 2.29	90.9 ± 12.2	0.75 ± 0	0.535 ± 0.0406	62.9 ± 3.82
61.0 - 100.0	58.4 ± 3.18	118 ± 15.6	0.75 ± 0	0.466 ± 0.0233	69.6 ± 2.28

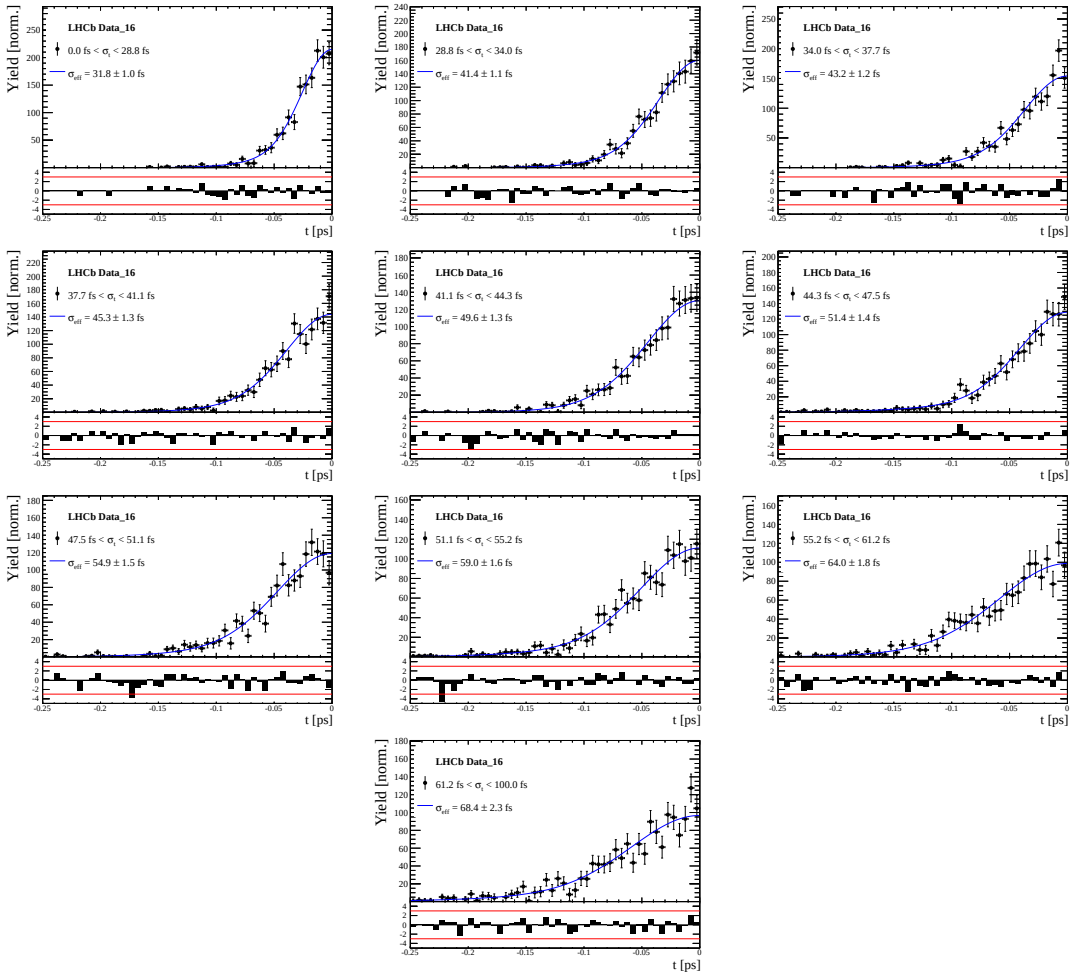

Figure B.3.: Decay-time distribution for fake B_s^0 candidates, reconstructed from D_s^- candidates originating from the PV and combined with random $K^-\pi^+\pi^-$ bachelor particles from the PV. The fits are performed in bins of the per-event decay-time error estimate. Data taken in 2016.

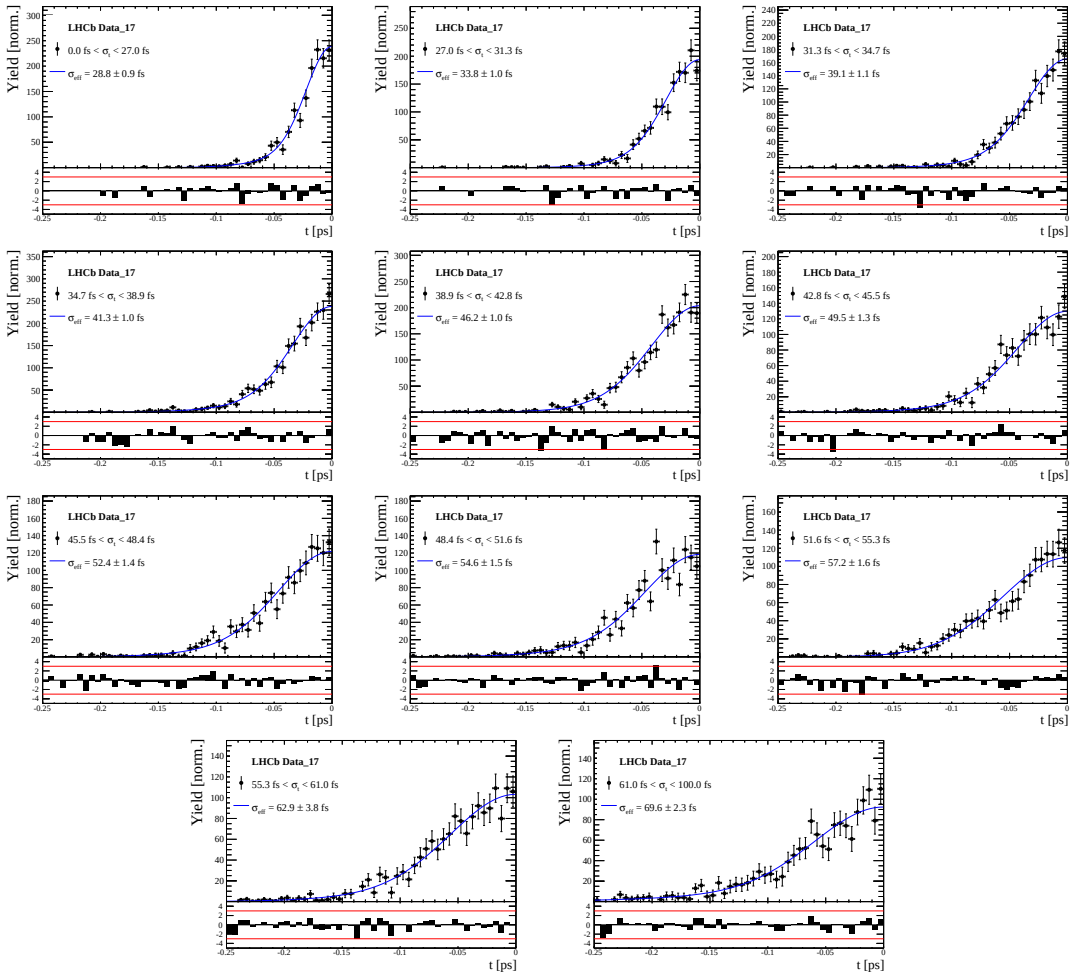

Figure B.4.: Decay-time distribution for fake B_s^0 candidates, reconstructed from D_s^- candidates originating from the PV and combined with random $K^-\pi^+\pi^-$ bachelor particles from the PV. The fits are performed in bins of the per-event decay-time error estimate. Data taken in 2017.

Appendix C

Detailed fit results for time acceptance studies

Table C.1.: Time acceptance parameters for events in category [Run I,L0-TIS].

Knot position	Coefficient	$B_s^0 \to D_s^- K\pi\pi$ data	$B_s^0 \to D_s^- K\pi\pi$ MC	Ratio
0.4	v_0	0.309 ± 0.018	0.410 ± 0.007	1.007 ± 0.029
0.5	v_1	0.694 ± 0.031	0.776 ± 0.011	0.936 ± 0.021
1.4	v_2	0.858 ± 0.043	0.896 ± 0.015	1.004 ± 0.024
2.5	v_3	1.090 ± 0.028	1.099 ± 0.009	0.992 ± 0.015
6.5	v_4	1.0 (fixed)	1.0 (fixed)	1.0 (fixed)
10.0	v_5	0.921 (interpolated)	0.913 (interpolated)	1.007 (interpolated)

Table C.2.: Time acceptance parameters for events in category [Run I,L0-TIS].

Knot position	Coefficient	$B_s^0 \to D_s^- K\pi\pi$ data	$B_s^0 \to D_s^- K\pi\pi$ MC	Ratio
0.4	v_0	0.158 ± 0.014	0.216 ± 0.005	0.986 ± 0.040
0.5	v_1	0.422 ± 0.029	0.524 ± 0.010	0.965 ± 0.029
1.4	v_2	0.802 ± 0.047	0.860 ± 0.017	0.982 ± 0.029
2.5	v_3	1.099 ± 0.034	1.098 ± 0.011	1.002 ± 0.019
6.5	v_4	1.0 (fixed)	1.0 (fixed)	1.0 (fixed)
10.0	v_5	0.913 (interpolated)	0.914 (interpolated)	0.998 (interpolated)

Table C.3.: Time acceptance parameters for events in category [Run II,L0-TOS].

Knot position	Coefficient	$B_s^0 \to D_s^- K\pi\pi$ data	$B_s^0 \to D_s^- K\pi\pi$ MC	Ratio
0.4	v_0	0.285 ± 0.009	0.368 ± 0.005	1.023 ± 0.020
0.5	v_1	0.663 ± 0.017	0.749 ± 0.009	0.911 ± 0.016
1.4	v_2	0.856 ± 0.025	0.893 ± 0.012	1.016 ± 0.019
2.5	v_3	1.060 ± 0.017	1.071 ± 0.008	0.996 ± 0.013
6.5	v_4	1.0 (fixed)	1.0 (fixed)	1.0 (fixed)
10.0	v_5	0.948 (interpolated)	0.938 (interpolated)	1.004 (interpolated)

Table C.4.: Time acceptance parameters for events in category [Run II,L0-TIS].

Knot position	Coefficient	$B_s^0 \to D_s^- K\pi\pi$ data	$B_s^0 \to D_s^- K\pi\pi$ MC	Ratio
0.4	v_0	0.117 ± 0.008	0.171 ± 0.003	0.965 ± 0.034
0.5	v_1	0.422 ± 0.019	0.474 ± 0.008	0.952 ± 0.024
1.4	v_2	0.733 ± 0.027	0.777 ± 0.013	0.973 ± 0.025
2.5	v_3	1.071 ± 0.020	1.046 ± 0.010	0.989 ± 0.015
6.5	v_4	1.0 (fixed)	1.0 (fixed)	1.0 (fixed)
10.0	v_5	0.938 (interpolated)	0.959 (interpolated)	1.009 (interpolated)

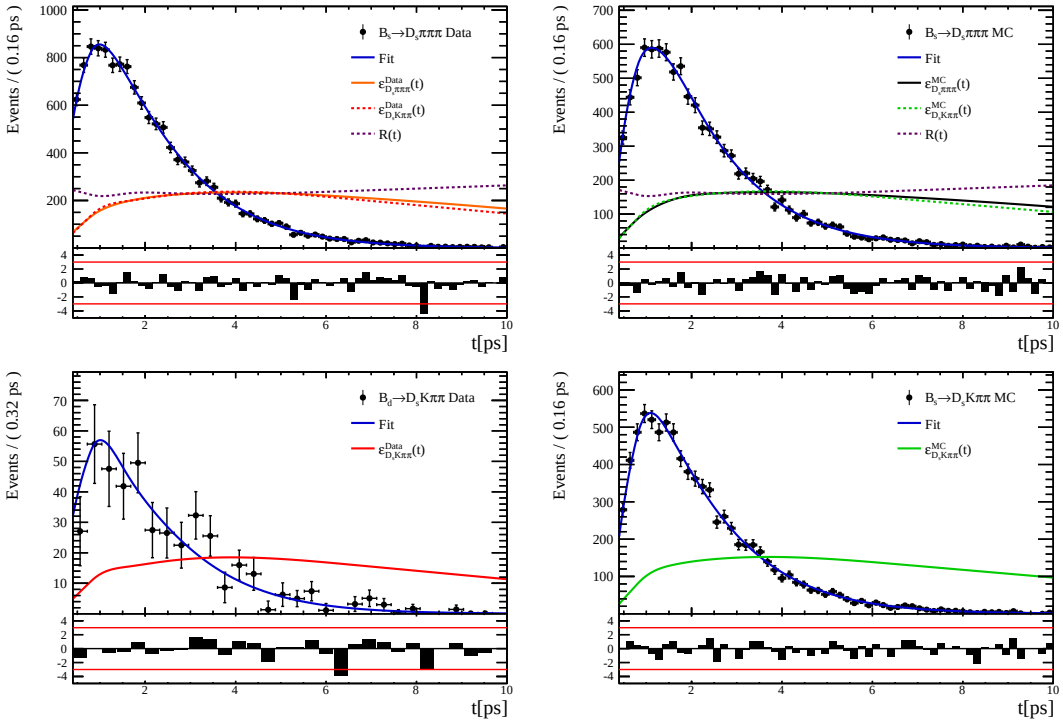

Figure C.1.: Decay-time fit projections for $B_s^0 \to D_s^- \pi\pi\pi$ data (top-left), $B_s^0 \to D_s^- \pi\pi\pi$ simulation (top-right), $B_d^0 \to D_s^- K\pi\pi$ data (bottom-left) and $B_s^0 \to D_s^- K\pi\pi$ simulation (bottom-right) in category [Run I,L0-TOS].
The respective acceptance function is overlaid in an arbitrary scale.

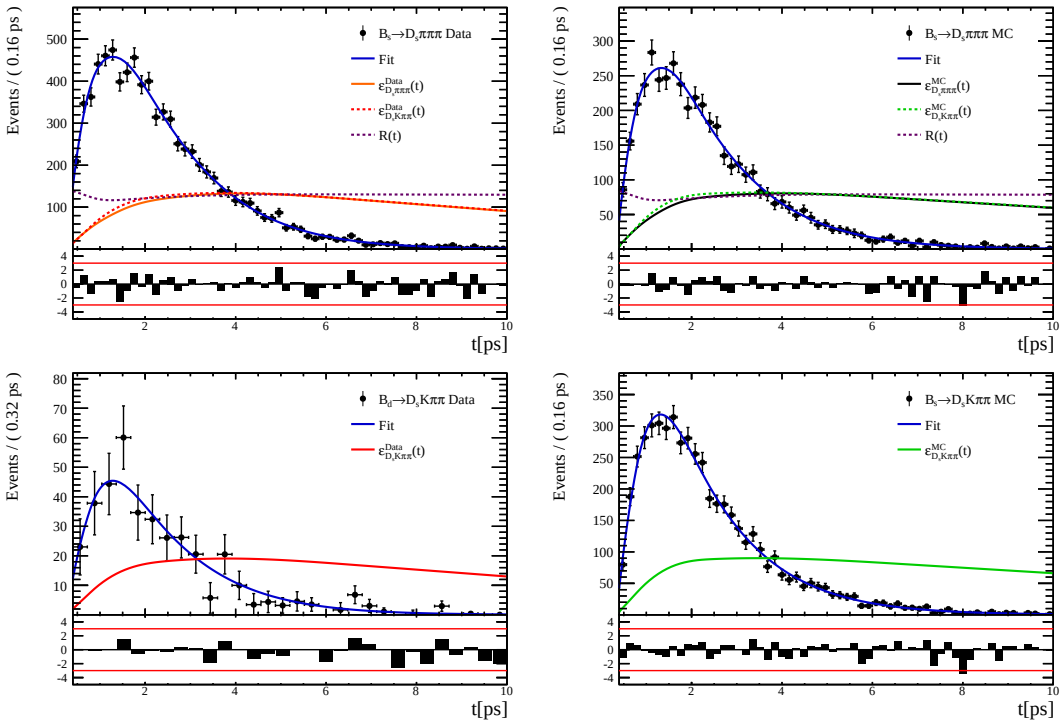

Figure C.2.: Decay-time fit projections for $B_s^0 \to D_s^- \pi\pi\pi$ data (top-left), $B_s^0 \to D_s^- \pi\pi\pi$ simulation (top-right), $B_d^0 \to D_s^- K\pi\pi$ data (bottom-left) and $B_s^0 \to D_s^- K\pi\pi$ simulation (bottom-right) in category [Run I,L0-TIS].
The respective acceptance function is overlaid in an arbitrary scale.

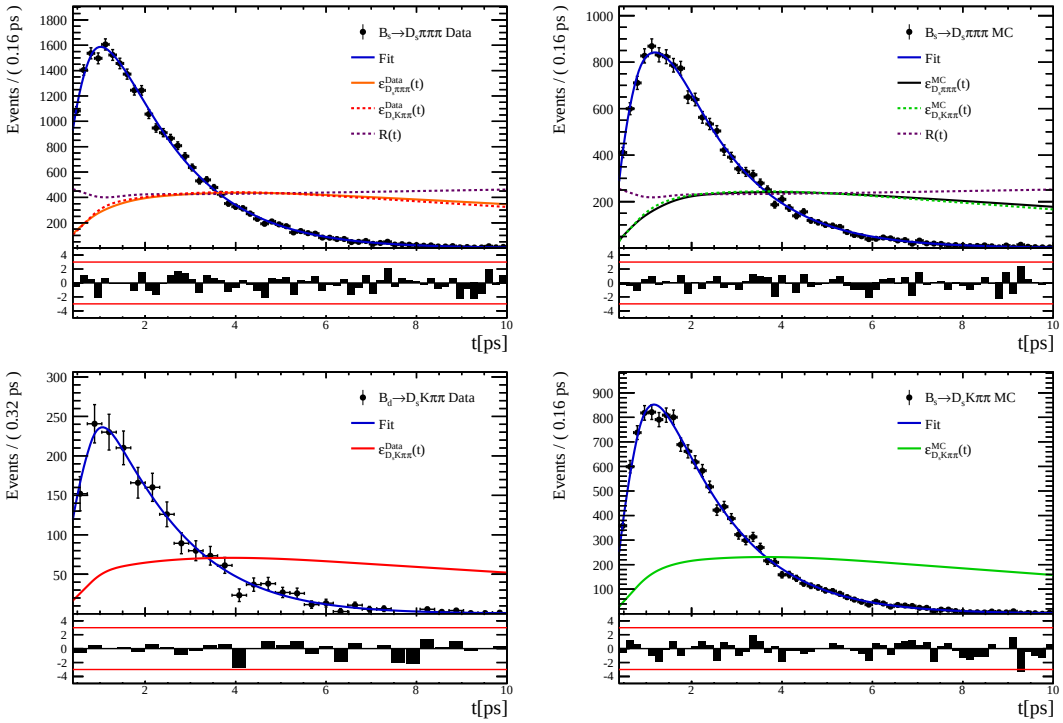

Figure C.3.: Decay-time fit projections for $B_s^0 \to D_s^- \pi\pi\pi$ data (top-left), $B_s^0 \to D_s^- \pi\pi\pi$ simulation (top-right), $B_d^0 \to D_s^- K\pi\pi$ data (bottom-left) and $B_s^0 \to D_s^- K\pi\pi$ simulation (bottom-right) in category [Run II,L0-TOS].
The respective acceptance function is overlaid in an arbitrary scale.

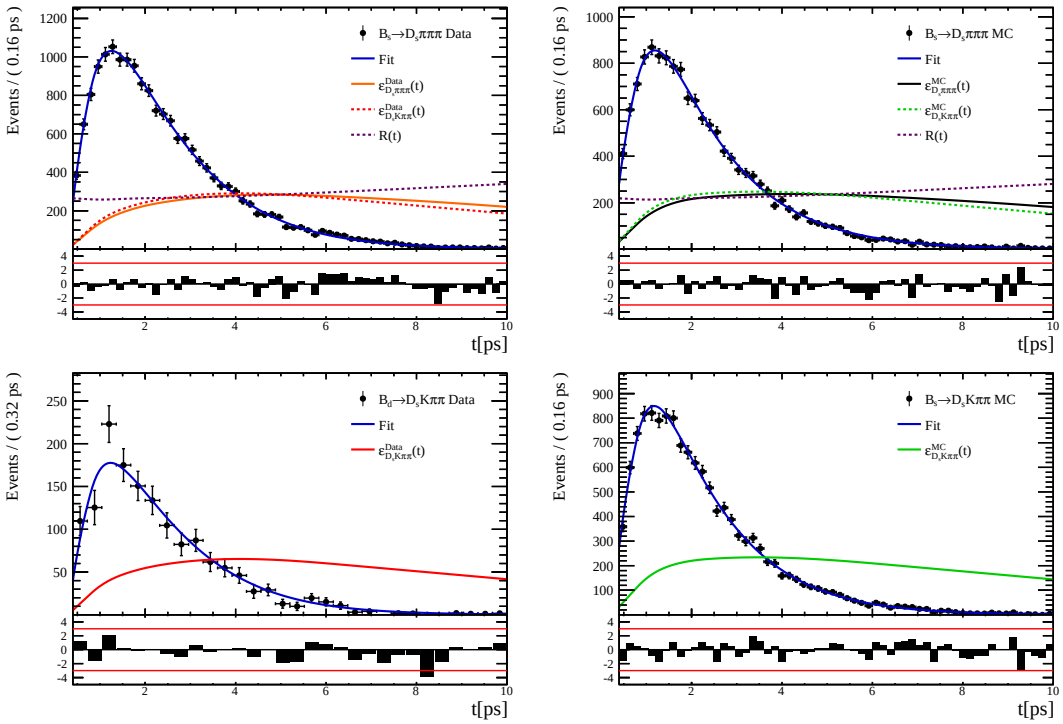

Figure C.4.: Decay-time fit projections for $B_s^0 \to D_s^- \pi\pi\pi$ data (top-left), $B_s^0 \to D_s^- \pi\pi\pi$ simulation (top-right), $B_d^0 \to D_s^- K\pi\pi$ data (bottom-left) and $B_s^0 \to D_s^- K\pi\pi$ simulation (bottom-right) in category [Run II,L0-TIS].
The respective acceptance function is overlaid in an arbitrary scale.

Appendix D

Production asymmetry

The following Table contains the measured B_s^0 production asymmetries in bins of p_t and η of the B_s^0 candidates for Run I.

Table D.1.: B_s production asymmetries in kinematic slices for data taken at $\sqrt{s} = 7\ TeV$ and $\sqrt{s} = 8\ TeV$ [83].

p_{T} [GeV/c]	η	$A_{\mathrm{P}}(B_s^0)_{\sqrt{s}=7\ \mathrm{TeV}}$	$A_{\mathrm{P}}(B_s^0)_{\sqrt{s}=8\ \mathrm{TeV}}$
$(2.00, 7.00)$	$(2.10, 3.00)$	$0.0166 \pm 0.0632 \pm 0.0125$	$0.0412 \pm 0.0416 \pm 0.0150$
$(2.00, 7.00)$	$(3.00, 3.30)$	$0.0311 \pm 0.0773 \pm 0.0151$	$-0.0241 \pm 0.0574 \pm 0.0079$
$(2.00, 7.00)$	$(3.30, 4.50)$	$-0.0833 \pm 0.0558 \pm 0.0132$	$0.0166 \pm 0.0391 \pm 0.0092$
$(7.00, 9.50)$	$(2.10, 3.00)$	$0.0364 \pm 0.0479 \pm 0.0068$	$0.0482 \pm 0.0320 \pm 0.0067$
$(7.00, 9.50)$	$(3.00, 3.30)$	$0.0206 \pm 0.0682 \pm 0.0127$	$0.0983 \pm 0.0470 \pm 0.0155$
$(7.00, 9.50)$	$(3.30, 4.50)$	$0.0058 \pm 0.0584 \pm 0.0089$	$-0.0430 \pm 0.0386 \pm 0.0079$
$(9.50, 12.00)$	$(2.10, 3.00)$	$-0.0039 \pm 0.0456 \pm 0.0121$	$0.0067 \pm 0.0303 \pm 0.0063$
$(9.50, 12.00)$	$(3.00, 3.30)$	$0.1095 \pm 0.0723 \pm 0.0179$	$-0.1283 \pm 0.0503 \pm 0.0171$
$(9.50, 12.00)$	$(3.30, 4.50)$	$0.1539 \pm 0.0722 \pm 0.0212$	$-0.0500 \pm 0.0460 \pm 0.0104$
$(12.00, 30.00)$	$(2.10, 3.00)$	$-0.0271 \pm 0.0336 \pm 0.0061$	$-0.0012 \pm 0.0222 \pm 0.0050$
$(12.00, 30.00)$	$(3.00, 3.30)$	$-0.0542 \pm 0.0612 \pm 0.0106$	$0.0421 \pm 0.0416 \pm 0.0162$
$(12.00, 30.00)$	$(3.30, 4.50)$	$-0.0586 \pm 0.0648 \pm 0.0150$	$0.0537 \pm 0.0447 \pm 0.0124$

Appendix E

Considered decay chains for the amplitude fit

Table E.1.: Decays considered in the LASSO model building, taken from [5]. The letters S, P, D correspond to the different spin-states (S=0, P=1, D=2) of the respective particle.

Decay channel
$B_s \to D_s^- \, [K_1(1270)^+[S,D] \to \pi^+ \, K^*(892)^0]$
$B_s \to D_s^- \, [K_1(1270)^+ \to \pi^+ \, K^*(1430)^0]$
$B_s \to D_s^- \, [K_1(1270)^+[S,D] \to K^+ \, \rho(770)^0]$
$B_s \to D_s^- \, [K_1(1270)^+[S,D] \to K^+ \, \omega(782)]$
$B_s \to D_s^- \, [K_1(1400)^+[S,D] \to \pi^+ \, K^*(892)^0]$
$B_s \to D_s^- \, [K_1(1400)^+[S,D] \to K^+ \, \rho(770)^0]$
$B_s \to D_s^- \, [K(1460)^+ \to \pi^+ \, \kappa]$
$B_s \to D_s^- \, [K(1460)^+ \to K^+ \, \sigma]$
$B_s \to D_s^- \, [K(1460)^+ \to \pi^+ \, K^*(892)^0]$
$B_s \to D_s^- \, [K(1460)^+ \to K^+ \, \rho(770)^0]$
$B_s \to D_s^- \, [K^*(1410)^+ \to \pi^+ \, K^*(892)^0]$
$B_s \to D_s^- \, [K^*(1410)^+ \to K^+ \, \rho(770)^0]$
$B_s \to D_s^- \, [K_2^*(1430)^+ \to \pi^+ \, K^*(892)^0]$
$B_s \to D_s^- \, [K_2^*(1430)^+ \to K^+ \, \rho(770)^0]$
$B_s \to D_s^- \, [K^*(1680)^+ \to \pi^+ \, K^*(892)^0]$
$B_s \to D_s^- \, [K^*(1680)^+ \to K^+ \, \rho(770)^0]$
$B_s \to D_s^- \, [K_2(1770)^+ \to \pi^+ \, K^*(892)^0]$
$B_s \to D_s^- \, [K_2(1770)^+ \to K^+ \, \rho(770)^0]$
$B_s \to \sigma^0 (D_s^- K^+)_S$
$B_s[S,P,D] \to \sigma^0 (D_s^- K^+)_V$
$B_s \to \rho(770)^0 (D_s^- K^+)_S$
$B_s[S,P,D] \to \rho(770)^0 \, (D_s^- K^+)_V$
$B_s \to K^*(892)^0 \, (D_s^- \pi^+)_S$
$B_s[S,P,D] \to K^*(892)^0 \, (D_s^- \pi^+)_V$
$B_s \to (D_s^- K^+)_S \, (\pi^+ \pi^-)_S$

Bibliography

[1] http://lhcb-public.web.cern.ch/lhcb-public/en/Collaboration/Collaboration-en.html.

[2] CLEO Collaboration, M. Artuso *et al.*, *Amplitude analysis of* $D^0 \to K^+K^-\pi^+\pi^-$, Phys. Rev. D **85** (2012) 122002.

[3] P. d'Argent *et al.*, *Amplitude Analyses of* $D^0 \to \pi^+\pi^-\pi^+\pi^-$ *and* $D^0 \to K^+K^-\pi^+\pi^-$ *Decays*, JHEP **05** (2017) 143, arXiv:1703.08505.

[4] LHCb, R. Aaij *et al.*, *Measurement of CP asymmetry in* $B_s^0 \to D_s^{\mp}K^{\pm}$ *decays*, JHEP **03** (2018) 059, arXiv:1712.07428.

[5] LHCb, E. M. Gersabeck, P. D'Argent, M. T. Schiller, and M. Kecke, *Measurement of the CKM angle* γ *using* $B_s \to D_sK\pi\pi$ *decays*, LHCb-ANA-2018-021.

[6] LHCb, R. Aaij *et al.*, *Measurement of the CKM angle* γ *using a time-dependent amplitude analysis of* $B_s \to D_sK\pi\pi$ *decays at LHCb*, LHCb-PAPER-2019-0XX, in preparation.

[7] A. Fowlie, *CMSSM, naturalness and the "fine-tuning price" of the Very Large Hadron Collider*, Phys. Rev. **D90** (2014) 015010, arXiv:1403.3407.

[8] ATLAS, G. Aad *et al.*, *Observation of a new particle in the search for the standard model higgs boson with the atlas detector at the lhc*, Physics Letters B **716** (2012), no. 1 1 .

[9] CMS, S. Chatrchyan *et al.*, *Observation of a new boson at a mass of 125 gev with the cms experiment at the lhc*, Physics Letters B **716** (2012), no. 1 30 .

[10] LHCb collaboration, R. Aaij *et al.*, *Observation of $J/\Psi p$ resonances consistent with pentaquark states in $\Lambda_b^0 \to J/\Psi p K^-$ decays*, Phys. Rev. Lett. **115** (2015) 072001, arXiv:1507.03414.

[11] I. Dunietz and R. G. Sachs, *Asymmetry Between Inclusive Charmed and Anticharmed Modes in B0, Anti-b0 Decay as a Measure of CP Violation*, Phys. Rev. **D37** (1988) 3186, [Erratum: Phys. Rev.D39,3515(1989)].

[12] R. Aleksan, I. Dunietz, and B. Kayser, *Determining the cp-violating phase γ*, Zeitschrift für Physik C Particles and Fields **54** (1992) 653.

[13] R. Fleischer, *New strategies to obtain insights into CP violation through $B_s \to D_s^{\pm} K^{\pm}$, $D_s^{*\pm} K^{\pm}$ and $B_d \to D^{\pm}\pi^{\pm}$, $D^{*\pm}\pi^{\pm}$ decays*, Nucl. Phys. **B671** (2003) 459, arXiv:hep-ph/0304027.

[14] N. Cabibbo, *Unitary symmetry and leptonic decays*, Phys. Rev. Lett. **10** (1963) 531.

[15] M. Kobayashi and T. Maskawa, *Cp violation in the renormalizable theory of weak interaction*, Progress of Theoretical Physics **49** (1973), no. 2 652, arXiv:http://ptp.oxfordjournals.org/content/49/2/652.full.pdf+html.

[16] D. J. Gross and F. Wilczek, *Asymptotically free gauge theories*, Phys. Rev. D **8** (1973) 3633.

[17] S. L. Glashow, *Partial-symmetries of weak interactions*, Nuclear Physics **22** (1961), no. 4 579 .

[18] A. Salam and J. C. Ward, *Weak and electromagnetic interactions*, Il Nuovo Cimento Series 10 **11** (1959), no. 4 568.

[19] S. Weinberg, *A model of leptons*, Phys. Rev. Lett. **19** (1967) 1264.

[20] Particle Data Group, M. Tanabashi *et al.*, *Review of particle physics*, Phys. Rev. D **98** (2018) 030001.

[21] P. W. Higgs, *Broken symmetries and the masses of gauge bosons*, Phys. Rev. Lett. **13** (1964) 508.

[22] M. E. Peskin and D. V. Schroeder, *An Introduction to quantum field theory*, Addison-Wesley, Reading, USA, 1995.

[23] W. Pauli, *Contributions mathematiques a la theorie des matrices de dirac*, Annales de l'institut Henri Poincare **6** (1936), no. 2 109.

[24] L. Wolfenstein, *Parametrization of the kobayashi-maskawa matrix*, Phys. Rev. Lett. **51** (1983) 1945.

[25] M. Neuner, *Determination of the b-hadron production cross-section and measurement of CP violation in $B_s^0 \to \phi\phi$ decays at the LHCb experiment*, PhD thesis, Physikalisches Institut, Heidelberg, 2017, Presented on 21 June 2017.

[26] LHCb collaboration, R. Aaij *et al.*, *Determination of the quark coupling strength $|V_{ub}|$ using baryonic decays*, Nature Physics **11** (2015) 743, arXiv:1504.01568.

[27] LHCb collaboration, R. Aaij *et al.*, *A precise measurement of the B^0 meson oscillation frequency*, Eur. Phys. J. **C76** (2016) 412, arXiv:1604.03475.

[28] LHCb collaboration, R. Aaij *et al.*, *Precision measurement of CP violation in $B_s^0 \to J\Psi K^+K^-$ decays*, Phys. Rev. Lett. **114** (2015) 041801, arXiv:1411.3104.

[29] CKMfitter Group, J. Charles *et al.*, *CP violation and the CKM matrix: Assessing the impact of the asymmetric B factories*, Eur. Phys. J. **C41** (2005), no. 1 1, arXiv:hep-ph/0406184.

[30] A. Lenz *et al.*, *Anatomy of New Physics in $B - \bar{B}$ mixing*, Phys. Rev. **D83** (2011) 036004, arXiv:1008.1593.

[31] I. Dunietz, R. Fleischer, and U. Nierste, *In pursuit of new physics with B_s decays*, Phys. Rev. **D63** (2001) 114015, arXiv:hep-ph/0012219.

[32] http://www.physik.uzh.ch/ che/FeynDiag/Details.php?code=52200101.

[33] S. L. Glashow, J. Iliopoulos, and L. Maiani, *Weak interactions with lepton-hadron symmetry*, Phys. Rev. D **2** (1970) 1285.

[34] A. D. Sakharov, *Violation of cp in variance, c asymmetry, and baryon asymmetry of the universe*, Soviet Physics Uspekhi **34** (1991), no. 5 392.

[35] I. Dunietz and J. L. Rosner, *Time-dependent cp-violation effects in $B^0 - \bar{B}^0$ systems*, Phys. Rev. D **34** (1986) 1404.

[36] LHCb, S. Blusk, *Measurement of the CP observables in $\bar{B}^0_s \to D^+_s K^-$ and first observation of $\bar{B}^0_{(s)} \to D^+_s K^- \pi^+ \pi^-$ and $\bar{B}^0_s \to D_{s1}(2536)^+ \pi^-$*, 2012. arXiv:1212.4180.

[37] K. De Bruyn *et al.*, *Exploring $B_s \to D_s^{(*)\pm} K^\mp$ Decays in the Presence of a Sizable Width Difference $\Delta\Gamma_s$*, Nucl. Phys. **B868** (2013) 351, arXiv:1208.6463.

[38] LHCb collaboration, R. Aaij *et al.*, *Measurement of the flavour-specific CP-violating asymmetry $a^s_{\rm sl}$ in B^0_s decays*, Phys. Lett. **B728** (2014) 607, arXiv:1308.1048.

[39] E. Byckling and K. Kajantie, *Particle Kinematics*, John Wiley & Sons, 1973.

[40] S. Mandelstam, J. E. Paton, R. F. Peierls, and A. Q. Sarker, *Isobar approximation of production processes*, Annals of Physics **18** (1962), no. 2 198 .

[41] D. J. Herndon, P. Söding, and R. J. Cashmore, *Generalized isobar model formalism*, Phys. Rev. D **11** (1975) 3165.

[42] J. J. Brehm, *Unitarity and the isobar model: Two-body discontinuities*, Annals of Physics **108** (1977), no. 2 454 .

[43] F. von Hippel and C. Quigg, *Centrifugal-barrier effects in resonance partial decay widths, shapes, and production amplitudes*, Phys. Rev. D **5** (1972) 624.

[44] J. D. Jackson, *Remarks on the phenomenological analysis of resonances*, Il Nuovo Cimento Series 10 **34** (1964), no. 6 1644.

[45] C. Zemach, *Use of angular momentum tensors*, Phys. Rev. **140** (1965) B97.

[46] W. Rarita and J. Schwinger, *On a theory of particles with half integral spin*, Phys. Rev. **60** (1941) 61.

[47] S. U. Chung, *General formulation of covariant helicity-coupling amplitudes*, Phys. Rev. D **57** (1998) 431.

[48] B. S. Zou and D. V. Bugg, *Covariant tensor formalism for partial wave analyses of ψ decay to mesons*, Eur. Phys. J. **A16** (2003) 537, arXiv:hep-ph/0211457.

[49] V. Filippini, A. Fontana, and A. Rotondi, *Covariant spin tensors in meson spectroscopy*, Phys. Rev. **D51** (1995) 2247.

[50] J.-J. Zhu, *Explicit expressions of spin wave functions*, arXiv:hep-ph/9906250.

[51] LHCb collaboration, R. Aaij *et al.*, *First observation of the decays* $\bar{B}^0_{(s)} \to D_s^+ K^- \pi^+ \pi^-$ *and* $\bar{B}^0_s \to D_{s1}(2536)^+ \pi^-$, Phys. Rev. **D86** (2012) 112005, arXiv:1211.1541.

[52] http://lhcb.web.cern.ch/lhcb/speakersbureau/html/Material_for_Presentations.html.

[53] K. Cornelis and R. Schmidt, *The performance of the sps as lep injector*, in *Proceedings of the 1989 IEEE Particle Accelerator Conference 'Accelerator Science and Technology'*, pp. 1853–1855 vol.3, March, 1989. doi: 10.1109/PAC.1989.72946.

[54] LHCb collaboration, R. Aaij *et al.*, *LHCb detector performance*, Int. J. Mod. Phys. **A30** (2015) 1530022, arXiv:1412.6352.

[55] ATLAS, A. Tricoli, *Parton Densities at the LHC*, Frascati Phys. Ser. **49** (2009) 376, arXiv:0808.2579.

[56] J. Nardulli, *Reconstruction of two-body B decays in LHCb*, PhD thesis, NIKHEF, Amsterdam, 2007, Presented on 04 Oct 2007.

[57] LHCb collaboration, A. A. Alves Jr. *et al.*, *The LHCb detector at the LHC*, JINST **3** (2008) S08005.

[58] R. Aaij *et al.*, *Performance of the LHCb Vertex Locator*, JINST **9** (2014) P09007, arXiv:1405.7808.

[59] http://lhcb.physik.uzh.ch/ST/public/material/index.php.

[60] R. Arink *et al.*, *Performance of the LHCb Outer Tracker*, JINST **9** (2014) P01002, arXiv:1311.3893.

[61] R. E. Kalman, *A new approach to linear filtering and prediction problems*, ASME Journal of Basic Engineering (1960).

[62] LHCb, R. Aaij *et al.*, *Measurement of the track reconstruction efficiency at LHCb*, JINST **10** (2015), no. 02 P02007, arXiv:1408.1251.

[63] M. Adinolfi *et al.*, *Performance of the LHCb RICH detector at the LHC*, Eur. Phys. J. **C73** (2013) 2431, arXiv:1211.6759.

[64] R. Aaij *et al.*, *Performance of the LHCb calorimeters*, LHCb-DP-2013-004, in preparation.

[65] F. Archilli *et al.*, *Performance of the muon identification at LHCb*, JINST **8** (2013) P10020, arXiv:1306.0249.

[66] R. Aaij *et al.*, *The LHCb trigger and its performance in 2011*, JINST **8** (2013) P04022, arXiv:1211.3055.

[67] V. Blobel and E. Lohrmann, *Statistische und numerische Methoden der Datenanalyse*, Teubner Studienbücher Physik, Teubner, Stuttgart, 1998.

[68] A. Hoecker *et al.*, *TMVA: Toolkit for Multivariate Data Analysis*, PoS **ACAT** (2007) 040, arXiv:physics/0703039.

[69] L. Breiman, J. H. Friedman, R. A. Olshen, and C. J. Stone, *Classification and regression trees*, Wadsworth international group, Belmont, California, USA, 1984.

[70] R. E. Schapire, *The strength of weak learnability*, Machine Learning **5** (1990) 197.

[71] M. Pivk and F. R. Le Diberder, *Plots: A statistical tool to unfold data distributions*, Nuclear Instruments and Methods in Physics Research A **555** (2005) 356, physics/04.

[72] W. D. Hulsbergen, *Decay chain fitting with a Kalman filter*, Nucl. Instrum. Meth. **A552** (2005) 566, arXiv:physics/0503191.

[73] N. L. Johnson, *Systems of frequency curves generated by methods of translation*, Biometrika **36** (1949), no. 1/2 149.

[74] L. Anderlini *et al.*, *The PIDCalib package*, Tech. Rep. LHCb-PUB-2016-021. CERN-LHCb-PUB-2016-021, CERN, Geneva, Jul, 2016.

[75] T. Skwarnicki, *A study of the radiative cascade transitions between the Upsilon-prime and Upsilon resonances*, PhD thesis, Institute of Nuclear Physics, Krakow, 1986, DESY-F31-86-02.

[76] W. D. Hulsbergen, *Decay chain fitting with a Kalman filter*, Nuclear Instruments and Methods in Physics Research A **552** (2005) 566, arXiv:physics/0503191.

[77] Heavy Flavor Averaging Group, Y. Amhis *et al.*, *Averages of b-hadron, c-hadron, and τ-lepton properties as of summer 2016*, Eur. Phys. J. **C77** (2017) 895, arXiv:1612.07233, updated results and plots available at https://hflav.web.cern.ch.

[78] T. M. Karbach, G. Raven, and M. Schiller, *Decay time integrals in neutral meson mixing and their efficient evaluation*, arXiv:1407.0748.

[79] LHCb, R. Aaij *et al.*, *Effective lifetime measurements in the $B_s^0 \to K^+K^-$, $B^0 \to K^+\pi^-$ and $B_s^0 \to \pi^+K^-$ decays*, Physics Letters B **736** (2014) 446 .

[80] LHCb collaboration, R. Aaij *et al.*, *Opposite-side flavour tagging of B mesons at the LHCb experiment*, Eur. Phys. J. **C72** (2012) 2022, arXiv:1202.4979.

[81] LHCb, R. Aaij *et al.*, *A new algorithm for identifying the flavour of B_s^0 mesons at LHCb*, JINST **11** (2016), no. 05 P05010, arXiv:1602.07252.

[82] J. Wimberley, *Calibrating flavor tagging algorithms with binominal regression*, Tech. Rep. LHCb-INT-2017-002. CERN-LHCb-INT-2017-002, CERN, Geneva, Jan, 2017.

[83] LHCb, R. Aaij *et al.*, *Measurement of B^0, B_s^0, B^+ and Λ_b^0 production asymmetries in 7 and 8 TeV proton-proton collisions*, Phys. Lett. **B774** (2017) 139, arXiv:1703.08464.

[84] H. Gordon, R. W. Lambert, J. van Tilburg, and M. Vesterinen, *A Measurement of the $K\pi$ Detection Asymmetry*, Tech. Rep. LHCb-INT-2012-027. CERN-LHCb-INT-2012-027, CERN, Geneva, Feb, 2013.

[85] A. Davis *et al.*, *Measurement of the instrumental asymmetry for $K^-\pi^+$-pairs at LHCb in Run 2*, Tech. Rep. LHCb-PUB-2018-004. CERN-LHCb-PUB-2018-004, CERN, Geneva, Mar, 2018.

[86] I. I. Y. Bigi and H. Yamamoto, *Interference between Cabibbo allowed and doubly forbidden transitions in $D \to K_s,\ K_L + \pi$ decays*, Phys. Lett. **B349** (1995) 363, arXiv:hep-ph/9502238.

[87] LHCb, D. Hill, M. John, and P. Gandini, *A study of partially reconstructed $B^\pm \to D^{*0}h^\pm$ decays using the $D^0 \to K\pi, KK, \pi\pi$ final states*, LHCb-ANA-2017-018.

[88] LHCb collaboration, R. Aaij *et al.*, *Measurement of CP observables in $B^\pm \to D^{(*)}K^\pm$ and $B^\pm \to D^{(*)}\pi^\pm$ decays*, Phys. Lett. **B777** (2017) 16, arXiv:1708.06370.

[89] G. H. Golub and C. F. Van Loan, *Matrix Computations (3rd Ed.)*, Johns Hopkins University Press, Baltimore, MD, USA, 1996.

[90] S. Viret, C. Parkes, and M. Gersabeck, *Alignment procedure of the LHCb Vertex Detector*, Nucl. Instrum. Meth. **A596** (2008) 157, arXiv:0807.5067.

[91] S. Borghi *et al.*, *First spatial alignment of the LHCb VELO and analysis of beam absorber collision data*, Nucl. Instrum. Meth. **A618** (2010) 108.

[92] LHCb collaboration, R. Aaij *et al.*, *Measurement of the CKM angle γ from a combination of LHCb results*, JHEP **12** (2016) 087, arXiv:1611.03076.

[93] LHCb collaboration, R. Aaij *et al.*, *A measurement of the CKM angle γ from a combination of $B^{\pm} \to Dh^{\pm}$ analyses*, Phys. Lett. **B726** (2013) 151, arXiv:1305.2050.

[94] LHCb collaboration, R. Aaij *et al.*, *Measurement of CP violation and the B_s^0 meson decay width difference with $B_s^0 \to J\Psi K^+K^-$ and $B_s^0 \to J\Psi\pi^+\pi^-$ decays*, Phys. Rev. **D87** (2013) 112010, arXiv:1304.2600.

[95] R. Tibshirani, *Regression shrinkage and selection via the Lasso*, Journal of the Royal Statistical Society, Series B **58** (1994) 267.

[96] B. Guegan, J. Hardin, J. Stevens, and M. Williams, *Model selection for amplitude analysis*, JINST **10** (2015), no. 09 P09002, arXiv:1505.05133.

Acknowledgments

I would like to use this opportunity and thank some people (and probably forget a dozen others) who helped me in various ways to complete this thesis.

First, I like to thank my supervisor Ulrich Uwer who guided me through all the different degrees this University has to offer: He has been the main supervisor for my Bachelor, Master and now, my Ph.D thesis. Thank you for giving me the opportunity for all this, while allowing a lot of freedom in choosing my topics of interest. Also, I would like to thank Hans-Christian Schultz-Coulon who agreed to be the second referee for all my theses including this one and Stephanie Hansmann-Menzemer for the useful advice during the years I have been a member of the LHCb group, especially during our weekly seminars.

My gratitude goes to to the whole LHCb group at the PI Heidelberg for providing the most pleasant, relaxed and friendly working atmosphere throughout the years. I hope the next generation of young scientists will keep up this great environment and that they can experience it the way I did for the last seven years. In particular, I am thankful to my close collaborators Eva Gersabeck and Philippe d'Argent. Without them, this analysis would not have been possible. Eva additionally provided comments and reviewed this thesis several times, while Philippe's deep understanding of the physics, as well as the technical details of the analysis were very helpful. Thanks are due to Manuel Schiller, who was the first person that talked to me about the idea of measuring γ in the presented decay channel and completes our analysis group. I am also thankful to my longtime friend and theoretical physics expert Sebastian Ohmer, who carefully reviewed the theory chapter despite being on a skiing trip.
Some of my collaborators at the PI are friends I have known since the first Bachelor

semester back in the day. David, Dominik, Philippe, it has been a great time with you guys for almost ten years! Also thanks to my office mate Snow, who manages to make me laugh with her at least five times a day.
A big 'thank you' is due to our secretaries Diana Horneck and Claudia Wallenwein, who manage every organizational problem we encounter with great effort and are additionally a pleasure to chat to just about anything.

I would like to thank my friends in- and outside of physics. There are countless people who contributed in various ways to an excellent work-life balance over the last years. Special thanks to my girlfriend who is always putting up with me, no matter the circumstances.

Finally and above all, I would like to express my gratitude to my parents who supported me in everything I did my whole life. I wrote this exact sentence already in the acknowledgments for my master thesis and it is more true than ever. They always have my back and I never had to worry, because of the support I got from them throughout the long years of studying. Vielen Dank !